INVESTIGATING THE COUPLING BETWEEN TECTONICS, CLIMATE AND SEDIMENTARY BASIN DEVELOPMENT

by

Todd M. Engelder

A Dissertation submitted to the faculty of the

DEPARTMENT OF GEOSCIENCES

In partial fulfillment of the requirements
For the Degree of

DOCTOR OF PHILOSOPHY

In the Graduate College

THE UNIVERSITY OF ARIZONA

2012

THE UNIVERSITY OF ARIZONA
GRADUATE COLLEGE

As members of the Dissertation Committee, we certify that we have read the dissertation

prepared by Todd M. Engelder

entitled "Investigating the effects of climate, tectonics and sedimentary basin development"

and recommend that it be accepted as fulfilling the dissertation requirement for the

Degree of Doctor of Philosophy

_____ Date: February 17, 2012
Jon Pelletier

_____ Date: February 17, 2012
Peter DeCelles

_____ Date: February 17, 2012
Paul Kapp

_____ Date: February 17, 2012
Clement Chase

_____ Date: February 17, 2012
Peter Reiners

Final approval and acceptance of this dissertation is contingent upon the candidate's submission of the final copies of the dissertation to the Graduate College.

I hereby certify that I have read this dissertation prepared under my direction and recommend that it be accepted as fulfilling the dissertation requirement.

_____ Date: February 17, 2012
Dissertation Director: Jon Pelletier

STATEMENT BY AUTHOR

This dissertation has been submitted in partial fulfillment of requirements for an advanced degree at the University of Arizona and is deposited in the University Library to be made available to borrowers under rules of the Library.

Brief quotations from this dissertation are allowable without special permission, provided that accurate acknowledgment of source is made. Requests for permission for extended quotation from or reproduction of this manuscript in whole or in part may be granted by the author.

SIGNED: Todd M. Engelder

ACKNOWLEDGEMENTS

I would like to start out by thanking my committee and especially my advisor Jon Pelletier for helpful suggestions and guidance during my research. Finishing my PhD would not have been possible without financial support from Exxon Mobil through the COSA project. I thank my colleagues Dave Pearson, Jon Volkmer and Ross Waldrip for fielding countless questions about structural geology when I couldn't locate DeCelles or Kapp. Thank you Caitlin Orem, Onne Crouvi and previous officemates for the many long discussions we had about Geomorphology and life in general. Finally, thank you Josh Spinler, Alexander Rohrmann, James Girardi, Andrew Kowler, Mark Warren, Meg Blome, Mark Trees, Mauricio Ibanez-Mejia, Maria Banks and friends outside of Tucson for helping me to "constructively" spend the few hours that I was not focusing on geology.

DEDICATION

I dedicate this dissertation to my parents, Terry and Jan, and my sisters, Zoe and Stacey. Thank you for all your visits, support and words of encouragement throughout graduate school.

TABLE OF CONTENTS

APPENDIX C: QUANTIFYING THE EFFECT OF HYDROLOGIC VARIABILITY ON BEDLOAD SEDIMENT TRANSPORT IN ALLUVIAL CHANNELS

LIST OF ILLUSTRATIONS

ABSTRACT

Sedimentary deposits have been broadly used to constrain past climate change and tectonic histories within mountain belts. This dissertation summarizes three studies that evaluate the effects of climate change and tectonics on sedimentary basin development. (1) The paleoslope estimation method, a method for calculating the threshold slope of a fluvial deposit, does not account for the stochastic variations in water depth in alluvial channels caused by climatic and autogenic processes. Therefore, we test the robustness of applying the paleoslope estimation method in a tectonic context. Based on our numerical modeling results, we conclude that if given sufficient time gravel can prograde long distances at regional slopes less than the minimum transport slope calculated with the paleoslope estimation method if water depth varies stochastically in time, and thus, caution should be exercised when evaluating regional slopes measured from the rock record in a tectonic context. (2) The role of crustal thickening, lithospheric delamination, and climate change in driving surface uplift in the central Andes in southern Bolivia and changes in the creation of accommodation space and depositional facies in the adjacent foreland basin has been a topic of debate over the last decade. Our numerical modeling results show that gradual rise of the Eastern Cordillera above 2-3 km prior to 22 Ma leads to sufficient sediment accommodation for the Oligocene-Miocene foreland basin stratigraphy, and thus, the Eastern Cordillera gained the majority of its modern elevation prior to 10 Ma. Also, we conclude that major changes in grain size and depositional rates are primarily controlled by mountain-belt migration (i.e., climate change and lithospheric delamination are secondary mechanisms). (3) Existing equations

for predicting the long-term bedload sediment flux in alluvial channels include mean discharge as a controlling variable but do not explicitly include variations in discharge through time. We develop an analytic equation for the long-term bedload sediment flux that incorporates both the mean and coefficient of variation of discharge. Our results show that although increasing aridity leads to an increase in large discharges with respect to small discharges, long-term bedload sediment transport rates decrease for both gravel and sand-bed rivers with increasing aridity.

INTRODUCTION

The stratigraphy of sedimentary basins is a partial record of climate change and tectonics because the fluvial systems that convey sediment from the bedrock drainages into the depositional basins are sensitive to changes in discharge, sediment texture, sediment supply from adjacent bedrock drainages and sediment accommodation rates. Thus, sedimentary deposits have been broadly used to constrain past climate change and tectonic histories within mountain belts (e.g. Heller et al., 1988; DeCelles et al., 1998; Gaupp et al., 1999; Marzo and Steel, 2000, Uba et al., 2007). However, linking stratigraphic patterns within sedimentary basin stratigraphy to either climate change or tectonics alone is challenging because the stratigraphy is a partial signal of both of these processes as well as autogenic processes (e.g. entrenchment and filling cycles and channel avulsion). For example, the onset of the South American monsoon, mountain-belt migration and rapid surface uplift within the mountain belt are three mechanisms that have been proposed for causing the grain size and depositional rate increases within the Neogene stratigraphy of the Chaco Foreland basin of the central Andes in southern Bolivia (DeCelles and Horton, 2003; Uba et al., 2006; Uba et al., 2007). This dissertation contains three studies that aim to further improve upon our understanding of how climate change, tectonics and autogenic processes affect the stratigraphy of and the sediment transport rates within sedimentary basins.

Several studies have used the paleoslope estimation method developed by Paola and Mohrig (1996) combined with grain size and channel depth data from gravel units that were deposited in alluvial channels to infer the presence or absence of tectonically-

driven tilting since the deposition of the gravel units (e.g. Kirby et al., 2000; McMillan et al., 2002; Cassel and Graham, 2011). It has been long recognized that sediment grains require a critical shear stress to initiate entrainment (Shields, 1936; Meyer-Peter and Mueller, 1948). Using the concept of a critical shear stress, Paola and Mohrig (1996) showed that the minimum transport slope for gravel-bed channels with cohesionless channel banks is proportional to bankfull flow depth and the median grain size of the channel bed sediment. Therefore, the stratigraphy of depositional units can be analyzed in outcrops to obtain these parameters and calculate the minimum paleoslope at which the coarse sediments within the depositional units were transported. However, the paleoslope estimation method does not account for climatically and autogenically driven changes in water depth that occur within alluvial channels, and thus, the paper in Appendix A evaluates the robustness of using the paleoslope estimation method to infer tectonics within sedimentary basins through a numerical modeling analysis.

Specifically, we focus on the study in which Heller et al. (2003) calculated paleoslopes for three long-runout gravel units in the Western U.S. (i.e., Shinarump Conglomerate of the Upper Triassic Chinle Formation, Lower Cretaceous conglomerate units and the Tertiary Ogallala Group). Long-runout gravels as defined by Heller et al. (2003) are gravels that have been transported hundreds of kilometers from their source regions. Heller et al. (2003) found that the calculated minimum paleoslopes for each of the three gravel units are greater than the slopes measured in outcrop. The three long-runout gravels were deposited on top of sedimentary units that contain depositional faces indicative of low-energy environments, and therefore, Heller et al. (2003) inferred that

topography was originally flat at the beginning of gravel transport and deposition. In the absence of tectonics, the clastic wedge created by gravel deposition would have to maintain the minimum transport slope to convey gravels far out into the basin (Figure 1A). However, the slope that Heller et al. (2003) measured from the internal relief of the gravel deposits was less than the calculated minimum transport slope. Based on this result, Heller et al. (2003) concluded that tectonic tilting must have occurred to allow gravels to be transported hundreds of kilometers from their source region (Figure 1B).

A key assumption of the paleoslope estimation method is that the fining upward sequence measured in outcrops represents the flow depth during gravel transport. However, flow depth varies in space and time in ways that may affect the accuracy of the paleoslope estimation method. For example, flow depth varies in response to one to several year changes in flood discharge and at longer time scales in response to climatic and autogenic processes (Schumm and Hadley, 1957; Leopold, 1964; Patton and Schumm, 1975). The non-steady-state nature of channel geometries is also significant because the stratigraphic record contains only depositional channels within the infill (i.e., only the final stage of active-incision is preserved as a scour surface). As such, the paleoslope estimation method uses an inherently biased proxy for flow depth during transport of the coarsest load if channel dimensions are measured from an individual stacked channel within an infilling succession. Given these considerations, it is reasonable to expect that threshold slopes for entrainment in natural rivers, which are function of flow depth, vary stochastically in time. If the threshold slope of entrainment varies stochastically through time, then the transport of coarse sediments such as gravel is

no longer controlled by just an average threshold condition (i.e., the threshold inferred from measuring the flow depth from outcrop). Instead, gravel may be able to prograde at channel slopes lower than the minimum value predicted by paleoslope estimation theory, albeit for geologically brief periods of time when threshold slope is lower than average.

The paper contained in Appendix B uses a coupled mountain-belt and foreland basin numerical model to constrain the surface uplift history of the eastern margin of the central Andes in southern Bolivia as well as constrain the effects of climate change and continental lithospheric delamination on the foreland basin stratigraphy. Numerical models are useful tools for simulating the response of alluvial channel profiles, and thus sedimentary basins, over geologic time scales to climatic and tectonic forcings. The first attempts to quantitatively predict sedimentary basin subsidence came from McKenzie (1978) and Beaumont (1978). The Beaumont (1978) study showed that stratigraphic patterns within foreland basins might contain a signature of lithospheric rheology (Paola, 2000). Later, Flemings and Jordan (1989) was the first study to couple subsidence and surface processes in a 2-dimensional foreland basin model. In their model, Flemings and Jordan (1989) simulated erosion and sediment transport using a diffusion model, which assumes that sediment flux is linearly proportional to the surface slope. Although the rate of sediment transported by an individual flood can be highly non-linear with respect to the channel slope, the long-term sediment transport rates averaged over many flood events has been both experimentally and theoretically shown to approximate diffusion (Begin et al., 1981; Paola et al., 1992). The results of Flemings and Jordan (1989) showed that the growth of a mountain belt eventually causes foreland basins to switch from

underfilled to overfilled as drainage development and increasing mountain front slopes lead to sediment input rates surpassing sediment accommodation rates. A second result of the study was that depositional energy, and thus, grain size is primarily influenced by a depositional zone's distance from the approaching mountain front. Following these early studies, coupled numerical models have improved by adding complexity to surface processes, dynamically predicting lithospheric deformation or simulating evolution of foreland basins in three dimensions (e.g. Coulthard et al., 2002; Clevis et al., 2003; Simpson, 2004).

An unresolved issue for the central Andes in southern Bolivia that is addressed in a numerical modeling study described in Appendix B is: when did the topography of central Andes rise to its modern elevation? The classic model for the central Andes poses that the majority of surface uplift occurred in response to Neogene thermal weakening of the lithosphere and deformation within the Subandean zone (a regional map that shows the location of tectonomporphic zones can be found in Figure 1 of Appendix B), which is the modern fold-and-thrust belt, and that earlier Tertiary deformation contributed to a small fraction of the modern topography (Isacks, 1988). Results from paleoelevation and geomorphic studies indeed support Late Neogene rapid surface uplift of the region (Gubbels et al., 1993; Barke and Lamb, 2006; Ghosh et al., 2006; Hoke et al., 2007; Garzione et al., 2008). A second conceptual surface uplift model poses that the central Andes have been gradually rising since deformation propagated east into the Eastern Cordillera and that the Eastern Cordillera had risen to near modern elevation prior to the Late Neogene. Evidence for pre-Neogene deformation and surface uplift come from

stratigraphic and thermochronologic studies (Horton et al., 2002; McQuarrie et al., 2005; Ege et. al., 2007; Barnes et al., 2008).

A second goal of the paper contained in Appendix B is to determine if the stratigraphic pattern of the Neogene stratigraphy of the Subandean zone is primarily controlled by the eastward propagation of the mountain belt or if there is a signal of climate change and/or continental lithospheric delamination. The Petaca Formation located at the base of the Neogene section contains fluvial deposits that are characterized by well developed paleosols and westward paleocurrent directions (Uba et al., 2006). Above the Petaca Formation, the mean grain size decreases and transport directions are predominantly north-south in the Yecua Formation. The transition upward into the Tariquia Formation occurs as a factor of five increase in depositional rates, grain size increase and a shift in paleocurrent directions toward the east. DeCelles and Horton (2003) and Uba et al. (2006) interpreted the Tertiary stratigraphy as evidence for a migrating mountain belt. However, Uba et al. (2007) interpreted the change in depositional rates and depositional facies between the Yecua and Tariquia Formation as a signal of climate change. Kleinert and Strecker (2001) documented a change from previously dry to wetter conditions in the Santa Maria basin of Northern Argentina between 9-7 Ma. Uba et al. (2007) posed that the onset of the South American monsoon would lead to higher sediment input from the mountain belt, and thus, higher depositional rates within the foreland basin.

Continental lithospheric delamination is another mechanism that may have influenced the stratigraphy of the Chaco foreland basin at this time. Continental

lithospheric delamination involves the removal of negatively buoyant lower crust (i.e., eclogite root) and mantle lithosphere. DeCelles et al. (2009) pose that in cordilleran orogenic systems like the Andes large volumes of lower crust are thrust beneath the developing orogen. Through melting of the lower crust beneath the magmatic arc, the lower crust is partitioned into a felsic melt and a mafic residual. The mafic residual can form a dense eclogitic root that is negatively buoyant with respect to the surrounding mantle if it is formed at pressures that exceed ~15 kbar (Wolf and Wyllie, 1993; Rapp and Watson, 1995; Rushmer, 1995). The eclogite root continues to grow as lower crust is thrust beneath the magmatic arc until it reaches a critical mass and founders into the mantle. The growth and foundering of an eclogite root is part of a conceptual model called the Cordilleran Cycle that relates feebacks between convergence rates, magmatic processes and delamination (DeCelles et al., 2009). Growth and delamination of an eclogite root has consequences for the foreland basin stratigraphy because the eclogite root is a subsurface load that modifies the elevation of the overlying mountain belt, and thus, the deflection of the lithosphere underlying the foreland basin. The presence/absence of an eclogite root also affects shortening rates within the upper plate, and thus, affects the rate of mountain belt propagation into the foreland basin. Thus, unconformities, changes in grain size and/or changes in depositional rates within the Neogene stratigraphy of the Subandean Zone of the central Andes may be a partial signal of eclogite root growth and delamination.

Thus far we have discussed sedimentary basins that are partially influenced by tectonics or feedbacks with the basin-bounding topography. However, the paper included

in Appendix C focuses only on climate change as the mechanism for varying long-term sediment transport rates in sedimentary basins. Long-term in the context of this research refers to time scales of decades to centuries, i.e. sufficiently long that the estimated sediment flux for a given location includes the cumulative effects of many flood events but not so long that the estimate averages over the effects of different climatic conditions. Constraining the effect of climate change on alluvial channel bedload transport efficiency is necessary for understanding the evolution of sedimentary basins, because upstream sediment flux acts as a principal boundary condition for terrestrial and marine depozones (Paola et al., 1992; Tucker and Slingerland, 1999; Molnar, 2004; Barnes and Haines, 2009). Changes in transport efficiency within a sedimentary basin can also modify erosional rates in the upstream drainage basins because the slope of the sedimentary basin sets the local base level of the drainage basin.

An unresolved question in fluvial geomorphology posed by Molnar (2001) is: does increasing aridity lead to an increase in the long-term sediment transport of a channel? Long-term sediment transport is the total sediment transported by distribution of floods or discharges that occur in a channel. Two important parameters of the discharge distribution are the mean and variation. Analysis of channel hydrographs reveals that discharge variability, expressed as a coefficient of variation (i.e., the standard deviation normalized by the mean), increases with increasing aridity. Turcotte and Greene (1993), for example, analyzed peak annual discharge for 10 channels in various climates across the United States. Their results showed that the ratio of the frequency of the largest discharges to that of the mean discharge increased significantly with increasing aridity. In

the most comprehensive analysis to date, McMahon et al. (2007) analyzed the sample statistics of 1221 channels globally. Their results confirm a negative correlation between the coefficient of variation of annual discharge and mean annual runoff. Therefore, as climates shift to greater aridity (i.e., decrease in the mean discharge), the variability in discharge increases. Discharge variability is important for long-term transport rates because sediment transport is a nonlinear function of discharge. As such, Molnar (2001) concluded that channels in arid climates would transport more sediment than the same channel in a humid climate. In effect, Molnar (2001) argued that the increase in the flashiness of discharge more than compensated for the decrease in mean discharge with increasing aridity. The reason for this is related to the fact that large floods are so much more effective, per unit discharge, than small floods.

Another unresolved question in fluvial geomorphology that is addressed in Appendix C is: what is the effect of increasing aridity on the return period of the effective discharge. The effective discharge is defined as the discharge magnitude that transports the most sediment over an interval of time (Wolman and Miller, 1960). The return period of the effective discharge has implications for the stability of a channel. Channels that have effective discharges with long return periods are thought to spend the majority of their time in a state of recovery. Another implication for return period of the effective discharge is to assess the time scales over which modern bedload fluxes are representative of the bedload component of long-term basin-averaged erosion rates. In a study of mixed bedrock and alluvial drainages in Idaho, Kirchner et al. (2005) found that basin-average erosion rates representing time scales of 10^3 to 10^7 years were an order of

magnitude greater than that those that represent 1 to 10 years. The decrease in basin-averaged erosion rates was interpreted as an effect of the sampling period, and thus, the modern erosion rates had not yet sampled a thousand year event that does more than 90 percent of the long-term geomorphic work.

PRESENT STUDY

The methods, results, and conclusions of this study are presented in the papers appended to this dissertation. The following is a summary of the most important findings in this document.

Previous studies have used the paleoslope estimation method of Paola and Mohrig (1996) to calculate the minimum paleoslopes of fluvial systems that deposited long-runout gravels in the western U.S. (McMillan et al., 2002; Heller et al. 2003). Heller et al. (2003) found that the upper slopes of the gravel wedges for each long-runnout gravel due to deposition above previously flat lying sediments were less than the calculated minimum slope required to entrain the gravel. Heller et al. (2003) interpreted the low gradients of the gravel deposits as evidence of tectonically driven regional tilting. For example, Heller et al. (2003) proposed that the long-wavelength tilting that led to the transport of the Miocene Ogallala Group into the Great Plains of the Western U.S. was caused by a combination of dynamic rebound due to the passage of the Farallon slab and regional lithospheric warming associated with extension within the Rio Grande Rift.

Using a 2-D coupled mountain belt and foreland basin numerical model, we explore the following question: given a sufficient period of time, can gravels prograde several hundred kilometers from their source regions at slopes significantly lower than the threshold slope predicted by the paleoslope estimation method given realistic variations in the threshold slope of entrainment in space and/or time (Appendix A)? A key assumption of the paleoslope estimation method is that the fining upward sequence

measured in outcrop is a proxy for the flow depth during gravel transport. However, flow depth varies in space and time due to climatic and autogenic processes such that gravel transport is a function of the variation in flow depth in addition to the mean flow depth and median grain size. In order to test the hypothesis that gravels can be transported long distances at regional slopes below the threshold slope predicted by the paleoslope estimation method, we allow threshold slopes that are a function of flow depth and median grain size to vary stochastically through time in our numerical model. Stochastic variation in threshold slope is simulated with a lognormal distribution. The coefficient of variation of the lognormal distribution was calculated using data from North American gravel-bed rivers (Church and Rood, 1983).

Simulations were run for two types of sedimentary basins: (1) isolated sedimentary basin and (2) a postorogenic foreland basin. The isolated sedimentary basin model allows us to isolate the effects of stochastic variation in threshold slopes on gravel transport independent of tectonics. The results of the isolated basin model show that gravel can prograde at regional slopes below the minimum transport slope predicted by the paleoslope estimation method if the coefficient of variation of threshold slope is greater than zero and the sediment supply does not greatly exceed the transport capacity of the main gravel-bed rivers within the depositional basin. A comparison of this result with the dynamically-coupled postorogenic foreland basin model results allows us to determine whether or not feedbacks between sediment supply to the basin and the base level of erosion for the mountain belt (controlled by transport efficiency of sediments across the basin) act in concert to control the rates and slopes at which a gravel wedge

can prograde within a sedimentary basin. The time required for the regional slope of the gravel-bed rivers to decrease below the minimum transport slope predicted by the paleoslope estimation method is depend on the transport efficiency of the rivers, the sediment supply rates from the upstream drainage basins and the variability of the threshold slope. The results of the postorogenic foreland basin model show that soon after the cessation of active uplift in the mountain belt (< 2 Myr), the regional slopes of gravel-bed rivers are generally high because sediment fluxes from the mountain belt are high. Beyond 2 Myr, the regional slopes of the gravel-bed rivers begin to decrease as sediment flux from the mountain belt decreases and the distal toe of gravel depositional passes into the postorogenic backbulge basin.

In our second study (Appendix B), a single 2-D coupled mountain belt and foreland basin numerical model was used to explore three issues for the central Andes: (1) constrain the surface uplift history of the eastern margin of the central Andes through comparing the results of end-member surface uplift experiments against the observed foreland basin stratigraphy, (2) constrain the effect of the continental lithospheric delamination on the foreland basin stratigraphy and (3) constrain the effect of climate change on the foreland basin stratigraphy. For the end-member uplift model experiments, climate and the rigidity of the South American plate are held constant. The timing of initiation and duration of crustal deformation within each of the tectonomorphic zones (e.g. Eastern cordillera, Interandean zone, Subandean zone) was prescribed based on published exhumation ages and stratigraphic relationships (Muller et al., 2005; Ege et al., 2007; Barnes et al., 2008). Rock uplift rates and bedrock erodibilities were calibrated in

the end-member surface uplift model experiment by fitting the observed modern topography and exhumation magnitudes. The results of this experiment show that the gradual uplift model fits the Eocene-early Miocene foreland basin stratigraphy best, and therefore, the Eastern Cordillera should have gained significant elevation (i.e., >2 km) by 22 Ma. Although the Eastern Cordillera was near modern elevation by 10 Ma, rapid uplift within the Interandean and western Subandean zones is still necessary to create sufficient sediment accommodation space for the Late Miocene foreland basin stratigraphy.

The continental lithospheric delamination experiments involved the growth and delamination of an eclogite root. The eclogite root was prescribed to be 100 km wide and located within the eastern Altiplano and Eastern Cordillera backthrust region based on geophysical data from the central Andes of Southern Bolivia (Beck and Zandt, 2002). We assume that the eclogite delamination is caused by a Raleigh-Taylor instability (defined as the diapiric drip of a dense layer overlying a less dense layer). We also assume that the majority of the delamination event is spent growing the instability (i.e., drip) by a factor of e, and thus, the maximum thickness of the eclogite root prior to delamination can be calibrated such that the majority of the delamination period was spend growing the instability. As such, we prescribe the thickness of the eclogite layer prior to delamination to be approximately 12.5 km. In this experiment the climate, elastic rigidity, timing and duration of deformation are the same as in the end-member surface uplift experiment. Between the initial

The results of the continental lithospheric delamination experiment show that the delamination of an eclogite root of the prescribed dimensions (i.e., 100 by 12.5 km)

causes approximately 1 km of isostatic rebound at the boundary between the Altiplano and Eastern Cordillera directly above the center of the root when the rigidity of the South American plate is approximately $6.8x10^{23}$ Nm. The isostatic rebound is not uniform, however, and rapidly decreases away from the center of the eclogite root. During the development of the foreland basin between 30 and 7 Ma the foredeep is always more than 300 km away from the center of the eclogite root. The deflection of the foredeep due to the growth and delamination of the eclogite root is less than or equal to 100 meters, and thus, the depositional rates of the foredeep stratigraphy is expected to be more sensitive to surface uplift rates in the front of the mountain belt than growth and removal of an ecologite root located on the eastern edge of the Altiplano. However, the growth and removal of an eclogite root may have a more significant effect on the foreland basin stratigraphy if the presence or absence of an eclogite root significantly modifies the convergence rates between the mountain belt and the South American plate (DeCelles et al., 2009).

The final experiment involved constraining the effect of the onset of the South American monsoon on the Late Miocene foreland basin stratigraphy. In this experiment the both erosion rates and sediment transport rates are reduced by a factor of two with respect to the values used within the end-member surface uplift models between 43 and 9 Ma. At 9 Ma, the erosion and sediment transport rates are increased by a factor of two to simulate the onset of the South American monsoon.

The results of the climate change experiment show that sediment fluxes from the central Andes into the foredeep basin are sufficient to overfill the basin from the Miocene

to present, and thus, sediment accommodation is the dominant mechanism for controlling depositional rates within the foreland basin.The results for the climate change experiment also show that increasing erosion and precipitation rates by a factor of two has a less dominant effect on the distribution of grain size within the foreland basin than migration of the mountain belt toward the foreland basin, and thus, is in agreement with the results of Flemings and Jordan (1989).

In the third study (Appendix C), we derive an expression for the long-term bedload sediment transport rates of alluvial channels and use the expression to explore three applications: (1) constrain the effect of climate change on long-term bedload sediment transport rates, (2) derive a diffusivity that includes the effects of discharge variability and (3) constrain the effect of climate change on the effective discharge. Wolman and Miller (1960) first proposed that the geomorphic work (i.e. long-term sediment transport) performed by a channel could be quantified by integrating the product of a sediment transport function and a frequency-size distribution of discharge over the range of all possible discharges (Figure 2). Thus, we integrated the bedload sediment transport formula of Wiberg and Smith (1989) and Engelund and Hansen (1967) with a lognormal distribution to solve for the long-term bedload sediment transport rates for both gravel and sand-bed channels. In the first application we compare gravel and sand-bed channels with the same grain size distributions and along profile slopes with different mean annual runoffs to constrain the effect of climate on long-term bedload sediment flux. Previous studies have demonstrated that discharge variation (i.e., the coefficient of variation of annual discharge) negatively correlates with mean annual

runoff and mean annual precipitation (Turcotte and Greene, 1993; Molnar et al., 2006; McMahon et al., 2007). We analyze 530 hydrographs from North American channels to develop an equation that relates the coefficient of variation of daily discharge to mean annual runoff. The results of the first application show that long-term bedload sediment transport rates decrease with increasing aridity for both gravel and sand-bed channels. Although the frequency of large discharges increases with aridity, the threshold for transporting both gravel and sand-sized grains is sufficiently low that shifting the mode of the discharge distribution toward smaller discharges decreases the long-term bedload sediment transport rate.

Another goal of the study described in Appendix C is to constrain the effect of climate change on the effective discharge for bedload transport in both gravel and sand-bed channels. The effective discharge is defined as the discharge magnitude that transports the most sediment per time (Wolman and Miller, 1960). Wolman and Miller (1960) showed that the effectiveness function for a given discharge distribution is the product of the sediment transport function and the discharge distribution (Figure 2). The discharge located beneath the peak of the effectiveness curve is the effective discharge. The effective discharge can be calculated by setting the derivative of the effectiveness curve equal to zero and then solve for discharge. Again we apply a lognormal distribution and the bedload sediment transport formula of Wiberg and Smith (1989) and Engelund and Hansen (1967) in this analysis. The results of this analysis show that the effective discharge for bedload sediment transport within a sand-bed channel has a return period that is less than a year when the mean annual runoff ranges between 0.01 and 1.0 m.

However, the return period for the effective discharge in gravel-bed channels can be significantly longer (up to hundreds of years) when the mean annual runoff is less than 0.02 m. When the mean annual runoff is greater than 0.1 m, the return period of the effective discharge for gravel-bed channels is less than or equal to one year. This result has implications for how well the bedload component of modern basin-averaged erosion rates represents the bedload component of erosion rates over thousands of years. Kirchner et al. (2001) found that modern basin-averaged erosion rates for gravel-bed channels in Idaho with mean annual runoffs of approximately 0.5m were an order of magnitude less than erosion rates that represent time scales of 10^3-10^7 of years. Conversely, our results show that the effective discharge for gravel-bed channels with mean annual runoffs greater than 0.2m occur on average once a year, and thus, the modern long-term bedload sediment transport rates measured in gravel-bed channels should reflect bedload transport rates representative of greater time scales.

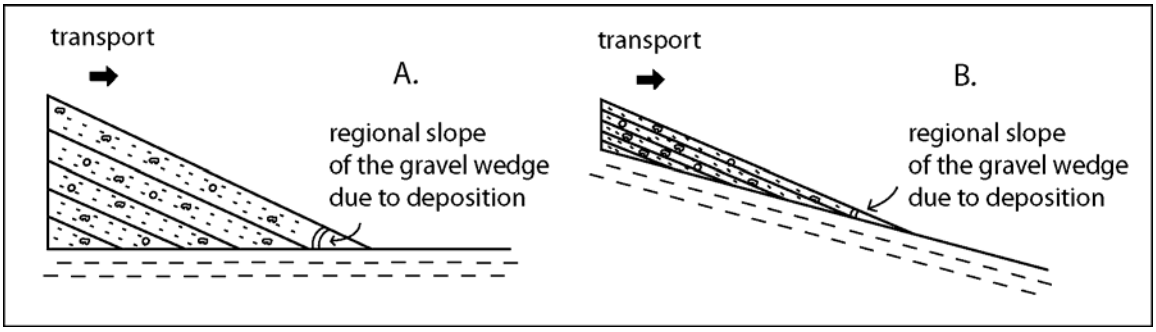

Figure 1: Conceptual diagrams of a gravel wedge prograding above (A) older flat-lying sedimentary deposits and (B) tectonically-tilted older deposits in response to an upstream sediment source. The regional slope of the gravel wedge due to deposition as measured by Heller et al. (2003) is represented by the angle between the upper surface of the gravel wedge and the underlying depositional unit.

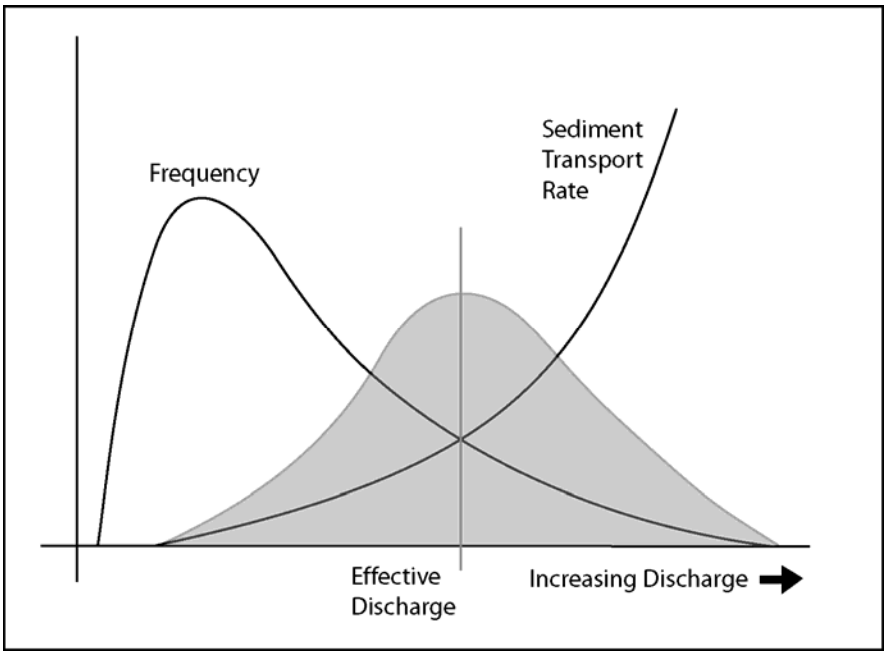

Figure 2: A plot of the relationship between long-term sediment transport, discharge frequency and sediment transport rates after Wolman and Miller (1960). The gray area, which represents the long-term sediment transport rate, is bound on top by the effectiveness curve of Wolman and Miller (1960).

REFERENCES

Beaumont, C., 1978. The evolution of sedimentary basins on a viscoelastic lithosphere: theory and examples. Geophysical Journal of the Royal Astronomical Society, 55, 471-497.

Beck, S.L. and Zandt, G., 2002. The nature of orogenic crust in the central Andes. Journal of Geophysical Research, 107, doi:10.1029/2000JB000124.

Begin, S.B., Meyer, D.F., Schumm, S.A., 1981. Development of longitudinal profile of alluvial channels in response to base-level lowering. Earth Surface Processes and Landforms, 6, 49-68.

Barke, R. and Lamb, S., 2006. Late Cenozoic uplift of the Eastern Cordillera, Bolivian Andes, Earth and Planetary Science Letters, 249, 350-367.

Barnes, J.B., Ehlers, T.A., McQuarrie, N., O'Sullivan, P.B., Tawackoli, S., 2008. Thermochronometer record of the central Andean Plateau growth, Bolivia (19.5^{o}S). Tectonics, 27, TC3003, doi:10.1029/2007TC002174.

Barnes, J.B. and Haines, W.A., 2009. Plio-Quaternary sediment budget between thrust belt erosion and foreland deposition in the central Andes, southern Bolivia. Basin Research, 21, 91-109.

Cassel, E.J., Graham, S.A., 2011. Paleovalley morphology and fluvial system evolution of Eocene-Oligocene sediments ("auriferous gravels"), northern Sierra Nevada, California: Implications for climate, tectonics, and topography. Geological Society of America Bulletin, 123, 1699-1719.

Church, M., and Rood, K., 1983. Catalogue of Alluvial River Channel Regime Data: Vancouver, British Columbia, Canada, University of British Columbia, Department of Geography.

Clevis, Q., de Boer, P., Wachter, M., 2003. Numerical modeling of drainage basin evolution and three-dimensional alluvial fan stratigraphy. Sedimentary Geology, 163, 85-110.

Coulthard, T.J., Macklin, M.G., Kirkby, M.J., 2002. A cellular model of a Holocene upland river basin and alluvial fan evolution. Earth Surface Processes and Landforms, 27, 269-288.

DeCelles, P.G., Ducea, M.N., Kapp, P., Zandt, 2009. Cyclicity in Cordillera orogenic systems. Nature Geosciences, 2, 251-257.

DeCelles, P.G., Gehrels, G.E., Quade, J., Ojha, T.P., Kapp, P.A., Upreti, B.N., 1998. Neogene foreland basin deposits, erosional unroofing and the kinematic history of the Himalayan fold-thrust belt, western Nepal. Geological Society of America Bulletin, 110, 2-12.

DeCelles, P.G. and Horton, B.K., 2003. Early to middle Tertiary foreland basin development and the history of Andean crustal shortening in Bolivia. Geological Society of America Bulletin, 115, 58-77.

Ege, H., Sobel, E.R., Scheuber, E., Jacobshagen, V., 2007. Exhumation history of the southern Altiplano plateau (southern Bolivia) constrained by apatite fission track thermochronolgy. Tectonics, 26, TC1004, doi:10.1029/2005TC001869.

Flemings, P.B. and Jordan, T.E., 1989. A synthetic stratigraphic model for foreland basin development. Journal of Geophysical Research, 94, 3851-3866.

Garzione, C.N., Hoke, G.D., Libarkin, J.C., Withers, S., MacFadden, B., Eiler, J., Ghosh, P., Mulch, A., 2008. Rise of the Andes. Science, 320, 1304-1307.

Gaupp, R., Kott, A., Worner, G., 1999. Palaeoclimatic implications of Mio-Pliocene sedimentation in the high-altitude intra-arc Lauca basin of northern Chile. Paeogeography, Palaeoclimatology, Palaeoecology, 151, 79-100.

Ghosh, P., Garzione, C.N., Eiler, J., 2006. Rapid uplift of the Altiplano revealed through ^{13}C-^{18}O bonds in paleosol carbonates. Science, 311, 511-512.

Gubbels, T.L., Isacks, B.L., Farrar, E., 1993. High-level surfaces, plateau uplift, and foreland development, Bolivian central Andes. Geology, 21, 695-698.

Heller, P., Angevine, C.L., Winslow, N.S., Paola, C., 1988. Two phase stratigraphic model of foreland-basin sequences. Geology, 16, 501-504.

Heller, P.L., Dueker, K., and McMillan, M.E., 2003. Post-Paleozoic alluvial gravel transport as evidence of continental tilting in the U.S. Cordillera: Geological Society of America Bulletin, 115, 1122-1132.

Hoke, G.D., Isacks, B.L., Jordan, T.E., Blanco, N., Tomlinson, A.J., Ramezani, J., 2007. Geomorphic evidence for post-10 Ma uplift of the western flank of the central Andes 18°30'-22°S. Tectonics, 26, TC5021, doi:10.1029/2006TC002082.

Horton, B.K., Hampton, B.A., LaReau, B.N., Baldellon, E., 2002. Tertiary provenance history of the northern and central Altiplano (Central Andes Bolivia): A detrital record of plateau-margin tectonics. Journal of Sedimentary Research, 72, 711-726.

Isacks, B.L., 1988.Uplift of the Central Andean Plateau and bending of the Bolivian orocline. Journal of Geophysical Research, 93, 3211-3231.

Leier, A.L., P.G. DeCelles, Pelletier, J.D., 2005. Mountains, monsoons, and megafans. Geology, 33, 289-292.

Leopold, L.B., Wolman, M.G., and Miller, J.P., 1964. Fluvial processes in geomorphology: San Francisco, W.H. Freeman and Company.

Kirby, E., Whipple, K.X., Burchfiel, B.C., Tang, W., Berger, G., Sun, Z., Chen, Z., 2000. Neotectonics of the Min Shan, China: Implications for mechanisms driving Quaternary deformation along the eastern margin of the Tibetan Plateau. Geological Society of America Bulletin, 112, 375-395.

Kirchner, J.W., Finkel, R.C., Riebe, C.S., Granger, D.E., Clayton, J.L., King, J.G., Megahan, W.F., 2001. Mountain erosion over 10 yr. 10 k.y., and 10 M.y. time scales. Geology, 29, 591-594.

Kleinert, K. and Strecker, M.R., 2001. Climate change in response to orographic barrier uplift: Paleosol and stable isotope evidence from the Late Neogene Santa Maria basin, northwestern Argentina, Geological Society of America Bulletin, 113, 728-742.

Marzo, M. and Steel, R.J., 2000. Unusual features of sediment supply-dominated, transgressive-regressive sequences: Paleogene clastic wedges, SE Pyrenean foreland basin, Spain. Sedimentary Geology, 138, 3-15.

McKenzie, D.P., 1978. Some remarks on the development of sedimentary basins. Earth and Planetary Science Letters, 40, 25-32.

McMahon, T.A., Vogel, R.M., Peel, M.C., Pegram, G., 2007. Global Stream Flows – Part 1: Characteristics of annual stream flows. Journal of Hydrology, 347, 243-259.

McMillan, M.E., Angevine, C., and Heller, P.L., 2002. Postdepositional tilt of the Miocene-Pliocene Ogallala Group on the western Great Plains: Evidence of late Cenozoic uplift of the Rocky Mountains: Geology, 30, 63-66.

McQuarrie, N., Horton, B.K., Zandt, G., Beck, S., DeCelles, P.G., 2005. Lithospheric evolution of the Andean fold-thrust belt, Bolivia, and the origin of the central Andean pleateau. Tectonophysics, 399, 15-37.

Meyer-Peter, E., and Mueller, R., 1948. Formulas for bed-load transport, *in* Proceedings, International Association for Hydraulic Structures Research Meeting, 2nd, Stockholm, Sweden, 39-64.

Molnar, P., 2001. Climate change, flooding in arid environments, and erosion rates. Geology, 29, 1071-1074.

Molnar, P., 2004. Late Cenozoic increase in accumulation rates of terrestrial sediment: How might climate change have affected erosion rates? Annual Review of Earth and Planetary Sciences, 32, 67-89.

Molnar, P., Anderson, R., Kier, G., Rose, J., 2006. Relationships among probability distributions of stream discharges in floods, climate, bed load transport, and river incision. Journal of Geophysical Research, 111, F02001, doi:10.1029/2005JF000310.

Muller, J.P., Kley, J., Jacobshagen, V., 2002. Structure and Cenozoic kinematics of the Eastern Cordillera, southern Bolivia (21^{o}S). Tectonics, 21, 10.1029/2001TC001340.

Paola, C., 2000. Quantitative models of sedimentary basin filling. Sedimentology, 47, 121-178.

Paola, C., Heller, P.L., and Andgevine, C.L., 1992. The large-scale dynamics of the grain-size variation in the alluvial basins, 1: Theory. Basin Research, 4, 73-90.

Paola, C., and Mohrig, D., 1996. Palaeohydraulics revisited: palaeoslope estimation in coarse-grained braided rivers. Basin Research, 8, 243-254.

Patton, P.C., Schumm, and Stanley, A., 1975. Gully erosion, northwestern Colorado; a threshold phenomenon: Geology, 3, 88-89.

Schumm, S.A., and Hadley, R.F., 1957. Arroyos and semiarid cycle of erosion: American Journal of Science, 255, 161-174.

Simpson, G., 2004. A dynamic model to investigate coupling between erosion, deposition and three-dimensional (thin-plate) deformation. Journal of Geophysical Research, 109, doi:10.1029/2003JF000078.

Tucker, G.E. and Slingerland, R.L., 1996. Predicting sediment flux from fold and thrust belts. Basin Research, 8, 329-349.

Turcotte, D.L., Greene, L., 1993. A scale-invariant approach to flood frequency analysis. Stochastic Hydrology and Hydraulics, 7, 33-40.

Uba, C.E., Heubeck, C., Hulka, C., 2006. Evolution of the late Cenozoic Chaco foreland basin, Southern Bolivia. Basin Research, 18, 145-170.

Uba, C.E., Strecker, M.R., Schmitt, A.K., 2007. Increased sediment accumulation rates and climatic forcing in the central Andes during the Late Miocene. Geological Society of America Bulletin, 35, 979-982.

APPENDIX A: STOCHASTIC VARIATIONS IN WATER FLOW DEPTH AND THEIR ROLE IN LONG-RUNOUT GRAVEL PROGRADATION IN SEDIMENTARY BASINS

Manuscript in review with Lithosphere

Todd M. Engelder* and Jon D. Pelletier
Department of Geosciences, University of Arizona, 1040 E. Fourth St., Tucson AZ, 85721, USA,

**Corresponding Author, email: engelder@email.arizona.edu, fax: (520) 621-2672*

Abstract

Several recent studies have used a threshold shear stress criterion, together with field-based measurements of median grain size and channel depth in alluvial gravel deposits, to calculate the threshold paleoslopes of alluvial sedimentary basins in the western United States. Threshold paleoslopes are the minimum slopes that would have been necessary to transport sediment in those basins. In some applications of this method, inferred threshold paleoslopes are sufficiently steeper than modern slopes that they imply large-magnitude tectonic tilting must have occurred in order to transport sediments to their present locations. In this paper, we evaluate the accuracy and robustness of the paleoslope estimation method and we evaluate the conditions under which long-runout gravels (i.e. gravels several hundred kilometers or more from their source regions) can occur using numerical models for two types of sedimentary basins: (1) an isolated sedimentary basin with a prescribed source of sediment from upstream, and (2) a basin dynamically coupled to a postorogenic mountain belt. Specifically, we address the question: can long-runout gravels prograde at regional slopes significantly lower than those predicted by the paleoslope estimation method? In the models, threshold slopes for entrainment are varied

stochastically in time with an amplitude comparable to those of natural rivers in order to represent fluctuations in flow depth due to hydroclimatic variability and local deviations from an equilibrium channel geometry. The models show that when local threshold slope values vary stochastically, alluvial basin sediments can persistently prograde at slopes far below the threshold slopes predicted by paleoslope estimation theory. As such, the models suggest that long-runout gravels do not require steep regional slopes in order for transport to occur. We conclude that the minimum progradational slopes of fluvial sedimentary basins adjacent to postorogenic mountain ranges are functions of the density and texture of the bed sediment and both the mean and coefficient of variation of flow depths associated with hydroclimatic variability and changes in local channel geometry arising from autogenetic and allogenetic variations.

Keywords- sediment transport, foreland basin, isostatic rebound, stochastic processes

1. Introduction

The concept that gravel transport in rivers requires a threshold bed shear stress has been recognized since the early 1900s (Shields, 1936; Meyer-Peter and Mueller, 1948). If flow conditions produce a shear stress that is greater than the threshold shear stress required for entrainment, sediment transport will take place. Paola and Mohrig (1996) used the threshold shear stress concept to relate the minimum channel slope required for sediment transport to the median grain size and flow depth in gravel-bed channels:

$$S_c = \psi D_{50} H^{-1} \quad (1)$$

where S_c is the threshold channel slope, D_{50} is the median grain size of the mobile bed sediments, H is the flow depth, and ψ (calculated to be 0.094 when the input grain size is the D_{50}) is a global constant for all gravel-bed channels with non-cohesive banks. Equation (1) assumes that flow is quasi-steady, bedforms are not present, and that channel banks are non-cohesive. Gravel-bed channels with non-cohesive banks modify their cross-sectional geometries (e.g. channel width-to-depth ratio) to produce a bank shear stress that is nearly equal to the threshold of entrainment (Parker, 1978; Andrews, 1984), hence channel width can be eliminated from the analysis that leads to equation (1). When this relationship was tested against a dataset of modern gravel-bed rivers compiled by Church and Rood (1983), a significant amount of scatter was observed in the ratio between threshold slopes calculated with equation (1) and observed channel slopes (i.e., S_c/S_{obs}). To within one standard deviation of the geometric mean, predicted threshold

slopes for channels with non-cohesive banks were up to a factor of 1.72 both greater and lesser than the observed slopes (Paola and Mohrig, 1996).

Equation (1) has recently been used to constrain the paleotopography of gravel-dominated alluvial deposits in the North American Cordillera (McMillan et al., 2002; Heller et al., 2003). These deposits are considered to be long-runout gravels because they extend several hundred kilometers from the bedrock drainage basins from which they were sourced. Heller et al. (2003) calculated paleoslopes based on measured median grain sizes and proxies for mean channel depth within outcrops of the Shinarump Conglomerate of the Upper Triassic Chinle Formation, Lower Cretaceous conglomerate units (e.g. Buckhorn Member of the Cedar Mountain Formation in central Utah and the Cloverly Formation in Wyoming) and the Tertiary Ogallala Group. The channel slopes calculated from equation (1) were significantly greater than the slope of the upper surface of the clastic wedge that formed through deposition of gravel above previous topography that Heller et al. (2003) interpreted to be nearly horizontal in slope based on depositional facies indicative of low transport energy. As such, Heller et al. (2003) inferred that pre- or syn-depositional tectonic tilting must have taken place in order to produce the slopes necessary to entrain sediment of the textures observed in these deposits.

A key assumption of the paleoslope estimation method, i.e. using equation (1) to calculate threshold paleoslopes, is that the flow depth inferred from the thickness of the fining-upward sequence in outcrop is equivalent to the minimum effective flow depth during transport. This assumption allows mean data measured from outcrops to be used in place of flow depth H in equation (1). However, flow depth varies in space and time in

ways that may affect the accuracy of the paleoslope estimation method. First, channels are subject to discharges of varying magnitude. Hydrologic time-series data collected within the last hundred years show that river discharges averaged on an annual basis can follow normal, lognormal and power-law distributions with parameters that depend on drainage basin area and climate (e.g. Leopold, 1964; Turcotte and Greene, 1993). As discharge varies, the flow depth must also vary unless the channel width and slope respond instantaneously to changes in shear stress, which they do not. If flow depth varies and grain size does not respond instantly to maintain the threshold condition defined by equation (1), then the threshold slope calculated by equation (1) must vary in time.

At time scales longer than one to several years, threshold slopes also vary because alluvial channels are non-steady-state systems. Instead, they often experience long-lived (i.e., millennial time scales and greater) cut-and-fill cycles triggered both autogenically (Schumm and Hadley, 1957; Patton and Schumm, 1975) and by climatic changes (Bull, 1997). The "cutting" cycle of alluvial channels is often accompanied by local channel narrowing as unit stream power, incision, and channel narrowing operate in a strong positive feedback. Conversely, depositional channels commonly widen as they aggrade. Natural channels can oscillate between these two modes indefinitely, transporting the coarsest load only during episodes of active channel incision when the channel is far from equilibrium (Pelletier and DeLong, 2004). In the southwestern United States, the typical time scale for the cutting and filling of large, valley-floor channels is approximately 1000 years (Waters and Haynes, 2001; Mann and Meltzer, 2007). Although the oscillating

nature of alluvial channels has been most well studied in arid fluvial systems, they are not unique to arid fluvial systems. For example, large meandering channels can exhibit spatial and temporal oscillations in which lateral meandering and deposition occurs preferentially in relatively low-gradient sections of the valley floor, which then builds a steep alluvial toe slope that facilitates entrenchment and narrowing downstream (Jones and Harper, 1998). The non-steady-state nature of channel geometries is also significant because the stratigraphic record contains only depositional channels within the infill (i.e., only the final stage of active-incision is preserved as a scour surface). As such, the paleoslope estimation method uses an inherently biased proxy for flow depth during transport of the coarsest load if channel dimensions are measured from an individual stacked channel within an infilling succession. Given these considerations, it is reasonable to expect that threshold slopes for entrainment in natural rivers vary stochastically in time. Within this conceptual model, time periods of lower-than-average threshold slopes are associated with an incised channel state triggered by climatic changes or autogenetic dynamics.

If the threshold slope of entrainment varies stochastically through time, then the transport of coarse sediments such as gravel is no longer controlled by just an average threshold condition. Instead, gravel may be able to prograde at channel slopes lower than the minimum value predicted by paleoslope estimation theory, albeit for geologically brief periods of time when threshold slope is lower than average. In this paper, we explore the hypothesis that gravel transport is a function of both the mean and coefficient of variation in threshold slope within a numerical modeling framework. Specifically, we

pose the following question: given a sufficient period of time, can gravels prograde several hundred kilometers from their source regions at slopes significantly lower than the threshold slope predicted by equation (1) given realistic variations in the threshold slope of entrainment in space and/or time?

2. Numerical Model Description

We used two types of numerical models in order to test our hypothesis that gravels can be transported over long distances at regional slopes lower than the threshold slope predicted by the paleoslope estimation method. The first model, herein called the isolated sedimentary basin model, represents a gravel wedge prograding along a horizontal plane in response to a sediment source at a fixed position at the upstream end of the basin. Deposition and sediment reworking along a channel profile is simulated using a numerical model that includes mass conservation combined with a slope-dependent transport relationship that contains a grain-size-dependent threshold value. This first model allows us to assess the effects of climate change and autogenetic processes alone on gravel progradation because sediment supply is held constant and tectonic movements are not considered. The second model, herein called the dynamically-coupled postorogenic foreland basin model, represents a gravel wedge prograding within a foreland basin in response to erosional unloading of an adjacent postorogenic mountain belt. This model allows us to observe the effects of feedbacks between erosion in the mountain belt and the evolution of the adjacent sedimentary basin.

The motivation for applying two types of models is that we want to isolate the effects of stochastic variation in threshold slopes on gravel transport in our isolated

sedimentary basin model independent of tectonics and then compare the results to those of a model that includes tectonics by coupling a basin and its adjacent mountain belt. The dynamically-coupled postorogenic foreland basin model allows us to determine whether or not feedbacks between sediment supply to the basin and the base level of erosion for the mountain belt (controlled by transport efficiency of sediments across the basin) act in concert to control the rates and slopes at which a gravel wedge can prograde within a basin. In a numerical modeling study, Paola et al. (1992) showed that varying sediment supply and accommodation rates sinusoidally through time had significant effects on the regional slope of an aggrading alluvial fan. The three long-runout gravels described by Heller et al. (2003) are each associated with a particular period of tectonic activity during which sediment supply and accommodation were not constant. For this reason, we include both a dynamically-coupled model of a mountain belt interacting with an adjacent foreland basin in addition to a model of an isolated basin with a prescribed sediment supply.

In both the isolated sedimentary basin and dynamically-coupled postorogenic foreland basin models, threshold slopes for entrainment are randomly sampled from a lognormal distribution at a regular prescribed interval of time. We use a lognormal distribution because it is the simplest (i.e. two-parameter) distribution available for a positive-definite quantity such as channel slope, and also because it provides a good fit to actual variations observed in modern gravel-bed rivers. Lognormal distributions are defined by a mean and a coefficient of variation given by:

$$C_v = \sigma_{Sc} / \overline{S_c} \quad (2)$$

where C_v is the coefficient of variation, σ_{Sc} is the standard deviation of threshold slope, and $\overline{S_c}$ is the mean of threshold slope. As the C_v of the threshold slope distribution increases, the recurrence interval between periods of threshold slopes significantly lower than average decreases. To estimate an appropriate value for C_v, the mean and standard deviation of the natural logarithm of the observed threshold slopes, i.e. μ and σ, were calculated from the Church and Rood (1983) dataset and related to σ_{Sc} and $\overline{S_c}$ using the following expressions (Turcotte, 1997):

$$\overline{S_c} = e^{\mu + \frac{1}{2}\sigma^2} \quad (3)$$

$$\sigma_{Sc} = \mu\left(e^{\sigma^2 - 1}\right)^{1/2} \quad (4)$$

The mean and coefficient of variation of the Church and Rood (1983) channel slope data were calculated using equations (3) and (4) to be 0.013 and 3.045, respectively. A coefficient of variation greater than 1.0 for a lognormal distribution indicates that the most frequent slope (mode) is significantly less than the average slope (mean). The most frequent slope for gravel-bed rivers in the Church and Rood (1983) dataset is an order of magnitude lower than the average slope and the range of possible slopes spans 3 orders of magnitude between 10^{-4} and 10^{-1}. When the slope data are normalized for average flow depth and median grain size, however, the coefficient of variation in the observed slopes of modern gravel-bed rivers decreases to 1.66 (Figure 1A). This value for C_v is more appropriate as an estimate of the variability of threshold slopes of individual gravel-bed

rivers through time because mean flow depth and median grain size are far more variable between rivers (as in the Church and Rood (1983) dataset) than within an individual river to which the paleoslope estimation method might be applied. A threshold slope of 0.0014 is predicted by equation (1) for a gravel-bed river with an average flow depth of 1.68 m and a median bed-material grain size of 25 mm. We use this threshold slope as our representative value in the simulations described below because it is within the range of threshold slopes calculated for the Ogallala Group, a type-example long-runout gravel deposit. When a C_v value of 1.66 and a mean threshold slope of 0.0014 are used to generate a lognormal distribution, approximately 70 percent of threshold slopes are less than the mean (Figure 1B).

In both types of models we consider here, i.e. in the isolated sedimentary basin model and in the dynamically-coupled postorogenic foreland basin model, gravel transport is modeled via a slope-dependent transport relationship with a grain-size-dependent threshold value. Sediment transport is used, together with conservation of mass (Exner's equation), to model alluvial erosion and deposition along a 2D channel longitudinal profile:

$$q_s = k_g\left(S - S_c\right), \qquad S > S_c \tag{5}$$
$$q_s = 0, \qquad S \le S_c$$

$$\frac{\partial h}{\partial t} = -\frac{\partial q_s}{\partial x} = \frac{k_g\left[\max(S_{upstream} - S_c, 0) - \max(S_{downstream} - S_c, 0)\right]}{\partial x} \tag{6}$$

where q_s is the volumetric unit sediment flux (m^2/s), k_g is the transport coefficient (m^2/yr), S is the local channel slope (unitless), h is the channel-bed elevation (m), t is

time (yr) and x is distance along the channel from the drainage basin headwaters (m). The transport coefficient k_g can be estimated from an empirical relationship that depends on discharge and river type (Paola et al., 1992). Paola et al. (1992) estimated transport coefficients of approximately 1.0×10^4 and 7.0×10^4 (m^2/yr) for braided and meandering rivers, respectively, draining catchments of length equal to 100 kilometers and a mean annual precipitation of 1 m. We chose a value of 1.0×10^4 (m^2/yr) for our numerical experiments, which corresponds to braided, gravel-bed streams with relatively small drainage areas.

Threshold slope (S_c) values are sampled from a lognormal distribution with a mean of 1.4×10^{-3}. The coefficient of variation is varied between experiments but nominally has a value of 1.66 (i.e., the value calculated for naturally occurring rivers from the Church and Rood dataset). Once the threshold slope is determined for a given point along the channel longitudinal profile, that value is held constant for the prescribed sampling period, which we defined as the length of time that the channel is characterized by a particular threshold slope. The sampling period value may have a significant effect on both types of models considered in this paper because it determines whether the simulated alluvial channels remain in a state of low threshold slope for long periods of time or whether channels rapidly jump back and forth between states of enhanced or limited gravel entrainment.

The time scales of autogenetic and allogenic cut-and-fill cycles documented in natural river systems (e.g. Waters and Haynes, 2001; Mann and Meltzer, 2007; Harvey et al., 2011) can be used as a guide for choosing sampling periods for both models.

Autogenic processes that lead to changes in alluvial channel position through time (i.e., such as channel meandering and avulsion) have received much attention in the literature (Miall, 1996). However, very few studies have focus on autogenic processes that lead to alluvial channel incision. In the southwestern US, for example, the recurrence interval of Late Holocene arroyo cut and fill cycles for the San Pedro River that drains a region of 1,000 km^2 has been well constrained (Waters and Haynes, 2001). Based on the radiocarbon dates at the base of each scour, arroyos were incised and filled within 500 to 4,000 years with a predominant period of approximately 1,000 years. Similar trends were observed for Holocene cut and fill cycles for the Wildhorse Arroyo and Archuleta Creek of the Upper Cimarron River drainage basin in New Mexico (Mann and Meltzer, 2007). Radiocarbon and OSL dating of arroyo cycles in Buckskin Wash, UT revealed that at least 4 cut and fill cycles have occurred since 3 ka, and thus, the predominant period was between 500 to 1,000 years (Harvey et al., 2011). Although the periodicity of cut and fill cycles in the southwestern US would be different than that of channels located in other climates, we infer that 1,000 years is a reasonable value for the threshold slope sampling period. As such, we chose to hold threshold slopes constant over a period of 1,000 years, which is equal to the time step for both the isolated sedimentary basin and dynamically-coupled postorogenic foreland basin models.

Another important issue involving sediment transport within our models is whether the threshold slope should be uniform or varied along the channel profile during each sampling period. Observation of alluvial fan and valley floor channels reveal oscillations or instabilities in channel width and slope that appear to have wavelengths on

the order of 100 m to 10 km (Pelletier and DeLong, 2004). Therefore, it's possible to have discrete sections of the river profile with lower threshold slopes compared to the majority of the river profile. If this is the case, then gravel transport should primarily take place within these localized regions of increased slope and low width-to-depth ratios. This would suggest that models aimed at understanding the role of autogenetic oscillations in river systems should use spatially non-autocorrelated threshold slopes sampled at a relatively small spatial wavelength. However, channels also respond to climatic and autogenic forcings that trigger incision/aggradation along the entire river. Such cases would suggest that models aimed at understanding the role of allogenetic events in river systems should use threshold slope values that vary in time but are highly spatially autocorrelated along the channel longitudinal profile. An example of such an allogenetic event would be entrenchment along an entire river profile due to a major decrease in the ratio of sediment to water from upstream. In this paper we consider both spatially autocorrelated and spatially non-autocorrelated variations in threshold slope values. When threshold slope values are spatially non-autocorrelated in the numerical models, the threshold slope is sampled from a lognormal distribution and held constant over the sampling period for each alluvial channel pixel representing 1 km. When changes in threshold slope are spatially autocorrelated, a single threshold slope is sampled and applied along the entire alluvial channel profile for the given sampling period.

Our dynamically-coupled postorogenic foreland basin model is a 2D model that solves for the longitudinal profile of a channel evolving due to bedrock erosion and

flexural-isostatic response to erosional unloading of a mountain belt in addition to sediment transport in an adjacent foreland basin subject to stochastic changes in threshold slopes of entrainment. A 2D model is sufficient for the purposes of this study because at least some examples of long-runout gravels (e.g. the Ogallala Group conglomerates) are effectively 2D systems, i.e. gravels were primarily transported perpendicular to a long, linear mountain belt. While the model is 2D, it should be emphasized that variations in threshold slope implicitly include variations in channel geometry in the third dimension, i.e. channel width. The mountain belt topography at the beginning of each simulation represents the profile for a high elevation plateau (similar to that of the modern central Andes or Himalaya).

Bedrock channel erosion is simulated using the empirical stream-power equation (Howard and Kerby, 1983; Whipple and Tucker, 1999). We do not employ a threshold for plucking in our model, and thus, bedrock incision occurs as long as the slope is greater than zero. The following is the stream-power equation applied to the bedrock portion of the dynamically-coupled postorogenic foreland basin model:

$$\frac{\partial h}{\partial t} = -k_e A^m \left|\frac{\partial h}{\partial x}\right|^n = -k_e A^{1/2} S = -k_e x S \qquad (7)$$

where k_e is the bedrock erodibility (yr^{-1} for n = 1.0 and m = 0.5), A is the drainage basin area (m^2) and m and n are constants that determine the dependence of local erosion on discharge and channel slope. Evidence from theory and field studies predict that the ratio of m/n is to be near 0.5 (Whipple and Tucker, 1999). Although the slope exponent n can range between 0.66 and 2.0 depending on the relationship between slope and stream

power (shear stress), we chose to make the stream power linearly proportional to the slope (n = 1.0 and m = 0.5), consistent with the assumption of many other studies (e.g. Kirby and Whipple, 2001; Snyder et al., 2000). The range of bedrock erodibility (k_e) can be up to five orders of magnitude (10^{-2} to 10^{-7}) depending on lithology and the values of m and n (Stock and Montgomery, 1999). We chose a value of 10^{-6} yr^{-1} in order to scale the erosion rate to reasonable values (1 mm/yr or less) during the early portion of the simulations when the channel slopes in the bedrock portion of the model are highest. Alluvial deposition occurs within the bedrock drainage basin when erosion exceeds transport capacity and therefore, bedrock that is temporarily buried by alluvium does not erode until the overlying sediment is removed. In this way, the transition between the bedrock and alluvium is free to migrate laterally in response to the coupled evolution of the mountain belt-foreland basin system in the model.

Coupling a flexural model to a surface-process model is necessary because unloading of a mountain belt by bedrock incision should lead to isostatic rebound of the mountain belt, thus modifying sediment accommodation in the adjacent depositional basin. The flexural component of our model solves for the displacement of a thin elastic beam subjected to a spatially-distributed vertical load (Turcotte and Schubert, 1992):

$$D\frac{\partial^4 w(x)}{\partial x^4} + (\rho_m - \rho_s) g w(x) = L(x) \qquad (8)$$

where w is the deflection of the Earth's crust (m), D is the flexural rigidity (Nm), ρ_m is the density of the mantle (kg/m^3), ρ_s is the density of the mountain crust or foreland sediment (kg/m^3), g is gravity (m/s^2) and $L(x)$ is the topographic load (kg/ms^2). A Fourier

transform method is used to solve this PDE at each time step in the model following Watts (2001). Appropriate flexural rigidities for a high-elevation plateau can range from between $2.4x10^{23}$ and $3.0x10^{24}$ Nm when the Poisson's ratio is 0.25 and the Young's modulus is on the order of 10^{11} Pa (Stewart and Watts, 1997; Jordan and Watts, 2005). We chose to apply a flexural parameter of 150 km. The flexural parameter is defined as the following (Turcotte and Schubert, 1992):

$$\alpha = \left[\frac{4D}{(\rho_m - \rho_s)g} \right]^{1/4} \tag{9}$$

where α is the flexural parameter (km). Rearranging equation (9) and applying values from table 1 yields a flexural rigidity of approximately $6.8x10^{23}$ Nm, i.e. within the range of values for mountain belts with high plateaus. In the dynamically-coupled postorogenic foreland basin model, equation (8) is applied twice, first to determine the initial flexural profile beneath the topographic load at time zero and second to solve for rock uplift in response to erosional unloading at each time step. The flexural-isostatic component of the model was validated using comparison with analytic solutions for a line load. A mountain belt with an average height of 2.8 km and a width of 550 km triggers a forebulge that is 300-400 m high, a foredeep that is 290 km wide and maximum depth of 3 km when the rigidity is on the order of $6.0x10^{23}$ Nm. An issue that arose during the study is: should the forebulge be a significant topographic barrier between the foredeep and backbulge basins? A topographically significant forebulge would prevent gravel progradation out of the foredeep until the alluvial systems could aggrade to the forebulge spill point. Along the central Andes, however, there is no topographic expression of the forebulge despite

the low elevations observed 200-300 km from the thrust front in Bolivia and Northern Argentina (i.e. 150-500 m a.s.l.) (Horton and DeCelles, 1997). Conversely, the predicted forebulge region based on 2D flexural modeling in the Himalayan foreland basin is elevated approximately 300-400 meters above the Ganges plain (Bilham et al., 2003). Interpreting this relief as exclusively the result of forebulge uplift is complicated by the presence of pre-existing topography in the Central Indian Plateau. Although the Himalayan foreland may be an exception, topographically expressed forebulges are not commonly observed within modern terrestrial foreland basins, most likely due to erosion and/or dynamic subsidence (DeCelles and Giles, 1996; Catuneanu et al., 2000). In order for the model to predict a forebulge amplitude that is consistent with modern analogs (i.e. a maximum of 150-300 m a.s.l.), we beveled the forebulge crest at the beginning of the model down to the elevation of the initial fluvial profile. However, this initial topographic adjustment does not modify the flexural response of the forebulge, which is an important control for sediment accommodation and depositional basin regional slope, to postorogenic denudation of the adjacent mountain belt.

Parameters for both the isolated sedimentary basin and dynamically-coupled postorogenic foreland basin models are reported in table 1. The isolated sedimentary basin model simulates 10 million years of gravel progradation using a time step of 1 kyr using a pixel spacing of 1 km. The mean threshold slope is held constant at a value of 0.0014 and the threshold slope sampled from the lognormal distribution is applied to the entire channel profile. Simulations with a range of C_v values and a range of ratios of the sediment supply to the transport coefficient, q_s/k_g, were conducted to test the sensitivity

of gravel progradation to variations in these parameters. Sediment flux into the basin is held constant at a rate of 6 m^2/yr for the simulations with variable C_v, consistent with a q_s/k_g value of approximately 0.00075. We chose this value for sediment supply because it is equivalent to the average sediment supply coming out of the drainage basin during the period of highest sediment flux for each of the dynamically-coupled postorogenic foreland basin model simulations discussed in the Results section. Simulations for each C_v value are repeated 20 times and the reported results are an average of those model runs. Following the simulations with variable C_v and q_s/k_g, we also tested the sensitivity of gravel progradation rates and slopes to the presence or absence of spatial autocorrelation in threshold slope along the channel profile.

The dynamically-coupled postorogenic foreland basin model simulates 20 million years of gravel progradation using a time step of 1 kyr and pixel size of 10 km. The initial topographic profile for the bedrock drainage basin is an actively uplifting mountain belt with frontal slopes of 0.011 and a low-relief plateau interior. In the first simulation of this model type, threshold slopes are sampled from a lognormal distribution with a C_v of 1.66 and a mean value of 0.0014, i.e. equivalent to that of the Church and Rood (1983) dataset and therefore, representative of natural variations of slopes of channels with similar mean flow depths and grain sizes. Changes in threshold slope are spatially autocorrelated along the channel profile. Simulations with spatially non-autocorrelated changes in threshold slope are not considered here due to the results for comparing the isolated sedimentary basin model simulations with uniform or non-uniform changes in threshold slopes which we address in the Discussion section. Topographic surfaces are sampled for display at

0.0, 0.25, 1.0 and 20.0 Myr of simulation. We also report on additional simulations that were ran to test the effect of varying C_v and the sampling period on the evolution of postorogenic gravel progradation.

3. Numerical Modeling Results

Time-series results for regional slope and the position of the gravel front generated by the isolated sedimentary basin model with spatially autocorrelated changes in threshold slope are shown in Figure 2. Regional slopes (defined herein as the ratio of the relief of the depositional basin to the length of the basin) decrease systematically with increasing C_v. When the C_v value is greater than or equal to 1.0, the gravel wedge progrades at regional slopes that are less than the mean threshold slope (i.e., 0.0014). Thus, the model results suggest that natural rivers with a C_v of 1.66 and the channel conditions considered here can prograde at regional slopes significantly lower than that predicted by the paleoslope estimation method.

The location of the gravel front increases as a power-law function of time with an exponent that increases from approximately 0.5 to 0.8 as the C_v increases from 1 to 8 (Figure 2B). Even prior to 1.0 Myr, clastic-wedge progradation in the model is rapid and gravels begin to reach downstream distances that are considered "long-runout," i.e. greater than tens of kilometers (Heller et al., 2003), when the C_v is high. Beyond 1 Myr, progradation rates decrease to long term average rates of between 30-55 km/Myr with the precise value dependent on C_v. Increasing the C_v value by a factor of 8 increases the total progradation by less than a factor of 2 after 10 Myr. In such cases, gravel-bed channels with a C_v value comparable to natural rivers, i.e. 1.66, are able to transport gravel up to

approximately 400 km away from their source regions given sufficient geologic time (i.e. 10 Myr).

Numerical modeling studies have shown that alluvial basin slopes are also affected by sediment supply rates and sediment transport rates (Paola et al., 1992). Therefore, we conducted simulations to determine the variation in the behavior of this model with respect to variations in q_s/k_g (Figure 3). We chose not to test the sensitivity of gravel progradation to q_s and k_g individually because the regional slope of a clastic wedge is sensitive to the ratio between these two parameters rather than their individual values. The regional slopes shown in Figure 3 are the long-term regional slopes illustrated in Figure 2. When the C_v value is equal to 0, the resulting regional slopes are always greater than the mean threshold slope (i.e., 0.0014) calculated using equation (1). When threshold slopes are allowed to vary stochastically in time, long-term regional slopes decrease below the mean threshold slopes when q_s/k_g is less than 0.00125. Values of q_s/k_g above approximately 0.00125 correspond to cases in which sediment supply to the basin exceeds the ability of the gravel-bed channels to convey that sediment at the mean threshold slope. As the q_s/k_g ratio increases above 0.01, the long-term regional slope increases as a power-law of q_s/k_g. In such cases, the gravel channels aggrade with little dependence on the value of C_v. Conversely, values of q_s/k_g less than approximately 0.00125 correspond to cases in which the transport capacity at the calculated mean threshold slope approaches the sediment supply. The q_s/k_g value used in the analysis shown in Figure 2 is located in this region of the plot. In this situation the C_v value has a significant effect on the long-term regional slope. The relationship between regional

slope and q_s/k_g implies that sedimentary basins located adjacent to actively uplifting bedrock drainages may not be able to produce long-runout gravels with low regional slopes early on while sediment supplies are high. However, once active uplifting ends the regional slopes of the gravel-bed rivers can lower in response to infrequent periods of gravel transport.

Simulations with spatially autocorrelated and non-autocorrelated changes in threshold slope were conducted to test the sensitivity of gravel progradation to the presence/absence of spatial autocorrelations in threshold slope along the channel profile. We found that the sedimentary basin regional slopes were identical in the two cases, i.e. the results for spatially non-autocorrelated threshold slopes lie directly on top of the results obtained with spatially autocorrelated changes illustrated in Figure 3. In the case of spatially-autocorrelated threshold slopes, there are time periods of high effective transport rates (when threshold slopes are low across the entire basin). One might expect such cases to have higher effective transport rates compared to cases with spatially non-autocorrelated threshold slopes, but the results of our model do not support this expectation. In the case of spatially non-autocorrelated variations in threshold slope, gravel is transported in small episodic steps that are localized in space but occur commonly through geologic time. In the case of spatially autocorrelated variations in threshold slope, gravel is transported long distances in brief periods of unusually-low threshold slope, but then the basin experiences long periods with no transport anywhere until the entire basin can again achieve a transport condition characterized by a low threshold slope (e.g. a phase of active entrenchment). Therefore, the selection of either

spatially autocorrelated or non-autocorrelated changes in threshold slope does not significantly affect the results of either the isolated sedimentary basin or dynamically-coupled postorogenic foreland basin model, provided that sampling periods are small, i.e. on the order of millennia, compared to the duration of the model.

In addition to climatically or autogenically driven changes in threshold slope, tectonically driven changes in sediment supply and basin accommodation might affect both the regional slope and rates at which gravels are transported. Three types of results are reported for the dynamically-coupled postorogenic foreland basin model: (1) a description of how bedrock drainage relief, rock uplift rates, sediment supply rates and regional slope evolve during a simulation with a C_v value that is representative of natural rivers (i.e., 1.66); (2) a comparison of regional slope results for simulations with varying C_v values and (3) comparison of regional slope results for simulations with varying sampling periods.

The first 250 kyr of the simulation with a C_v value of 1.66 is marked by knickpoint retreat toward the plateau divide and an increase in basin average erosion rates (Figure 4A). Steep slopes and large contributing drainage areas (i.e. a proxy for discharge) lead to peak bedrock incision rates of 0.7 mm/yr near the mountain front. As such, high erosion rates near the mountain front begin to decrease slopes, and thus, erosion rates over the first 250 kyr as the main bedrock channel adjusts to slower (i.e., postorogenic) rock uplift rates. Overall, erosional adjustment of the drainage network over this time period has not significantly changed maximum erosion rates because the

topography after 250 kyr of simulation still closely resembles the original topography at the end of active deformation.

High basin-averaged erosion rates over the first 250 kyr following the cessation of active deformation leads to isostatic rebound, gravel input into the depositional basin and gravel front progradation. Erosional unloading of the mountain belt causes between 40 to 80 meters of rock uplift within the bedrock drainage basin over the first 250 kyr. Bedrock incision near the topographic divide is an order of magnitude less than incision at the mountain front in this time period, and as a result peak elevations increase by 40 m at the topographic divide. Overall, however, the mean elevation of the mountain belt is less than its original value, as it must be because only passive (isostatic) uplift is occurring. Isostatic rebound in the adjacent depositional basin increases proximal alluvial slopes because rock uplift exponentially decreases away from the mountain front. High basin average erosion rates during the first 250 kyr also lead to an increase in gravel flux into the depositional basin. Gravel flux reaches a maximum value of 10 m^2/yr and an average of approximately 5-6 m^2/yr at this time. As a consequence of increasing sediment supply and proximal channel slopes, the gravel front rapidly progrades approximately 150 km (i.e., a time averaged rate of 0.6 m/yr) from the mountain front in the first 250 kyr.

After 1 Myr of postorogenic time, basin-averaged erosion rates continue to decrease as the increase in peak elevations and bedrock channel slopes near the topographic divide is accompanied by a decrease in channel slopes near the mountain front (Figure 4A). In contrast to the initial 250 kyr, the highest erosion rates (0.6 mm/yr) are concentrated within the intermediate portion of the drainage basin instead of at the

mountain front. Reduced slopes and temporary sediment storage on the timescale of one hundred thousand years both act to limit erosion rates within the lower portion of the drainage system. Overall, the basin-averaged erosion rates at this point in time approach rates expected for postorogenic denudation (Matmon et al., 2003; Reiners et al., 2003). Erosion in the drainage basin leads to approximately 100 m and 140 m of surface uplift at the mountain front and topographic divide over the 0.75 Myr period. Isostatic rebound in the mountain belt is accompanied by subsidence in the forebulge region. As the surface topography lowers in the forebulge region and sediment flux remains high, the distal toe of gravel deposition migrates 100 km further from the mountain front.

Following 20 Myr of postorogenic denudation, basin-averaged erosion rates are on the order of 0.01 (mm/yr) as bedrock incision is concentrated near the topographic divide where steep slopes still persist (Figure 4A). Both peak elevation and erosion rates are comparable to values characteristic for postorogenic mountain belts that have only been eroding for tens of millions of years. Approximately 610 and 3780 m of exhumation occurs at the mountain front and topographic divide respectively over the 19 Myr period between 1 Myr and 20 Myr following the start of the simulation. Isostatic rebound at the mountain front due to erosional unloading of the mountain belt continues to steepen proximal foreland slopes. The distal toe of gravel deposition migrates an additional 300 km into the foreland basin in this time interval. Gravel progradation persists despite the factor of 3 decrease in gravel flux from the bedrock drainage system compared to the 0.25-1.0 Myr time interval (Figure 4B).

Changes in rock uplift and sediment supply rates have a significant effect on regional slope of the foreland basin. Figure 4B shows the time-dependent behavior of the regional slope. The most rapid change in regional slope (i.e. decreasing from values of $8.0x10^{-4}$ to values of approximately $5.0x10^{-4}$) occurs early in the simulation (prior to 200 kyr). Initially, increasing gravel flux from the bedrock drainage and non-uniform rock uplift rates near the mountain front lead to rapid gravel migration into the foredeep. This initial period is followed by a regional slope increase that lasts until approximately 1.5 Myr when the toe of the gravel wedge reached the distal foredeep and mean gravel flux from the mountain front begins to decrease. A topographically significant forebulge would impede gravel progradation beyond the foredeep as the distal toe is forced to aggrade to a forebulge spill point. In this case, however, the forebulge is eroded by the fluvial system to be in grade with the foredeep channel. Beyond 1.5 Myr, the gravel wedge toe is located in the forebulge to backbulge region where rock uplift rates are extremely low, and thus, the decrease in regional slope with time is predominantly controlled by decreasing gravel fluxes at the mountain front and the stochastic variation in threshold slopes.

Regional slopes are nearly linear in log-log space beyond 8-9 Myr of progradation, and thus represent a power-law relationship between regional slope and time (Figure 4B). It can also be argued that the decrease in regional slope is nearly linear as early as 2 Myr following the end of active uplift. When power-law curves are fit to the data in Figure 4B through linear regression of the log-transformed data between 2 and 8 Myr and between 8 and 20 Myr, the resulting power-law exponents are -0.11 and -0.34

respectively (with correlation coefficients of approximately -0.982 and -0.999 respectively). The differences in exponent values may be related to changes in sediment supply and foreland slopes near the toe of the gravel wedge.

Stochastic changes in threshold slope are the main mechanism for driving gravel progradation below the mean threshold slope, and thus have a significant effect on the long term decrease in the foreland basin regional slope with time. The variation in postorogenic regional slope as a function of the coefficient of variation of threshold slope (i.e., ranging between 0.0 and 3.0) and time is summarized in Figure 5. Heller et al. (2003) proposed that the gravel wedge must achieve and maintain a mean threshold slope to prograde gravel. Figures 4 and 5, however, show a decrease in regional slopes through time that suggests that gravel-dominated foreland basins do not maintain the predicted mean threshold slope (i.e., 0.0014 for our models) as time progresses. When there is no variation in threshold slope the long-term regional slope approaches the mean threshold slope predicted by equation (1) for the given parameters. However, the regional slope may not decrease to the mean threshold slope until the sediment input from the drainage basin approaches the transport capacity as demonstrated in Figure 3. When the C_v is 0.5, approximately 5.5 Myr of postorogenic gravel transport is required to reduce regional slopes below the calculated mean threshold slope value. Regional slopes never increased above the calculated mean threshold slope when the C_v is greater or equal to 1.0, and thus, the results suggest that the rate of gravel progradation for a given grain size far out into the foreland basin is strongly dependent on C_v and time in addition to the value of the transport coefficient. When power-law curves are fit to the data a negative correlation

exists between the C_v value and the power-law exponent for slope decrease after 7 Myr. The relationship between the C_v and power-law exponent is best approximated by a logarithmic function (correlation coefficient value of 0.9869). The negative relationship between C_v and the power-law exponent occurs because higher variability in threshold slopes increases the transport capacity of gravel-bed channels early on when sediment fluxes are high (i.e., between 0.25 and 1 Myr) and prevents significant aggradation. As such, regional slopes are already low at the beginning of the final phase of regional slope decrease.

Thus far we have shown how regional slopes respond to changes in the threshold slopes held constant over sampling periods of 1,000 years. However, gravel-bed channels that maintain threshold slopes over longer timescales may evolve differently than channels that vary threshold slopes over shorter timescales. Simulations using the dynamically-coupled postorogenic foreland basin model were run for different sampling periods to determine the dependence of gravel progradation on the sampling period duration (Figure 6). We define sampling period as the length of time over which the threshold slope for gravel transport is held constant before a new threshold slope is picked from the lognormal distribution. The curves illustrated in Figure 6 represent an average of trials conducted for sampling periods of 500 yr, 1 kyr, 10 kyr and 100 kyr.

The solid line in Figure 6 represents the sampling period applied to the simulation with a C_v of 1.66. The decrease in long-term regional slope (i.e., the trend in regional slope beyond 10 Myr) averaged over many trials remains unchanged as the sampling period is decreased by a factor of two or increased by one to two orders of magnitude. By

10 Myr, each of the sampling period simulations have experienced enough changes in threshold slope that the regional slope values resulting from the different sampling intervals converge. At shorter timescales, regional slopes for simulations with 10-100 kyr sampling periods are greater by a factor of two than the slopes for simulations with 0.5-1 kyr sampling periods. However, this trend may disappear when regional slope is averaged over more trials. Overall, the first order trend in regional slope, i.e. an increase in regional slope between 0.3 and 1 Myr followed by a long-term decrease below mean threshold slope, occurs in each simulation. As such, the first order behavior of the results for either model is not significantly biased by the size of the sampling period.

4. Discussion

Results from the simulations presented here suggest that allowing the threshold slope of gravel entrainment to vary stochastically through time in a lognormal fashion has a significant effect on the regional slopes at which gravels prograde in a depositional basin. When gravel progrades as a simple wedge with a constant sediment supply rate in the absence of tectonic influences, the regional slope reaches a constant value after only approximately 1 Myr that is dependent on C_v and q_s/k_g. According to our model results, gravel-bed channels that experience greater variation in threshold slope values develop lower regional slopes than those with relatively constant threshold slope values through time. This behavior is independent of whether the changes in threshold slope are localized (i.e., autogenically forced instabilities in the channel cross-section) or autocorrelated along the entire river profile (i.e., climatically forced entrenchment). If the q_s/k_g are sufficiently low and/or the C_v values are sufficiently high the regional slope can

be lower than the threshold slope calculated with the paleoslope estimation method during gravel transport. During postorogenic denudation of a coupled orogen-sedimentary basin system, the regional slope of a gravel-dominated basin decreases in a power-law relationship with time following an initial adjustment period of approximately 1 Myr. The timescale of the adjustment period depends on how rapidly the sediment supply begins to decrease following the end of active-uplift. Regional slope decrease initially occurs because channels are adjusted to higher sediment supply created by an actively uplifting orogen. However, the long-term regional decrease results from a combination of a decrease in sediment supply as the orogen loses relief and a stochastic variation in threshold slope. The duration and magnitude of the long-term regional slope decrease is dependent on the C_v, k_g and the initial relief of the orogen. A power-law relationship with time predicts that the postorogenic foreland basin regional slope can become much lower than the mean threshold slope predicted by paleoslope-estimation theory if the q_s/k_g ratio is sufficiently small. In the absence of major axial rivers, pre-existing topography and additional tectonic events that affect the postorogenic foreland basin, gravel units will continue to prograde away from the mountain belt through time over a period of more than 20 Myr.

The long-term regional slope of a sedimentary basin and rate of decrease in slope through time depend on the C_v value. Differences in the frequency of periods of lower-than-average threshold slopes as a function of C_v and time lead to the dependence of regional slope on the value of C_v. Simulations with larger coefficients of variation should experience a shorter amount of time between gravel-transporting intervals that can

transport gravel in the distal portions of the basin, which leads to an increasingly negative exponent value in the power-law relationship between regional slope decrease and time. This behavior has been described in the statistics literature as a "threshold-crossing" problem. For example, the probability of a threshold slope on the order of $1.0x10^{-4}$ is extremely low for a coefficient of variation of 1.0 (less than 4 percent frequency). When sediment supply rates and foreland basin slopes are highest during the early stages of postorogenic rebound, the time periods between gravel-transporting intervals is relatively short. As gravel is transported further into the sedimentary basin during periods of lower threshold slope, alluvial channel slopes decrease. Therefore, the duration between gravel-transporting intervals (i.e. those with sufficiently low threshold slopes) at the distal toe of the gravel wedge continually increases. Increasing the coefficient of variation to 3.0, increases the probability of threshold slopes on the order of $1.0x10^{-4}$ (approximately 16 percent frequency). Although these probabilities seem small, the number of millennia out of a 20 million year simulation where the threshold slope is on the order of 10^{-4} can be quite large (10^2 to 10^3 millennia).

The results for both models suggest that gravels can prograde hundreds of km at low regional slopes over a few million years when sample periods are on the order of millennia. Although 1,000 years is an appropriate (mid-ranged) value for the sampling period, the timescales of cut and fill cycles can vary between 500 to 4,000 years. This motivates the question: as channels spend longer periods of time at a given threshold slope (i.e., longer sampling periods), must the long term progradation of gravels happen more rapidly or at significantly lower slopes than channels that more frequently change

their threshold slopes? We infer from our model results that the long-term progradation rates (> 10 Myr) and foreland behavior are approximately time invariant for the tested sampling periods (Figure 6). As long as the duration of the gravel transport is much larger than the sampling period, then the long term gravel progradation will occur at similar rates and regional slopes. At shorter timescales, autogenic or climatic processes that lead to changes in flow depth, and thus threshold slopes, every 0.1-1 kyr are more efficient at prograding gravel than changes in flow depth on timescales of 10-100 kyr when the C_v is representative of modern rivers.

If variations in channel width-to-depth ratio over geologically brief timescales (i.e., 0.001 to 1.0 Myr) occurred during gravel transport, then the internal stratigraphic architecture of the gravel deposits should reflect this behavior. The Buckhorn Conglomerate member of the Lower Cretaceous Cedar Mountain Formation located in southern Utah and the Upper Conglomerate of the Lower Cretaceous Cloverly Formation of central Wyoming, for example, are composed of coalesced lenticular conglomerate bodies that contain planar to trough cross-stratification (DeCelles and Burden, 1992; Currie, 1998). Erosional surfaces that mark a cycle of cutting have not been identified within the coalesced gavel bodies; however, such surfaces may be difficult to detect within continuous conglomerate successions (Miall, 1996). A lack of developed flood plain units within or laterally correlative to the conglomerates and the lateral continuity of gravelly to coarse sandy deposits lead to the interpretation that the gravel bodies represent deposition in a series of unstable, interconnected, braided fluvial channels that reworked the entire width of paleovalleys in which the gravels were deposited. Due to the

lateral instability of braided channels and low accommodation rates during deposition it is not surprising that soils and fine grained floodplain deposits were not preserved in the valley fill, and thus, evidence of periods of channel stability or entrenchment over geologically-brief periods of time may only be preserved in the unconformity surfaces adjacent to the paleovalleys. Evidence for cycles of channel incision and paleosol formation during the deposition of conglomerates is seen within the basal Shinarump conglomerate of the Upper Triassic Chinle Formation (Blakey and Gubitosa, 1984; Hasiotis et al., 2000). Gravelly to sandy bodies within the Shinarump conglomerate paleovalley fill were also interpreted to be deposited by an unstable, braided river system due to the lack of fine grained, horizontally laminated floodplain deposits and the abundance of trough-cross stratified dunes and planar cross-stratified bars (Blakey and Gubitosa, 1984). Significant scour surfaces between individual channel stories with relief ranging between 1-2 meters are observed within outcrops located in northern Arizona and southern Utah. However, its unclear if this magnitude of incision was accomplished over a significant period of time or during a single flood event. Ephemeral alluvial rivers with drainage basin areas on the order of 50-100 km^2 have been observed to incise their channel beds up to 2 m during floods where average flow depths were between 0.3 to 2m (Hassan et al., 1999; Hooke and Mant, 2000). In the Petrified Forest National Park of Northern Arizona, multiple cycles of valley cut-and-fill have been identified in the lower part of the Chinle Formation (Hasiotis et al. 2000). Lenticular channel deposits of the Shinarump member cut into contemporaneous overbank deposits that show slight to moderate pedogenesis.

Clear evidence for cycles of entrenchment and periods of low deposition adjacent to the active channel can be found within the internal stratigraphic architecture of the Tertiary Ogallala Group observed in Nebraska. Valley fill deposits of the Ogallala Group are separated by major erosional surfaces and contain Miocene fossil assemblages of distinctly different ages, which suggest multiple cycles of cut and fill occurred after the initial incision of the main paleovalleys (Diffendal, 1982). In some outcrops the younger deposits cut completely through to basal Ogallala and into the underlying mid-Tertiary stratigraphy. Further south in Texas and New Mexico, cycles of deposition and pedogenesis can be seen within the fine sand to coarse silt lithofacies of the Ogallala Group. In some outcrops eolian deposits that contain cycles of deposition and pedogenesis cap fluvial sections in the paleovalley fill and paleo-uplands (Gustavson and Holliday, 1999).

Cycles of entrenchment and fill, that cause periods of low threshold slopes over millennia timescales, have been directly observed and inferred from Pleistocene and Holocene alluvial fan and valley floor river outcrops. Although climatic conditions for the Quaternary may be quite different from other periods of time, cutting and filling cycles are not limited to the Quaternary. For example, DeCelles et al. (1991) interpreted a series of 5^{th} order lithosomes and 5^{th} order surfaces (as defined by Miall, 1995) within alluvial fan deposits from the Paleocene Beartooth Conglomerate in Montana as a cycle of entrenchment and backfilling. Holbrook (2001) observed a continuum of channel-form bounding surfaces within the Cretaceous Muddy Sandstone of southeastern Colorado that represent river scour at different scales. Nested valleys or bundles of channel belts

truncated and bound by higher order surfaces were present throughout the formation. These nested valleys were interpreted to analogous to modern cut and fill deposits that form over timescales of 10^3 years. Based on the observation of the Western US long-runout gravels and other evidence for entrenchment and fill cycles contained within the rock record, invoking stochastic variations in threshold slope to drive gravel transport at low gradients over long distances is realistic.

Our modeling results suggest that ancient orogens that have undergone postorogenic denudation under ideal conditions (e.g. sufficient relief and appropriate drainage lithologies for generating gravel) should produce long-runout gravels if given sufficient time. However, it's unclear if long-runout gravels have not been described for other ancient orogens outside of the western U.S. because they were not recognized as having been transported considerable distances from their source region or the conditions for producing long-runout gravels are rare. One explanation for why long-runout gravels might be rare is that the ability of gravel clasts to resist grain size reduction through abrasion may be an important factor (Kodama, 1994; Lewin and Brewer, 2002). As clasts saltate along the channel bed or are at rest, collisions with the bed or other clasts cause the grain size to decrease by shedding off smaller particles. Grain size reduction generally follows a power-law with distance from the source of the clasts. Although channel conditions may be suitable for transporting gravel out to the distal foreland basin, the gravel may be broken down into sand sized grains within 50-100 km from where they were sourced depending on the lithology. Interestingly, the Shinarump and Lower Cretaceous gravels are dominated by resistive lithologies. For example, approximately 24

and 72 percent of point counts within samples from the Buckhorn Conglomerate were composed of chert nodules and monocrystalline quartz (Currie, 1998). Chert and quartzite are also prevalent within the Lakota, Cloverly and Shinarump conglomerates (Blakey and Gubitosa, 1984; Zaleha et al., 2001). We infer from the lithologic trends of Lower Cretaceous and Shinarump conglomerates that gravels require lithologies that are resistant to grain size reduction in order to be transported 100s of kilometers from their source regions; although, the Ogallala Group conglomerates are an exception.

Another possible explanation for why ancient orogens do not commonly produce long-runout gravels is due to the lithology of the eroding drainages. Toward the eastern edge of the central Andes, for example, Tertiary synorogenic sediments are being exhuming within the Subandean Zone, which is the active fold and thrust belt today. Within the Tertiary units, the Yecua and Tariquia Formations that make up approximately half the thickness of the Tertiary units, mainly compose of sandstones and mudstones with some conglomerate units present (Uba et al., 2005). Consequently, studies of the large megafans that drain this region in southern Bolivia and northern Argentina observed limited gravel to abundant sand and mud along the entire megafan profile (Horton and DeCelles, 2001). Conglomerates should be absent from the rock record if material that is prone to erode into finer grain sizes is being exhumed in the bedrock drainage regions that are the predominant supply of sediment to the depositional basin.

5. Conclusions

The evolution of gravel transport within foreland basins is significantly influenced by the stochastic variation in threshold slopes. When the gravel supply is held constant and subsidence is negligible, the regional slope of a prograding gravel wedge reaches a long-term value that is dependent on the values q_s/k_g and both the mean and coefficient of variation of the threshold slope of entrainment. When the C_v value is less than one, the effective regional slope remains equal to or greater than the mean threshold slope and gravel progradation is minimized. However, when the C_v value is greater than one and the basin sediment supply is low, gravel can be transported at regional slopes that are well beneath threshold slopes predicted by the paleoslope estimation method. As such, caution should be exercised when evaluating regional slopes measured from the rock record in a tectonic context.

The results of our dynamically-coupled postorogenic foreland basin model show that the decrease of foreland basin regional slopes closely follows a power-law relationship with time, although variability in sediment supply and rock uplift cause significant scatter in foreland basin slopes through time. This implies that gravel will continue to prograde in the foreland basin following the end of active uplift for a significant period of time. The power-law regional slope decrease with time observed in the model does not appear to depend on the sampling period beyond 10 Myr as long as the period does not approach a million years. The spatial autocorrelation of threshold slope change also has little effect on the first order behavior of regional slope decrease, and thus, either climatic or autogenic forcings should be sufficient to prograde gravel at extremely low regional slopes.

Our model results suggest that under ideal conditions, long-runout gravels can be formed within a period that is on the order of a few million years if threshold slopes are variable through time. The three described long-runout gravels of the western US contain lithologies that are highly resistive to grain size reduction through abrasion which we infer to also be a necessary condition for the transport of gravel long distances. Both macroscale and internal geometries within the Lower Cretaceous and Ogallala gravels support the possibility of significant variation in channel width-to-depth ratios through time. Therefore, the Shinarump, Lower Cretaceous and Ogallala gravels need not have required a tectonically driven increase in slope above the observed slopes today to transport large distances from where they were sourced.

Acknowledgements

This research was supported in part by ExxonMobil funding. We thank Doug Jerolmack for helpful conversations.

References

Allmendinger, R.W., Jordan, T.E., Kay, S.M., and Isacks, B.L., 1997, The Evolution of the Altiplano-Puna Plateau of the Central Andes: Annual Review of Earth and Planetary Sciences, v. 25, p. 139-174.

Andrews, E.D., 1984, Bed-material entrainment and hydraulic geometry of gravel-bed rivers in Colorado: Geological Society of America Bulletin, v. 95 (3), p. 371-378.

Bilham, R., Bendick, R., and Wallace, K., 2003, Flexure of the Indian Plate and Intraplate Earthquakes: Proceedings of the Indian Academy of Sciences-Earth and Planetary Sciences, v. 112, p. 1-14.

Blakey, R.C., and Gubitosa, R., 1984. Controls of sandstone body geometry and architecture in the Chinle Formation (Upper Triassic), Colorado Plateau: Sedimentary Geology, v. 38, p. 51-86.

Bull, W.B., 1997, Discontinuous ephemeral streams: Geomorphology, v. 19, p. 227-276.

Catuneanu, O., Sweet, A.R., and Miall, A.D., 2000, Reciprocal stratigraphy of the Campanian-Paleocene Western Interior of North America: Sedimentary Geology, v. 134, p. 235-255.

Church, M., and Rood, K., 1983, Catalogue of Alluvial River Channel Regime Data: Vancouver, British Columbia, Canada, University of British Columbia, Department of Geography.

Currie, B.S., 1998, Upper Jurassic-Lower Cretacueous Morrison and Cedar Mountain Formations, NE Utah-NW Colorado: Relationships between nonmarine deposition and early cordilleran foreland basin development: Journal of Sedimentary Research, v. 68, p. 632-652.

DeCelles, P.G., 1986, Sedimentation in a tectonically partitioned, nonmarine foreland basin – the Lower Cretaceous Kootenai Formation, southwestern Montana: Geological Society of America Bulletin, v. 97, p. 911-931.

DeCelles, P.G., and Burden, E.T., 1992, Non-marine sedimentation in the overfilled part of the Jurassic-Cretaceous Cordilleran foreland basin: Morrison and Cloverly Formations, central Wyoming, USA: Basin Research, v. 4, p. 291-313.

DeCelles, P.G., and Giles, K.A., 1996, Foreland basin systems: Basin Research, v. 8, p. 105-123.

DeCelles, P.G., Gray, M.B., Ridgeway, K.D., Cole, R.B., and Pivnik, D.A., 1991, Controls on synorogenic alluvial fan architecture, Beartooth Conglomerate (Paleocene), Wyoming and Montana: Sedimentology, v. 38, p. 567-590.

Diffendal, R.F., Jr., 1982, Regional implications of the geology of the Ogallala Group (upper Tertiary) of southwestern Morrill County, Nebraska, and adjacent areas: Geologic Society of America Bulletin, v. 93, p. 964-976.

Gustavson, T.C., and Holliday, V.T., 1999, Eolian sedimentation and soil development on a semiarid to subhumid grassland, Tertiary Ogallala and Quaternary Blackwater Draw

Formations, Texas and New Mexico High Plains: Journal of Sedimentary Research, v. 69, p. 622-634.

Gustavson, T.C., and Winkler, D.A., 1988, Depositional facies of the Miocene-Pliocene Ogallala Formation, northwestern Texas and eastern New Mexico: Geology, v. 16, p. 203-206.

Harvey, J.E., Pederson, J.L., and Rittenour, T.M., 2001, Exploring relations between arroyo cycles and canyon paleoflood records in Bucksin Wash, Utah: Reconciling scientific paradigms: Geological Society of America Bulletin, v. 123, p. 2266-2276.

Hasiotis, S.T., Demko, T.M., and Dubiel, R.F., 2000. Shinarump incised valley cut-and-fill deposits, paleosols, and ichnofossils in the lower part of the Upper Triassic Chinle Formation, Petrified Forest National Park, Arizona: It really does exist, and it has regional stratigraphic implications: Geological Society of America Abstracts with Programs, v. 33, p. 23.

Hassan, M.A., Schick, A.P., and Shaw, P.A., 1999, The transport of gravel in an ephemeral sandbed river: Earth Surface Processes and Landforms, v. 24, p. 623-640.

Heller, P.L., Dueker, K., and McMillan, M.E., 2003, Post-Paleozoic alluvial gravel transport as evidence of continental tilting in the U.S. Cordillera: Geological Society of America Bulletin, v. 115 (9), p. 1122-1132.

Holbrook, J., 2001, Origin, genetic interrelationships, and stratigraphy over the continuum of fluvial channel-form bounding surfaces: an illustration from middle Cretaceous strata, southeastern Colorado: Sedimentary Geology, v. 144, p. 179-222.

Hooke, J.M., and Mant, J.M., 2000, Geomorphological impacts of a flood event on ephemeral channels in SE Spain: Geomorphology, v. 34, p. 163-180.

Horton, B.K., DeCelles, P.G., 1997, The modern foreland basin system adjacent to the Central Andes: Geology, v. 25, p. 895-898.

Horton, B.K., and DeCelles, P.G., 2001, Modern and ancient fluvial megafans in the foreland basin system of the Central Andes, southern Bolivia: implications for drainage network evolution in fold-thrust belts: Basin Research, v. 13, p. 43-63.

Howard, A.D, and Kerby, G., 1983, Channel changes in badlands: Geological Society of America Bulletin, v. 94, p. 739-752.

Jones, L.S, and Harper, J.T., 1998, Channel avulsions and related processes, and large-scale sedimentation patterns since 1875, Rio Grande, San Luis Valley, Colorado: Geology Society of America Bulletin, v. 110, p. 411-421.

Jordan, T.A., and Watts, A.B., 2005, Gravity anomalies, flexure and elastic thickness structure of the India-Eurasia collisional system: Earth Planetary Science Letters, v. 236, p. 732-750.

Kirby, E., and Whipple, K., 2001, Quantifying differential rock-uplift rates via stream profile analysis: Geology, v. 29, p. 415-418.

Kodama, Y., 1994, Downstream changes in the lithology and grain size of fluvial gravels, the Watarase River, Japan: Evidence of the role of abrasion in downstream fining: Journal of Sedimentary Research, v. A64, p. 68-75.

Leopold, L.B., Wolman, M.G., and Miller, J.P., 1964, Fluvial processes in geomorphology: San Francisco, W.H. Freeman and Company.

Lewin, J., and Brewer, P.A., 2002, Laboratory simulation of clast abrasion: Earth Surface Processes and Landforms, v. 27, p. 145-164.

Mann, D.H., and Meltzer, D.J., 2007, Millennial-scale dynamics of valley fill over the past 12,000 14C yr in northeastern New Mexico, USA: Geological Society of America Bulletin, v. 119, p. 1433-1484.

Matmon, A., Beirman, P.R., Larsen, J., Southworth, S., Pavich, M., and Caffee, M., 2003, Temporally and spatially uniform rates of erosion in the southern Appalachian Great Smoky Mountains: Geology, v. 31, p. 155-158.

McMillan, M.E., Angevine, C., and Heller, P.L., 2002, Postdepositional tilt of the Miocene-Pliocene Ogallala Group on the western Great Plains: Evidence of late Cenozoic uplift of the Rocky Mountains: Geology, v. 30, p. 63-66.

Meyer-Peter, E., and Mueller, R., 1948, Formulas for bed-load transport, *in* Proceedings, International Association for Hydraulic Structures Research Meeting, 2nd, Stockholm, Sweden, p. 39-64.

Miall, A.D., 1995, Description and interpretation of fluvial deposits: a critical perspective: discussion: Sedimentology, v. 42, p. 379-384.

Miall, A.D., 1996, The Geology of Fluvial Deposits: Sedimentary Facies, Basin Analysis, and Petroleum Geology: New York, Springer, 582 p.

Paola, C., Heller, P.L., and Andgevine, C.L., 1992, The large-scale dynamics of the grain-size variation in the alluvial basins, 1: Theory: Basin Research, v. 4, p. 73-90.

Paola, C., and Mohrig, D., 1996, Palaeohydraulics revisited: palaeoslope estimation in coarse-grained braided rivers: Basin Research, v. 8, p. 243-254.

Parker, G., 1978, Self-formed straight rivers with equilibrium banks and mobile bed-Part II, The Gravel River: Journal of Fluid Mechanics, v. 89, p. 127-148.

Patton, P.C., Schumm, and Stanley, A., 1975, Gully erosion, northwestern Colorado; a threshold phenomenon: Geology, v. 3, p. 88-89.

Pelletier, J.D., and DeLong, S., 2004, Oscillations in arid alluvial channels: Geology, v. 32, p. 713-716.

Reiners, P.W., Zhou, Z., Ehlers, T.A. Xu, C., Brandon, M.T., Donelick, R.A., and Nicolescu, S., 2003, Post-orogenic evolution of the Dabi Shan, eastern China from (U-Th)/He and fission track thermochronology: American Journal of Science, v. 303, 489-518.

Schumm, S.A., and Hadley, R.F., 1957, Arroyos and semiarid cycle of erosion: American Journal of Science, v. 255, p. 161-174.

Shields, A., 1936, Anwendung der Aehnlichkeitsmechanik und der Turbulenzforschung auf die Geschiebebewegung, Mitt. Preuss. Versuchsanst. Wasserbau Schiffbau 26, p. 36.

Snyder, N.P., Whipple, K.X., Tucker, G.E., and Merritts, D.J., 2000. Landscape response to tectonic forcing: Digital elevation model analysis of stream profiles in the Mendocino triple junction region, northern California: Geological Society of America Bulletin, v. 112, p. 1250-1263.

Stewart, J., and Watts, A.B., 1997, Gravity anomalies and spatial variations of flexural rigidity at mountain ranges: Journal of Geophysical Research, v. 102, p. 5327-5352.

Stock, J., and Montgomery, D., 1999, Geologic constraints on bedrock river incision using the stream power law: Journal of Geophysical Research, v. 104, p. 4983-4993.

Turcotte, D.L., 1997, Fragmentation: Cambridge, Cambridge University Press, Fractals and Chaos in Geology and Geophysics, 2nd edition, p. 29-55.

Turcotte, D.L., and Greene, L., 1993, A scale-invariant approach to flood frequency analysis: Stochastic Hydrology and Hydraulics, v. 7, p. 33-40.

Turcotte, D.I., and Schubert, G., 1992, Geodynamics, Application of Continuum Physics to Geological Problems: New York, Wiley.

Uba, C.E, Heubeck, C., and Hulka, C., 2005, Facies analysis and basin architecture of the Neogene Subandean synorogenic wedge, southern Bolivia: Sedimentary Geology, v. 180, p. 91-123.

Waters, M.R., and Haynes, C.V., 2001, Late Quaternary arroyo formation and climate change in the American Southwest: Geological Society of America Bulletin, v. 29, p. 399-402.

Watts, A.B., 2001, Isostacy and Flexure of the Lithosphere: Cambridge. Cambridge University Press.

Whipple, K., and Tucker, G., 1999, Dynamics of the stream-power river incision model: Implications for height limits of mountain ranges, landscape response timescales, and research needs: Journal of Geophysical Research, v. 104, p. 17661-17674.

Zaleha, M.J., Way, J.N., and Suttner, L.J., 2001, Effects of syndepositional faulting and folding on early Cretaceous rivers and alluvial architecture (Lakota and Cloverly Formations, Wyoming, U.S.A.): Journal of Sedimentary Research, v. 71, p. 880-894.

Tables, Figures and Figure Captions:

TABLE 1. PARAMETERS FOR MODEL SIMULATIONS

Parameter	Isolated Sedimentary Basin Model	Dynamically-Coupled Postorogenic Foreland Basin Model
Model Duration (yr)	1.0×10^7	2.0×10^7
ρ_m (kg/m^3)	NA	3300
ρ_c (kg/m^3)	NA	2750
k_e (yr^{-1})	NA	1.0×10^{-6}
k_g (m^2/yr)	1.0×10^4	1.0×10^4
$\overline{S}_c$ (unitless)	0.0014	0.0014

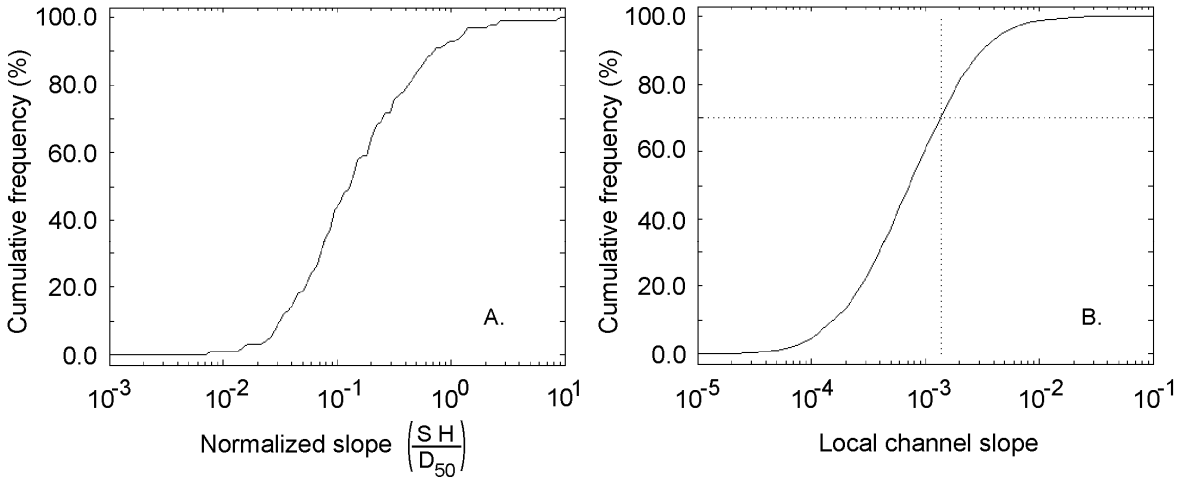

Figure 1: Channel slope statistics applied to calibrate the variation in threshold slope. (A) Cumulative frequency distribution for normalized slopes determined from slope data collected by Church and Rood (1983) for gravel-dominated rivers in North America. (B) Cumulative frequency distribution for model threshold slopes. Vertical, dotted line

represents the location of the threshold slope that is predicted by paleoslope estimation theory.

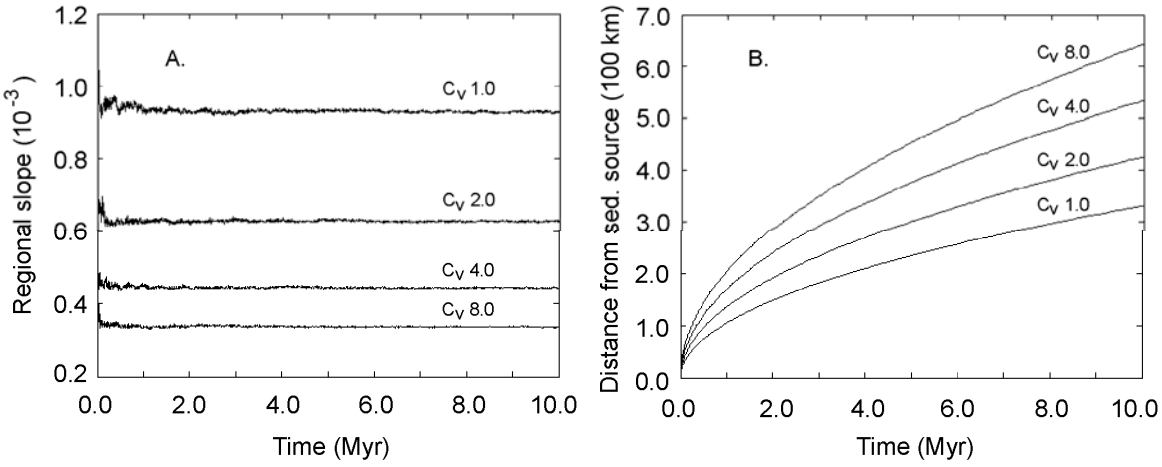

Figure 2: Isolated sedimentary basin model results. (A) Average regional slopes and (B) gravel front positions through time for gravel-bed channels with different C_v values.

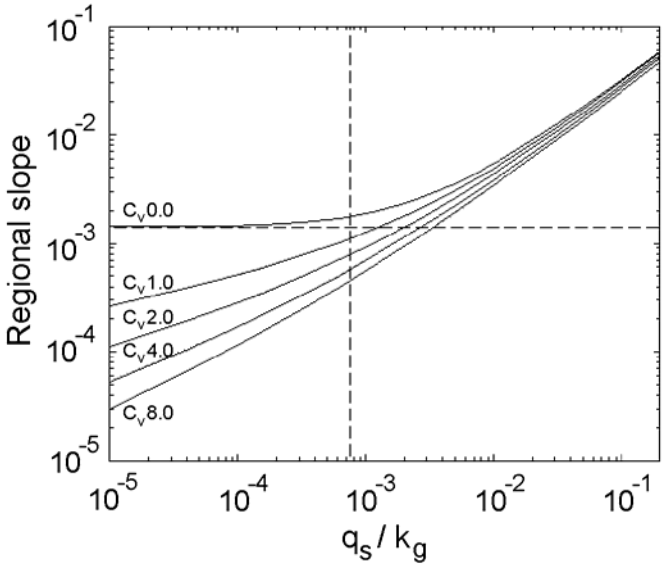

Figure 3: Relationship between the regional slope of a prograding clastic wedge in an isolated sedimentary basin and the ratio of sediment supply to transport coefficient for

various values of C_v. The solid curves represent simulations with correlated changes in threshold slope along the entire channel profile. The dashed horizontal line represents the mean threshold slope of 0.0014 and the dashed vertical line represents the sediment supply to transport coefficient ratio for simulations shown in Figure 2.

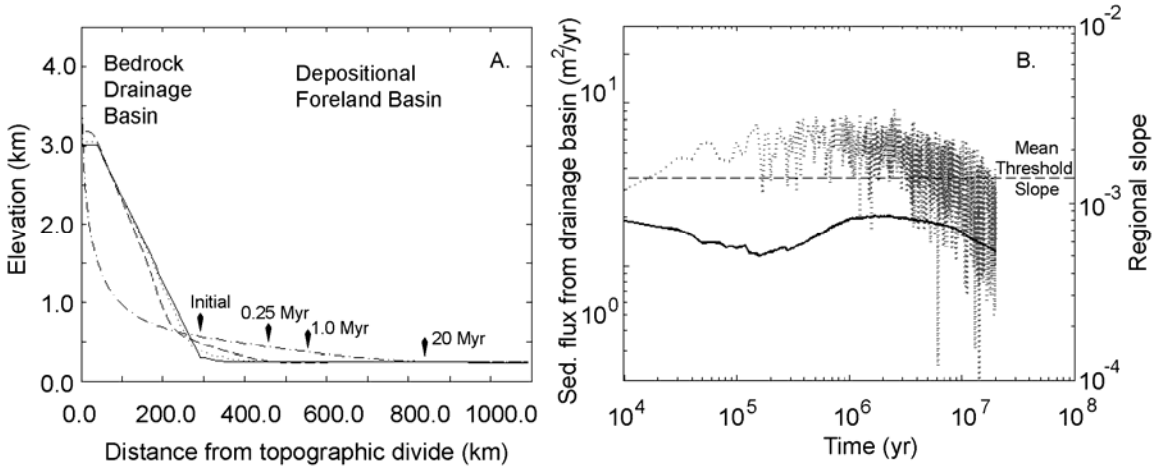

Figure 4: Dynamically-coupled postorogenic foreland basin model results for the simulation with a C_v value of 1.66. (A) Topographic cross sections and (B) sediment flux and regional slope time-series following a cessation of active uplift. The solid, dotted, dashed and dashed-dotted dark lines in Figure 4A represent snap-shots in time of topography at intervals of 0, 250 kyr, 1 Myr and 20 Myr following the cessation of tectonically driven rock uplift. The vertical tick marks represent the downstream limit of gravel deposition during those instants in time. In Figure 4B the regional slope and sediment influx rate are represented by the solid and dotted lines respectively.

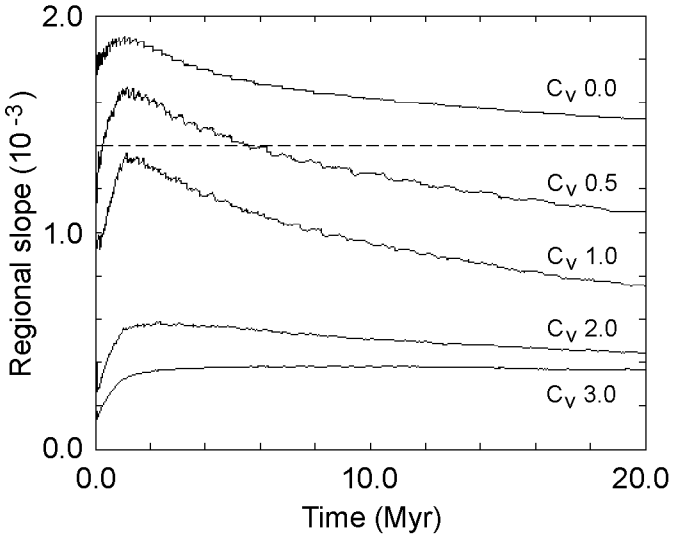

Figure 5: A summary of the dynamically-coupled postorogenic foreland basin model simulations for the coefficient of variation of threshold slope. The mean threshold slope calculated using equation (1) for the assumed channel conditions is represented by the dashed line. Each sensitivity study curve is an average of individual trials for a given C_v value.

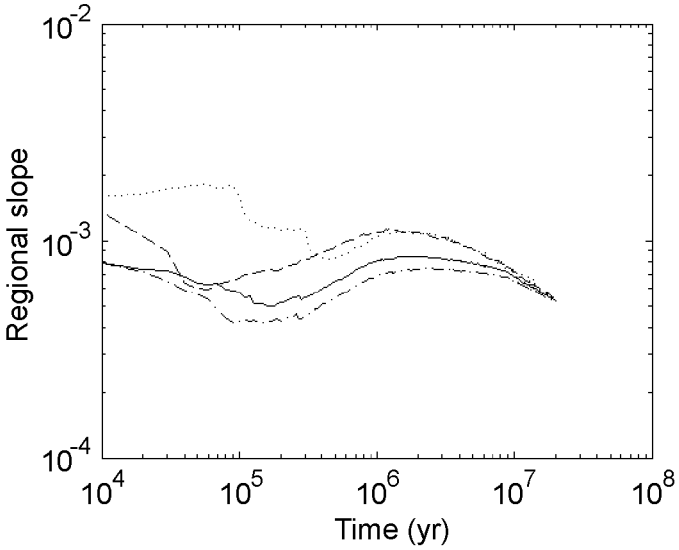

Figure 6: Resulting regional slopes for a range of sampling intervals for the dynamically-coupled postorogenic foreland basin model. The dot-dashed, solid, dashed and dotted lines represent 500 yr, 1 kyr, 10 kyr and 100 kyr sampling intervals respectively.

APPENDIX B: SIMULATING FORELAND BASIN RESPONSE TO MOUNTAIN BELT KINEMATICS AND CLIMATE CHANGE FOR THE CENTRAL ANDES: A NUMERICAL ANALYSIS OF THE CHACO FORELAND IN SOUTHERN BOLIVIA

Manuscript for submission to Tectonics

Todd M. Engelder [a] and Jon D. Pelletier
Department of Geosciences, University of Arizona, 1040 E. Fourth St., Tucson AZ, 85721, USA,

[a]*Corresponding Author, email: engelder@email.arizona.edu, fax: (520) 621-2672*

Abstract

The role of crustal thickening, lithospheric delamination, and climate change in driving surface uplift in the central Andes in southern Bolivia and changes in the creation of accommodation space and depositional facies in the adjacent foreland basin has been a topic of debate over the last decade. Interpretation of structural, geochemical, geomorphic and geobiologic field data collected from the region has led to two proposed end-member Tertiary surface uplift scenarios. A "gradual uplift" model proposes that the rate of surface uplift has been relatively steady since deformation propagated into the Eastern Cordillera during the Late Eocene (McQuarrie et al., 2005). In this scenario, the mean elevation of the region was > 2 km a.m.s.l. by the Late Miocene or earlier. Alternatively, a "rapid uplift" model suggests that the mean elevation of the Altiplano was < 1 km a.m.s.l. and that the peaks of the Eastern Cordillera were more than 2 km below their modern elevations until 10 Ma (Garzione et al., 2008). Determining which of these uplift scenarios is most consistent with the stratigraphic record is complicated by global climate changes and lithospheric delamination during this period. In this study, we use a coupled

mountain belt/sediment transport model to predict the foreland basin stratigraphic response to end-member surface uplift scenarios, lithospheric delamination and climate change. Our model results indicate that the location and height of the migrating deformation front plays the dominant role in controlling changes in accommodation space and grain size within the foreland basin. Changes in accommodation and sediment supply rates related to climate change and lithospheric delamination events appear to be secondary to crustal thickening and propagation of the deformation front. Based on stratigraphic data, the Eastern Cordillera likely gained significant elevation prior to 10 Ma, which is in contrast with recent proposals that most of the modern elevation was obtained during the Late Miocene.

Keywords- sediment transport, foreland basin, central Andes, surface uplift, delamination, climate change

1. Introduction

Sediments eroded from mountain belts are primarily deposited in foreland basins, which are elongate troughs created by flexural loading of the lithosphere adjacent to mountain belts (DeCelles and Giles, 1996). Foreland-basin stratigraphy is recognized to be a useful dataset for reconstructing climate and crustal deformation histories within ancient mountain belts (e.g., Heller et al., 1988; DeCelles et al., 1998; Marzo and Steel, 2000, Uba et al., 2007). The fluvial systems that transport the sediment from mountain belts are sensitive to changes in sediment supply, discharge and sediment accommodation rates, and thus, the foreland-basin stratigraphy deposited by these systems is a partial record of changes in climate and the geometry of the mountain belt load through time. The flexural profile of foreland accommodation depends on the rigidity of the lithosphere that is underthrusted beneath the mountain belt as well as the width and elevation of the mountain belt load. If the foreland basin geometry and rigidity of the underthrusted lithosphere are constrained, then it is possible to infer changes in the mountain belt load that occurred during the development of the foreland basin. As such, numerous studies have inferred tectonic histories for ancient mountain belts by fitting foreland basin geometries predicted by a coupled mountain belt and foreland basin numerical model to observed foreland basin isopach data (e.g., Toth et al., 1996; Ford et al., 1999; Garcia-Castellanos et al., 2002; Prezzi et al., 2009).

The eastern margin of the central Andes (i.e., the portion of the mountain belt that is to the east of the Altiplano plateau) in southern Bolivia is an ideal region for constraining Late-Cenozoic changes in mountain-belt geometry and climate through

numerical modeling of foreland-basin stratigraphy because the sediments preserved in the foreland basin have been well described in the literature and field and laboratory constraints have been reported in the literature for shortening and exhumation rates in the hinterland for the period of time over which the eastern margin of the central Andes formed. A W-E transect of the Cenozoic foreland-basin stratigraphy is exposed within the retroarc fold-and-thrust belt. Detailed isopach maps and stratigraphic sections for the Cenozoic foreland-basin stratigraphy have been developed based on a combination of measured sections from the fold-and-thrust belt and correlations between well log data and 2-D seismic data (Sempere et al., 1997; DeCelles and Horton, 2003; Echavarria et al., 2003; Uba et al., 2005; Uba et al., 2006). In addition to data from the foreland basin, the timing and magnitude of shortening and exhumation within the mountain belt has been constrained by field mapping and thermochronology (McQuarrie et al., 2002; Muller et al., 2002; Oncken et al., 2006; Ege et al., 2007; Barnes et al., 2008). At a larger scale, the Andes as a whole have been an invaluable natural laboratory for exploring feedbacks between climate and rock uplift (Montgomery et al., 2000; Strecker et al., 2007).

An unresolved issue for the central Andes is: when did the topography of the central Andes rise to its modern elevation? The classic model for the topographic development of the central Andes posits that the mean topography reached near-modern elevation following Neogene crustal thickening within the Subandean zone; thus, earlier crustal thickening within the Eastern Cordillera was not sufficient for the central Andes to rise to near-modern elevation (Isacks, 1988; Gubbels et al., 1993). In addition to crustal thickening, continental lithospheric delamination has been proposed as a

mechanism for the rapid Neogene surface uplift posited by the classic model (Kay and Kay, 1993; Garzione et al., 2008; DeCelles et al., 2009). Continental lithospheric foundering involves removal of negatively buoyant lower crust (i.e., eclogite root) and mantle lithosphere. Results from paleoelevation and geomorphic studies indeed support Late Miocene rapid surface uplift of the region (Ghosh et al., 2006; Hoke et al., 2007; Garzione et al., 2008). Pedogenic carbonate and carbonate cement samples collected between 17 and 18°S within the Altiplano and Eastern Cordillera Neogene stratigraphy contain decreasing $\delta^{18}O$ values in progressively younger units (Garzione et al., 2008). Garzione et al. (2008) interpreted this oxygen-isotope trend as evidence for an increase of 2.5$\pm$1 km of the elevation of the Eastern Cordillera during Late Miocene time. Although these results are in agreement with fossil leaf and clumped isotope data collected from the Altiplano and Eastern Cordillera (e.g., Gregory-Wodzicki, 1998; Ghosh et al., 2006), the elevation gain predicted by all three methods can be complicated (i.e., biased toward larger values) by climate change due to the uplift of the Andes (Ehlers and Poulsen, 2009). Evidence for Late Miocene rock uplift is also recorded by paleosurfaces that exist on both the eastern and western margins of the central Andes. Barke and Lamb (2006) estimated 1.7$\pm$0.7 km of localized rock uplift for the San Juan Del Oro surface of the Eastern Cordillera and Interandean tectonomorphic regions since 12-9 Ma when the surface was abandoned and incised. The Barke and Lamb (2006) results do not constrain the magnitude of surface uplift, however. The difference between rock and surface uplift is particularly significant because localized rock uplift can be much higher than mean

regional surface uplift due to isostatic effects. We will refer to this conceptual model for surface uplift as the rapid uplift end-member model.

A second end-member model for the topographic evolution of the central Andes invokes gradual surface uplift since the Late Eocene when deformation propagated from the Western Cordillera into the Eastern Cordillera. Evidence for pre-Neogene deformation comes from Eocene exhumation ages within the Eastern Cordillera and changes in paleocurrent directions within Paleogene stratigraphy of the Altiplano and Eastern Cordillera (Horton et al., 2002; McQuarrie et al., 2005; Ege et. al., 2007; Barnes et al., 2008). Although pre-Neogene shortening is considered low (<100-150 km) for building a high-elevation plateau, long-term shortening should have led to crustal thickening and isostatic rebound in the Eastern Cordillera. Therefore, unless erosion rates exceeded or were equal to rock uplift rates, the Eastern Cordillera should have been rising since the Late Eocene barring some mechanism for keeping the elevation of the Andes low during an extended period of deformation. The gradual uplift end-member model posits that the Andes gained the majority of its modern elevation prior to the Late Miocene (i.e. ~10 Ma).

The Tertiary stratigraphy of the Chaco foreland basin in Bolivia shows an increase in both grain size and depositional rates during the Late Miocene (Uba et al., 2006, Uba et al., 2007). This stratigraphic change might be the result of rapid surface uplift. However, previous studies have inferred that this depositional trend might instead be primarily controlled by distance from the approaching fold-and-thrust belt (DeCelles and Horton, 2003; Uba et al., 2006). Thus, the primary mechanism that caused these

changes in Late Miocene stratigraphy is still uncertain. In addition to thrust belt migration, the role of climate change and continental lithosphere foundering as controls on the foreland-basin stratigraphy of the central Andes has also been emphasized in recent years. For example, Kleinert and Strecker (2001) documented a change from previously dry to wetter conditions in the Santa Maria basin of northern Argentina between 9 and 7 Ma. Uba et al. (2007) found a significant (i.e. factor of 5) increase in time-averaged depositional rates within the stratigraphy of the Subandean thrust belt at approximately 8-7 Ma based on U-Pb dating of tuffs within Tertiary volcanic rocks. Coeval with changes in depositional rates and climate conditions within the foreland depositional facies of the Cenozoic fluvial units shift from single-thread sinuous channels to more amalgamated alluvial megafan facies (Uba et al., 2006). Uba et al. (2007) interpreted the change in depositional rates and facies as a consequence of a shift from semiarid to a more humid climate condition during the onset of the South American monsoon. An increase in mean annual precipitation should increase sediment supply through enhanced erosion rates and transport ability of foreland fluvial systems through higher mean annual discharge.

In addition to thrust belt migration, rapid surface uplift due to crustal thickening and climate change, lower crustal delamination is another mechanism that has been proposed for the central Andes to cause surface uplift in the mountain belt and, through flexural loading of the adjacent foreland basin, modify foreland-basin stratigraphy. The cordilleran cycle, a conceptual model for mountain-belt development and cyclicity proposed by DeCelles et al. (2009), posits that as lower crust and mantle lithosphere are

underthrust beneath a growing mountain-belt, magmatic and petrologic processes lead to the formation of a dense eclogitic root that acts as a subsurface negatively-bouyant load, lowering the elevation of the mountain belt relative to a state of isostatic equilibrium (DeCelles et al., 2009; Pelletier et al., 2010). If sufficient shortening takes place, the eclogite root reaches a critical thickness or volume and is delaminated or removed as a Rayleigh-Taylor instability. This cordilleran cycle, as posited by DeCelles et al. (2009), includes episodic periods of increased surface uplift and shortening rates, both of which should have a significant effect on the adjacent foreland basin through the modification of both rates of sediment supply and creation of accommodation-space. Presently, the Puna plateau is thought to be in a post-delamination state in this conceptual model (Schurr et al., 2006; DeCelles et al., 2009) and, as a consequence, has a mean elevation that is significantly higher than the Altiplano plateau. The Altiplano, in turn, is thought to have had a delamination event at 10 Ma (Kay et al., 1994). DeCelles et al. (2009) propose that the Altiplano may already be in an early stage of a new cycle and its lower elevation is a consequence of newly forming eclogite loads. Evidence for delamination beneath the Altiplano comes from seismic velocity analysis of the eastern Altiplano lithosphere at 20°S (Zandt and Beck, 2002). A low velocity zone occurs within the upper mantle beneath the thickened crust of the eastern Altiplano and western edge of the Eastern Cordillera and is interpreted as a location where the cold-fast upper mantle has been removed by a delamination event. As such, might stratigraphic trends in the Late Miocene Chaco foreland-basin deposits be a signature of lithospheric foundering?

Previous studies have numerically modeled the evolution of the central Andes as a coupled mountain-belt-foreland-basin system. Flemings and Jordan (1989) first simulated the rapid uplift end-member model for the last 5 Myr of deformation in the central Andes with a two-dimensional model. They concluded that the foreland basin adjacent to the central Andes should have shifted from narrow and underfilled to broad and overfilled as sediment supply outpaced sediment accommodation. However, the results of their model are potentially limited by the fact the mountain belt component of their model was simplified by assuming a constant topographic slope and sediment supply through time. Prezzi et al. (2009) recently applied a more rigorous deformation and erosion model to test the effect of mountain load geometry and elastic thickness of the South American lithosphere on the sediment accommodation rates within the foreland basin of the central Andes since the middle Miocene. They found that by decreasing the elastic thicknesses beneath the Eastern Cordillera and Interandean zones between 14-6 Ma and by deforming a detailed structural cross section developed by McQuarrie (2002), their model results adequately fit modern gravity anomalies and isopach distributions for the Late Cenozoic stratigraphy recently described by Uba et al. (2006) in the Subandean zone.

In this study we explore the linkages between thrust-belt kinematics, climate change, continental lithosphere delamination, and the foreland-basin stratigraphy in the central Andes using a coupled, two-dimensional numerical model. Flemings and Jordan (1989) simulated the foreland response to a fixed topographic slope and constant sediment supply, and thus, did not capture the effects of feedbacks among mountain-belt erosion, sediment supply to the foreland basin, and sediment accommodation within the

foreland basin. The Prezzi et al. (2009) study focused on the changes in foreland basin accommodation based on surface uplift due to a very specific history of crustal deformation and changes in elastic thickness under constant climate conditions. Both studies focused on crustal thickening as the dominant mechanism for driving foreland basin development. In contrast, in this paper, we aim to constrain the relationship of the Cenozoic foreland-basin stratigraphy to end-member surface uplift models, climate change and lower crustal delamination in order to place firmer constraints on the paleoelevation history of central Andes. First, we determine which end-member surface uplift model is most consistent with the available stratigraphic and tectonic data for the development of the eastern margin of the central Andes. Second, we determine whether there is some signal (e.g., unconformity, grain size change) of climate change or continental lithospheric delamination recorded in the upper Miocene Chaco foreland-basin stratigraphy.

2. Geologic Background

The central Andes of southern Bolivia contain a high-elevation, internally draining, low-relief plateau. This portion of the Andes also has the highest magnitude of total shortening (i.e., approximately 285 km of minimum crustal shortening within the Eastern Cordillera, Interandean and Subandean zones) (Isacks, 1988; McQuarrie, 2002; Oncken et al., 2006). The orogenic belt is generally broken up into tectonomorphic regions which include (from west to east): the Western Cordillera, Altiplano, Eastern Cordillera, Interandean, Subandean and Chaco Foreland Basin zones (Figure 1). The modern topographic divide between westward internal drainage into the Altiplano basin

and eastward drainage into the Chaco foreland basin resides within the Eastern Cordillera, a bivergent fold-and-thrust belt. Thrusts within the Eastern Cordillera detach in Ordovician-aged horizons and predominantly exhume Paleozoic through Mesozoic units (McQuarrie, 2002). Further east, the Interandean and Subandean zones are where deformation is currently active. These zones contain dominantly eastward-verging imbricate thrusts that generally exhume younger stratigraphic units compared to the Eastern Cordillera. The modern deformation front is located between 0.5 and 1 km a.m.s.l. Beyond the Subandean zone, the Chaco foreland basin extends an additional 250 to 600 km east into Bolivia, Paraguay and the Pantanal wetlands of Brazil until it onlaps Precambrian basement highs in eastern Bolivia and southwestern Brazil (Horton and DeCelles, 1997). An exception occurs between 19 and 20°S where the foredeep basin deposits pinch out onto the Alto de Izozog basement high over a distance that is less than 200 km from the deformation front (Uba et al., 2006).

The Chaco foreland-basin stratigraphy has been documented within the exposed thrust sheets of the Eastern Cordillera, Interandean and Subandean zones by DeCelles and Horton (2003), Echavarria et al. (2003), Horton (2005), and Uba et al. (2005). Isopach trends have also been developed for the buried modern foreland basin units based on correlations between well data and seismic cross sections (Uba et al., 2006). Starting at the base of the Cenozoic stratigraphy from the Subandean zone (Figure 2), the Petaca and Yecua Formations contain fluvial deposits with well developed paleosols, paleocurrent trends that dominantly show transport toward or along strike with the approaching mountain belt and thicknesses that are low considering the amount of time

contained within the units. The Yecua Formation is unique to the Subandean zone Cenozoic units because it also contains shallow marine facies in addition to fluvial and lacustrine facies in outcrops located north of 20°S. Moving up through the stratigraphy into the Tariquía, Guandacay and Emborozú Formations, overall grain size increases from that of the Yecua Formation, paleocurrent data indicate a shift to transport from the west, and depositional rates increase. Based on dating volcanic ash layers in the Cenozoic foreland-basin stratigraphy, there is a factor of five increase in depositional rates between the Yecua and Tariquía Formations (Uba et al., 2007). Higher in the stratigraphic section, depositional rates decrease by half upward into the Guandacay Formation. Although deposition is generally conformable within the Cenozoic stratigraphy, unconformities bound the Petaca Formation and an angular unconformity separates the Guandacay and Emborozú Formations. The upper unconformity of the Petaca Formation has been interpreted to record the uplift and passage of the forebulge as the Subandean zone passed from the backbulge into the foredeep basin (Uba et al., 2006). In contrast, the angular unconformity located between the Guandacay and Emborozú Formations has been interpreted as the initiation of wedge-top deposition in the Subandean zone. Low-angle unconformities have been documented at the base of coarsening upward cycles within the age equivalent stratigraphy of the Tariquía and Guandacay Formations in northern Argentina (Echavarria et al., 2003). However, cycles and significant unconformities were not documented in the Tariquía and Guandacay Formations of the southern Bolivia Subandean zone (Uba et al., 2006). Farther west and older in age, similar stratigraphic trends occur within the remnant foreland-basin stratigraphy of the Eastern Cordillera and

Interandean zones (Figure 2). The transition from the Cayara into the Camargo Formation involves an overall increase in grain size, and changes in paleocurrent direction and apparent depositional rates. One stratigraphic difference between this remnant foreland basin and the Neogene foreland basin of the Subandean zone is that an unconformity does not bound the lowest Cenozoic unit in the section. Overall, the most significant trends within the Cenozoic foreland-basin stratigraphy of the eastern margin of the central Andes are the apparent increase in depositional rates and grain size with decreasing age, and thus, any numerical models for the foreland basin evolution of the eastern margin of the central Andes must honor these trends.

3. Numerical Model Description

The numerical model of this paper is a 2D kinematic model that couples an actively deforming and eroding mountain belt with sediment transport and flexure within a depositional foreland basin. A 2D model is valid for this region of the Andes because the mountain front is nearly linear and paleoflow directions for the majority of the Cenozoic foreland-basin stratigraphy are perpendicular to the mountain front. The topography of the numerical model represents the mean topography of the eastern margin of the central Andes (i.e. western edge of the model begins in the Altiplano) located between 18-21°S. In our kinematic model, shortening and rock uplift rates are prescribed. Although time-averaged shortening rates can be directly calculated from published values, obtaining valid rock uplift rates is an iterative process of running simulations and checking the results against independent published data (e.g., modern topography and exhumation magnitudes). In this paper we report model outcomes that are consistent with

published data for the central Andes, including the modern topography, shortening rates from balance cross-sections, exhumation magnitudes, Cenozoic isopach data and modern basin geometries.

3.1. Deformation Model

Dynamic models for crustal deformation (e.g., Simpson, 2004) that directly solve for visco-plastic deformation within a fold-and-thrust belt could be applied to the central Andes. This approach, however, comes with the drawbacks of longer computational times and the difficulty of calibrating the model to multiple types of calibration data. We therefore take a simpler approach in this paper. In the model, the mountain belt is partitioned into individual blocks for each tectonomorphic region (i.e., Altiplano, Eastern Cordillera, etc.). Exceptions are made for the Eastern Cordillera and Subandean zones. The Eastern Cordillera, a bivergent fold-and-thrust belt, was divided into separate backthrust and forethrust blocks because these two regions rapidly exhume at different periods of time (Barnes et al., 2008). The Subandean zone was divided into a western and eastern block to allow the central and eastern Subandean zone to continue to subside until deformation propagated into the region during the Late Miocene. Deformation is simulated by uniform rock uplift and shortening applied to each actively deforming block. Time-averaged shortening rates were determined for input to the model by dividing the total shortening determined from field-based balanced cross sections for each tectonomorphic zone by the duration of fault activity (McQuarrie, 2005; Muller, 2002). The positions of the model nodes located to the east of the deformation front are fixed while the model nodes to the west of the deformation front are allowed to translate

toward the foreland basin as if riding over a décollement. The total propagation of the deformation front (and hence the forebulge) is approximately 536 km, which is close to the approximately 600 km of total propagation of the forebulge since the Late Eocene estimated by DeCelles and Horton (2003).

3.2. Erosion Model

A stream-power model is used to determine bedrock incision rates within the mountain belt (Howard and Kirby, 1983; Whipple and Tucker, 1999):

$$\frac{\partial h}{\partial t} = -k_e A^m \left|\frac{\partial h}{\partial x}\right|^n = -k_e A^{1/2} S = -k_e l S \qquad (1)$$

where h is elevation a.m.s.l. (m), t is time (yr), k_e is the bedrock erodibility (yr^{-1} for n = 1.0 and m = 0.5), A is the contributing drainage basin area (m^2), x is the lateral distance from the model origin (m), l is the distance along the principal channel from the headwaters of the drainage basin (m), S is the local channel slope (unitless) and m and n are constants that determine the dependence of local erosion on discharge and channel slope. Equation (1) determines the erosion rates of the major streams that act as the local base level for the mountain front topography. In equation (1) we assume that the length of the principal channel is proportional to the square root of the contributing drainage area (Hack, 1957). We also assume that the area and slope exponents m and n have values of 0.5 and 1 respectively. Evidence from theory and field studies predicts that the ratio of m/n is near 0.5 (Whipple and Tucker, 1999). Although the slope exponent n can range between 0.66 and 2.0 depending on the relationship between slope and stream power

(shear stress), we chose to make the stream power linearly proportional to the slope (n = 1.0 and m = 0.5), consistent with the assumption of many other studies (e.g., Kirby and Whipple, 2001; Snyder et al., 2000). Bedrock incision rates for active mountain belts are on the order of 0.1 to 1.0 mm/yr (Montgomery and Brandon, 2002). When m/n is equal to 1/2, we found that k_e must be on the order of 10^{-6} (m/yr) to appropriately reproduce the range of calculated exhumation rates (i.e., 0.1-0.6 mm/yr) for timescales of 10^2 to 10^7 years for the central Andes (Safran et al., 2005; Ege et. al., 2007; Barnes et. al. 2008). The boundary between the bedrock portion of the model (where stream-power-driven erosion of bedrock is modeled) and the alluvial portion of the model (where grains-size-dependent sediment transport is modeled) is allowed to fluctuate in the model. If a given model node contains sediment or sediment is deposited (i.e., upstream sediment supply exceeds the transport capacity), then the node is treated as an alluvial channel and no bedrock incision occurs. Otherwise, bedrock incision occurs and the amount of newly created sediment transported downstream is controlled by the transport capacity.

3.3. Sediment Transport Model

Sediment transport of a bimodal grain size distribution (i.e., gravel and sand) is simulated with a modified version of the diffusion model approach, which states that sediment flux is proportional to local channel slope. Linear slope-dependent sediment flux, when combined with conservation of mass, gives a diffusion equation for the evolution of the longitudinal profile of the foreland basin (Paola et al., 1992). In the model of this paper we added a threshold slope term to the diffusion equation model because transport of gravel requires a threshold slope to initiate transport. The equation

for alluvial deposition and erosion along a channel profile in our model is a combination of mass balance (i.e., the Exner equation) and the slope-dependent sediment-transport equation:

$$\begin{aligned} q_s &= k_g(S-\varphi), S > \varphi \\ q_s &= 0 \qquad\quad , S \le \varphi \end{aligned} \tag{2}$$

$$\frac{\partial h}{\partial t} = -\frac{\partial q_s}{\partial x} = \frac{q_{s,\text{upstream}} - q_{s,\text{downstream}}}{\partial x} \tag{3}$$

where k_g is the transport coefficient (m^2/yr), φ is the threshold slope which is a function of grain size and q_s is the local sediment flux (m^2/yr). The transport coefficients for gravel and sand are determined from a relationship that depends on discharge and river type (Paola et al., 1992). Paola et al. (1992) calculated the values for braided and meandering rivers to range between 1.0-7.0 x 10^4 (m^2/yr) for a drainage basin with a length of 100 kilometers and a mean annual precipitation of 1 m. We chose a value of 1.0 x 10^4 (m^2/yr) for the gravel transport coefficient, which is a reasonable value for braided, gravel-dominated streams with relatively small drainage areas. The transport coefficient for sand was chosen to be approximately 6.5 x 10^4 (m^2/yr), which is on the order of the transport coefficient used by Flemings and Jordan (1989) for their simulation of the central Andes. The threshold slope for gravel entrainment is approximately 0.001, which represents effective channel parameters of a median grain size of 0.02 m and bankfull flow depth of 1.85 m. The chosen median grain size is on order with the median grain size of bedload material observed within the modern Rio Pilcomayo located in the Eastern Subandean zone (Mugnier et al., 2006).

Channel armoring is an emergent property of the model obtained by incorporating a threshold slope for gravel transport. If discharge is insufficient to entrain gravel present on the channel bed during a time step, then the finer-grained sand deposited beneath the gravel is prevented from being transported during that time step. This process should reduce both alluvial and bedrock erosion in regions of lower regional slope where gravel is present. Active bed material layers in natural channels are on the order of 1-2 grains thick (Hassan et al., 2006). Although our active layer is on the order of a meter, it is valid to have a larger active layer for the purposes of this study because we are focusing on long-term (>10^5 yr) grain size trends that average over many individual flooding events.

3.4. Basin Flexure

The bedrock and alluvial surface dynamics models are coupled to a flexural foreland basin in order to quantitatively assess accommodation-space creation and the migration of the forebulge through time in the model. The flexural model solves for the displacement of a thin elastic beam subjected to a spatially-distributed vertical load (Turcotte and Schubert, 2002):

$$D\frac{\partial^4 w(x)}{\partial x^4} + (\rho_m - \rho_s)gw(x) = L(x) \qquad (4)$$

where w is the deflection of the Earth's crust (m), D is the flexural rigidity (Nm), ρ_m is the density of the mantle (kg/m^3), ρ_s is the density of the mountain crust or foreland sediment (kg/m^3), g is the acceleration due to gravity (m/s^2), and $L(x)$ is the topographic load (kg/ms^2). For each simulation, except for those involving eclogite root delamination

(discussed later), we solve for the deflection due to a topographic load every time step using a Fourier transform method (Watts, 2001). Viscous relaxation effects were not considered in the model because we interpret stratigraphic patterns over geologic timescales that are greater than relaxation timescales.

Several studies have calculated the flexural rigidity of the central Andes using 2-dimensional methods (Horton and DeCelles, 1997; Stewart and Watts, 1997; Tassara, 2005). Their results suggested that flexural rigidities along the eastern margin of the central Andes range between 1.5×10^{23} and 4.0×10^{24} Nm. We chose to use a flexural parameter of 150 km because this value best fits the observed modern basin geometry between 18-20°S. This value is consistent with the results of Chase et al. (2009), who found that the flexural parameter should be less than 220 km for the central Andes. The flexural parameter is defined as the following (Turcotte and Schubert, 2002):

$$\alpha = \left[\frac{4D}{(\rho_m - \rho_s)g} \right]^{1/4} \tag{5}$$

where α is the flexural parameter (km). Rearranging equation (5) and applying values from Table 1 yields a flexural rigidity of approximately 6.8×10^{23} Nm, which is well within the range of calculated effective flexural rigidities for the central Andes. Although previous studies have suggested that the elastic thickness varies in space and time (e.g., Toth et al., 1996; Prezzi et al., 2009), such variations are difficult to constrain. Therefore, our model implements a uniform and constant elastic thickness.

3.5. Numerical Modeling Methods

We ran three types of experiments using our numerical model: (1) an end-member surface-uplift model experiment, (2) an eclogite-root-foundering experiment, and (3) a climate-change experiment. The end-member surface-uplift model experiment simulates the last 43 Myr when deformation is concentrated in the eastern margin of the central Andes. The purpose of this experiment is to contrast the foreland basin response (e.g., changes in depositional rates and grain size) to a mountain belt that is gradually uplifting through time against the foreland-basin response to rapid surface uplift caused by Neogene crustal thickening. The parameters used in this experiment are found in Table 1. During the simulations of this experiment, climatic conditions were held constant and time steps are approximately 700 yr. Topographic profiles were sampled at 22, 10 and 0 Ma for visual comparison.

Following the end-member surface-uplift model experiment, we ran an eclogite-root-foundering experiment. The purpose of this experiment is to contrast the foreland-basin response to rapid surface uplift in the mountain belt caused by crustal thickening alone against rapid surface uplift caused by a combination of foundering and crustal thickening. The model duration, time steps and interval of topographic profile sampling in the foundering experiment are the same as in the end-member surface-uplift experiment. We also apply the parameters in Table 1 and the same kinematic histories in the mountain belt (e.g., shortening rates and propagation of deformation) as in the rapid uplift model. An eclogite root grows in our model between 25 and 10 Ma beneath the Altiplano and Eastern Cordillera backthrust zones where significant crustal thickening has taken place such that lower crustal rocks are subjected to pressures sufficient enough

to produce eclogite. We assume that eclogite foundering is caused by a Rayleigh-Taylor instability (defined as the diapiric drip of a dense layer overlying a less dense layer) and that the timescales over which the growth of the eclogite drip occurs can be calculated to within first order by the results of the linear-stability analysis of Turcotte and Schubert (2002):

$$\tau_a = \frac{13.04\mu}{(\rho_e - \rho_m)b} \tag{6}$$

where τ_a is the amount of time required for an instability to grow by a factor of e, μ is the viscosity of the upper and lower layers and b is the original thickness of the eclogite layer. The Rayleigh-Taylor instability is not modeled explicitly but instead we prescribe a rate of eclogite root growth consistent with the observed spacing between foundering events in the central Andes and the thickness of the root required to initiate foundering. Equation (6) is rearranged to solve for b in order to prescribe the thickness of the eclogite root required to initiate foundering in our model. Based on geophysical models and paleoelevation proxies, the length of time over which the foundering event occurred beneath the Altiplano was approximately 3 Myr (i.e. between 10 and 7 Ma) (Molnar and Garzione, 2007; Garzione et al., 2008). We assume that the majority of the foundering time is spent growing the instability in the lower crust-mantle interface by the initial factor of e due to the high resistance to flow of the mantle when minimal perturbations in the lower crust-mantle interface exist. Later, when a significant pressure gradient exists at the base of the eclogite layer due to the formation of a drip; the pinching and foundering portion of the drip event occurs much more rapidly. Based on this argument we inferred

that τ_a is approximately less than or equal to 3 Myr. Using densities of 3300 and 3600 kg/m^3 for upper mantle and eclogite and a root growth period of 3 Myr, the range in maximum eclogite layer thickness is calculated to be between 1.87 to 46.88 km as the effective viscosity of the underlying mantle layer varies between 4.0 x 10^{19} and 1.0 x 10^{21} Pa s. This range in eclogite layer thickness is consistent with the 10 to 20 km eclogite root thickness that occurred prior to removal during a numerical simulation of mantle drip for the Puna plateau (Quinteros et al., 2008). We used a similar scale (i.e. 12.5 km) for the thickness of the eclogite root required to initiate delamination.

Between 10 and 7 Ma, the root is removed at a linear rate until it is completely removed at 7 Ma. During the period of root foundering, we allowed our flexure algorithm to specify the magnitude of rock uplift due to foundering and superimposed that result on the results of the rapid-uplift model. Our model is kinematic, so the viscous coupling between the sinking root and the overlying lithosphere is not simulated in our model. However, there is a possibility that viscous coupling may result in significant (i.e., on the order of 100s meters) subsidence and rebound (Gogus and Pysklywec, 2008).

An experiment with climate change during the late Miocene was also conducted in order to determine its impact on the foreland-basin stratigraphy. At 9 Ma, we simulated the onset of the South American monsoon by increasing both the bedrock erodibility and sediment transport coefficients in response to increased mean annual discharge and storm intensity. The bedrock erodibility (k_e) of the stream power model and the transport coefficients (k_s and k_g) of the diffusion model are both theoretically shown to be proportional to discharge (Paola et al., 1992; Whipple and Tucker, 1999). If we assume

that discharge scales proportionally with precipitation, then erosion rates and sediment transport rates scale proportionally with precipitation. This is reasonable assumption for erosion rates because long-term erosion rates have been shown to correlate with mean annual precipitation rates in the Andes (Kober et al., 2007). Sediment transport rates in alluvial rivers have been proposed to correlate with mean annual precipitation (Molnar et al., 2006). Although the magnitude of increase in mean annual precipitation at the onset of the South American monsoon unknown, long term erosion rates since the Eocene have not varied by more than a factor of two from modern rates (Safran et al., 2005; Ege et. al., 2007; Barnes et. al. 2008). Thus, both erosion rates and sediment transport rates increase by a factor of two at 10 Ma. The model duration, time steps and interval of topographic profile sampling are the same as in the end-member uplift models.

4. Numerical Modeling Results

4.1. End-member surface-uplift model experiment summary

Topographic-profile and sediment-flux time-series plots show the development of the eastern margin of the central Andes in response to the gradual uplift end-member model (Figures 3A and 3B). Between 43 and 22 Ma, deformation is concentrated within the Eastern Cordillera. During this period of time, topographic slopes are low, and thus the sediment fluxes from the mountain belt into the Altiplano and foreland basin are also low. Sediment eroded off of the Eastern Cordillera is not transported beyond the foredeep, which is underfilled to completely filled. The sediment flux leaving the backbulge basin toward the east is zero at this time. The Subandean zone in its pre-deformed state is located more than 400 km from the deformation front near the

forebulge crest (Figure 3A). Low sediment flux from the mountain belt is consistent with observed paleocurrent data from the Petaca Formation, located in the Subandean zone, showing westward paleotransport from the South American craton. Between 30 and 22 Ma there is a period of higher than average sediment flux (Figure 3b). Sediments with low erodibility contained within wedgetop basins are exhumed as the eastern portion of the Eastern Cordillera begins to uplift at 30 Ma. Exhumation of the wedgetop basin deposits causes the period of high sediment delivery to the foredeep.

By 22 Ma, rock uplift rates between 0.1 and 0.2 mm/yr cause the Eastern Cordillera to rise to a peak elevation of 3 km a.m.s.l. The increase in topographic relief causes the mean sediment flux from the mountain belt into the foreland basin to increase such that sediment from the mountain belt outpaces foreland accommodation rates and is transported out of the foredeep. Subsidence rates in the backbulge basin are an order of magnitude lower than in the foredeep. Consequently, the backbulge basin is rapidly filled and sediment from the mountain belt begins to bypass the filled backbulge basin by 27 Ma (Figure 3B). At this time the deformation front propagates east into the Interandean zone and creates a step in topography located 500 km from the left end of the model domain in Figure 3A. Again, there is a period of higher-than-average sediment flux between 22 and 15 Ma caused by exhumation of wedgetop basins within the Interandean zone. The 22 Ma snapshot represents the time period when the Camargo Formation is transitioning into the overlying Mondragon Formation of the Eastern Cordillera and when the Petaca Formation is being deposited in the Subandean zone.

By 10 Ma, the core of the Eastern Cordillera is within 1 km of its modern peak elevation and the deformation front and forebulge migrate another 100 km toward the South American craton (Figure 3A). As a result of the increase in relief and mountain front slopes, the average sediment flux into the foredeep increased from 20 to 30 m^2/yr and overfills the foredeep. A plot of sediment flux leaving the backbulge basin shows that at least half of the mean sediment supply to the foreland is leaving the backbulge basin at this time (Figure 3B). A significant decrease in the amount of sediment leaving the backbulge basin and a significant increase in the amount of sediment entering the foredeep occurs between 5 and 2 Ma. This is the period in time when the eastern Subandean zone is actively uplifting. High rock uplift rates in the eastern Subandean zone lead to exhumation of wedgetop basins and the development of a topographic step. Although sediment flux from the mountain belt is high during this time, rapid creation of topographic relief in the front of the thrust belt causes high subsidence rates in the foredeep. A significant portion of the sediment supply to the foreland basin is deposited and stored in the foredeep. The final topography at 0 Ma fits the average and maximum topography of the modern central Andes well. However, the alluvial slopes of the depositional foreland basin are a few hundred meters higher than the average channel elevations today. It is unclear if this error is due to an over prediction of the sediment supply, an under prediction of transport coefficient, or if sediment fluxes at the downstream end of the model domain are too low.

Although rates of shortening and the propagation of the deformation front are identical for both the gradual and rapid uplift models, the surface uplift and sediment flux

response to the rapid uplift model is notably different (Figure 4A and 4B). Between 43 and 22 Ma, low rock uplift rates (i.e., 0.1-0.2 mm/yr) in the Eastern Cordillera lead to only 1.7 km of peak surface uplift over this period of time. As such, mean sediment supply rates from the mountain belt remain low (i.e., <10 m^2/yr) over the first 21 Myr of simulation. Despite the fact that the mean sediment flux into the foreland is half the rate of the gradual uplift model, the foredeep and backbulge basins in the rapid uplift model are able to fill and bypass sediment from the mountain belt by 25 Ma. Following an additional 12 Myr of active uplift between 22 and 10 Ma, peak elevation of the Eastern Cordillera in the rapid uplift model rises to 2.3 km a.m.s.l. and deformation propagates east into the western Subandean zone. Mean sediment flux into the foreland basin and sediment fluxes leaving the backbulge basin in the rapid uplift model remain low compared to the values for the gradual uplift model at this time. At 10 Ma, rock uplift rates across the mountain belt increase from 0.1 to 0.3-0.5 mm/yr as the central Andes rapidly uplift in response to deformation in the Subandean zone. As a result, mean sediment flux from the mountain belt increases from 20 to 60 m^2/yr. However, the sediment flux leaving the backbulge basin decreases shortly after the initiation of rapid uplift across the mountain belt because subsidence rates in the foredeep quickly respond to surface uplift within the mountain belt, trapping sediment within the foredeep near the edge of the mountain belt. The final topography in the rapid uplift model at 0 Ma equally reproduces the modern mean and maximum topographies of the central Andes mountain belt and foreland basin. Again, the predicted foreland topography is slightly higher than that of the observed.

4.2. Constrains on foreland basin depositional rates

In both the gradual and rapid uplift models, surface uplift of the eastern margin of the central Andes leads to an increase in sediment supply and subsidence within the foreland basin. Figures 5A and 5B show the sediment thickness curves for four depozones (i.e., the forethrust region of the Eastern Cordillera, western Interandean zone, western Subandean zone and eastern Subandean zone, respectively) within the foreland basin for both the gradual and rapid uplift models. The solid lines represent the results for the simulations described in the previous section. Between 43 and 22 Ma deformation and surface uplift is limited to the Eastern Cordillera. At this time, both the eastern region of the Eastern Cordillera and western Interandean zones are located within the foredeep basin of the gradual uplift model (Figure 5A). Between 40 and 30 Ma the deformation front remains in the core of the Eastern Cordillera. A spatially-fixed load leads to constant subsidence rates, and thus, constant depositional rates in the Eastern Cordillera depozones over this period of time. The Interandean depozone, however, is located in the distal foredeep, and therefore develops an acceleration in depositional rates between 31 and 25 Ma that is characteristic of an increase in subsidence rates due to an approaching mountain belt. Further to the east, the western and eastern Subandean depozones are located within the backbulge basin. Low subsidence rates lead to low depositional rates between 43 and 36 Ma. Between 36 and 25 Ma, the forebulge crest migrates through the western Subandean depozone and leads to erosion and development of an unconformity. Sediment deposited while the eastern Subandean depozone was located in the backbulge is completely eroded away during this time period. The shaded region between 36 and 25

Ma represents the approximate depositional age for the Camargo Formation. Predicted depositional thicknesses for the Camargo Formation range between 1 and 2 km in the Eastern Cordillera and Interandean depozones, but under predict the > 2 km thickness of the Camargo Formation observed in the Camargo syncline (DeCelles and Horton, 2003). By 22 Ma, deformation propagates into the Interandean zone. Therefore, the Interandean depozone is uplifted and exhumed at this time. Between 22 and 10 Ma, depositional rates within the western Subandean zone accelerate as it reaches the foredeep. At 9 Ma, a sharp inflection point occurs that reflects a significant increase in depositional rates in the eastern Subandean zone. These high depositional rates are inferred to be the result of high rock uplift rates in the western Subandean zone. Gradual uplift model simulations were also conducted for constant and lower rock uplift rates for the western Subandean zone. However, a slow and gradual kinematic model for the deformation front could not reproduce the extreme increase in isopach thickness for the Tariquía Formation given the constraints on deformation propagation rates during the Late Miocene. Reproducing accurate accommodation magnitudes for the foreland-basin stratigraphy while also fitting the modern topography motivated applying an increase in rock uplift rates at the front of the mountain belt to the gradual uplift model. Rock uplift rates within the backthrust and forethrust of the Eastern Cordillera, however, remained gradual and constant. Increased uplift rates between 9 and 4 Ma caused an increase in sediment accommodation rates. As a result, a larger portion of the incoming sediment flux is stored in the foredeep depozone. Extremely high depositional rates continue until approximately 4 Ma when the

basin begins to uplift and exhume. This period of time represents the deposition of the Guandacay Formation and the transition into the Emborozú Formation.

Although shortening rates and thrust belt propagation rates in the rapid uplift model are the same as in the gradual uplift model, the total thicknesses of basins for the rapid uplift model are significantly different than those for the gradual uplift model (Figure 5B). Early in the model experiment between 43 and 22 Ma, lower rock uplift rates within the Eastern Cordillera cause depositional thicknesses within the eastern forethrust region of the Eastern Cordillera and Interandean zones to be 500 m less compared to thicknesses predicted in the gradual uplift model. Both locations develop Camargo Formation thicknesses of approximately 500 m, which is much less than the observed > 1 km thickness for the Camargo Formation in the Camargo syncline. By 12 Ma, low rock uplift rates in the Eastern Cordillera and Interandean zones lead to a factor-of-2 decrease in the total sediment thickness of the western Subandean depozone compared to the thickness predicted for this depozone in the gradual uplift model. At 9 Ma, the entire mountain belt between the western Subandean zone and Altiplano rapidly uplifts. This rapid uplift causes an order of magnitude increase in depositional rates within the eastern Subandean depozone. Approximately 2 km of sediment are deposited between 8-6 Ma. However, this is still 1 to 1.8 km less than the maximum isopach values reported by Uba et al. (2006) for the Tariquía Formation.

Additional simulations were conducted for both surface-uplift models to test the sensitivity of the sediment thickness curves to the rigidity of the South American plate. The dotted lines represent the results for simulations with the lowest rigidity calculated

for the South American plate (i.e., $1.5x10^{23}$ Nm). Decreasing the rigidity in the gradual uplift model simulation does not significantly affect the depositional thicknesses within the Eastern Cordillera (Figure 5A). However, the maximum thicknesses of the other three depozones decrease by approximately 300-500 m. Conversely, increasing the rigidity of the South American plate (dashed lines) to the upper limit of rigidities previously calculated for the South American plate (i.e., $4.0x10^{24}$ Nm) causes the maximum depositional thickness of three western most depozones to increase with respect to the initial results. Changing the rigidities of the South American plate in the rapid uplift model has similar effects as in the gradual uplift model (Figure 5B). Although the rigidity of the South American plate can range over an order of magnitude, the predicted thickness of the Camargo Formation within Eastern Cordillera and Interandean depozones of the rapid uplift model is less than a kilometer.

4.3. The role of eclogite-root-foundering on surface uplift and foreland development

The eclogite-root-foundering simulation involves the growth and removal of a subsurface load that modifies the flexural response of the foreland basin and rock uplift distribution within the mountain belt. Prior to 10 Ma, rock-uplift rates and shortening rates are prescribed to be identical to the rapid-uplift model for the region of the mountain belt that is deforming. Between 25 and 10 Ma, an eclogite load is allowed to uniformly grow beneath the Altiplano and backthrust region of the Eastern Cordillera where the deformed crust is sufficiently thick for lower crustal rocks to undergo a phase transition to eclogite (Figure 6A). The subsurface eclogite load, whose location is represented by the black bar, sets up a flexural profile (identified by the thick black line)

that superimposes onto the flexural profile caused by the topographic load. Although the total deflection due to the presence of the eclogitic root is small (i.e. ~1m) at 25 Ma, by 10 Ma the total deflection is on the order of 1 km at the center the eclogite root. At 25 Ma, the edge of the eclogite load is located approximately 150 km from the current deformation front. As a result of the distance between the load and deformation front, subsidence caused by the eclogite load is small in the foredeep and shortly to the east subsidence changes to rock uplift in the distal foredeep. As time progresses, the Interandean and Subandean depozones are subject to an additional component of rock uplift because they are located on the flexural forebulge related to the eclogite root load. Following 10 Ma, the polarity of lithospheric deflection reverses as the eclogite root is removed (Figure 6B). The solid black curve is the total amount of deflection that occurs over 3 Myr as the subsurface load is removed. A significant amount of rock uplift occurs directly over the center of the load in the eastern Altiplano and western backthrust region of the Eastern Cordillera and rapidly decays into the core of the Eastern Cordillera. Further east, the Interandean and western Subandean zones experience subsidence on the order of meters to tens of meters. Beyond the western Subandean zone, the deflection due the eclogite foundering is less than a meter. Rock uplift rates in the Altiplano and the core of the Eastern Cordillera due to the eclogite root foundering range between $3.0\text{-}6.0\text{x}10^{-4}$ m/yr. Maximum deflection rates in the eastern Interandean and western Subandean zones are on the order of 10^{-7} and 10^{-5} m/yr. Rock uplift rates near the mountain front and within the foreland basin (i.e., Interandean and Subandean zones) prescribed in the rapid uplift model at 10 Ma are on the order of $6.0\text{-}5.0\text{x}10^{-4}$ m/yr, and therefore, the flexural

signal from a delamination is small when compared to the subsidence or rock uplift due to crustal thickening. Conversely, rock uplift rates due to the delamination are slightly greater in the Altiplano and the backthrust region of the Eastern Cordillera than the prescribed uplift rates due to crustal thickening.

Sediment supply into the foredeep predicted by the eclogite-root-foundering model shows a similar behavior to that of the rapid-uplift model. Sediment supply rates are low until approximately 10 Ma when the eclogite drip event accompanied by the rapid uplift of the eastern Interandean and western Subandean zones lead to increased channel slopes in the front of the mountain belt (Figure 7A). The amount of sediment bypassing the foreland basin in the eclogite-root-foundering model is also similar to the rates predicted by the rapid uplift model with the exception of a greater magnitude of sediment flux between 15 and 5 Ma. This increase in sediment leaving the foreland per time is either the result of increased erosion rates in the mountain belt or decreased sediment accommodation rates in the foreland basin. A comparison of sediment thicknesses predicted by the rapid uplift and eclogite-root-foundering models through time for the Interandean, western Subandean and eastern Subandean zones shows that the drip event modified sediment accommodation by less than 10 percent of the maximum basin thicknesses before foundering (Figure 7B). The western Interandean zone basin deposits are approximately 100 meters thicker at 22 Ma for the eclogite-root-foundering model (solid line) compared to the rapid uplift model (dashed line). Between 25 and 22 Ma the western Interandean zone is located close enough to the edge of the eclogite load to experience subsidence which causes the change in sediment thickness between models.

Conversely, the Subandean basins are located far enough from the eclogite load at that time to undergo rock uplift. The western Subandean basin is the least affected basin by the drip event because of its proximity to the inflection point between subsidence and rock uplift caused by accumulation of eclogite. The eastern Subandean zone also experiences rock uplift due to foundering, and thus, lesser sediment thicknesses between 20 and 10 Ma. Decreased accommodation in the Subandean zones leads to an increase in sediment leaving the basin prior to 10 Ma. Following 10 Ma, the drip event leads to minor subsidence in the eastern Subandean zone and the sediment thickness differences between the two models becomes negligible.

4.4. The role of climate change in foreland basin development

The results for the climate change experiment that involves a factor-of-two increase in mean annual precipitation during the Late Miocene due to the onset of the South American monsoon are reported here. Bedrock uplift rates during the Late Miocene within the actively deforming mountain belt in this simulation are increased with respect to those of the rapid-uplift model to maintain similar surface uplift histories, and thus, the basin accommodation histories between the rapid uplift model and the climate change model are the same. We only report observations for sediment flux and grain size. Although erosion rates and sediment transport rates are a factor of two lower for the first 35 Myr, the first order behavior of sediment flux entering the basin appears to be unchanged from that of the rapid uplift model (Figure 8). The effect of lowering both erosion and sediment transport coefficients by a factor of two early on in the simulation is a few million years delay in the time when sediments begin to exit the backbulge basin.

Decreasing both erosion rates and sediment transport rates also has a cumulative effect of decreasing sediment bypass rates (solid black line) by almost half the value of sediment bypass predicted by the rapid uplift model (dashed line). Following 9 Ma, the sediment bypass rates suddenly increase by a factor of 1.5 times the previous flux.

An abrupt change in erosion rates and transport efficiency due to climate change should be expected to have an effect on grain size within the depositional basin, and therefore, we tracked the gravel-sand interface for each of the experiments (Figure 9). A comparison of the gradual uplift, rapid uplift and climate change model results (Figure 9) reveals that in general the gravel-sand boundary closely tracks the location of the deformation front (shown as the dashed line). An exception to this observation occurs immediately following times when the deformation front propagates basinward and the gravel-sand interface lags behind the deformation front for approximately 1-2 Myr until the regional slope of the newly formed wedgetop basin increases above the threshold slope for gravel transport. Once gravel reaches the deformation front, gravel progradation into the foredeep appears to be limited within a narrow zone of approximately 50 km from the deformation front. Figure 9A compares the gravel-sand boundaries for the gradual and rapid uplift models. Prior to 10 Ma, the mean location of the gravel-sand boundaries for both models generally remain in front of the deformation front following the 2 Myr lag periods. However, the initiation of rapid uplift in the Interandean and western Subandean zones at approximately 10 Ma causes the gravel-sand boundary to retrograde back into the wedgetop zone as accommodation rates exceed sediment supply rates. Both models appear to closely overlap each other with two exceptions. Between 22

and 15 Ma, the gravel front in the gradual uplift model progrades more rapidly than the gravel front of the rapid uplift model due to a combination of greater uplift rates in the Interandean zone wedgetop basin and greater sediment supply rates. Between 8 and 5 Ma, the mean location of the gravel-sand interface of the rapid uplift model retrogrades more than the gravel-sand interface of the gradual uplift model due to greater subsidence rates. Figure 9B compares the results for the climate-change model to the rapid-uplift model, and thus, should highlight the effects of changes in precipitation on grain size. Although both the bedrock erodibilities and transport coefficients are a factor of two less in the climate change model compared to the rapid-uplift model between 25 and 9 Ma, the gravel-sand boundaries generally track each other well through time. However, there are a few brief periods of time when the gravel-sand interface of the climate change model lags behind that of the rapid uplift mode. When the bedrock erodibilities and transport coefficients increase by a factor of root 2, the results of the climate change model do not vary significantly from the trends of the rapid-uplift model.

5. Discussion

Two end-member surface-uplift models have been proposed for the central Andes (Garzione et al., 2008). One model involves a long history of constant deformation since the Late Eocene, accompanied by a gradual increase in mean surface elevation prior to 10 Ma. The opposing end-member model suggests that the central Andes did not gain significant elevation until after 10 Ma. Our results show that if the elastic properties of the underthrusted South American plate remain effectively constant, then rapid rock uplift is likely to have occurred within the Interandean and western Subandean zones

during the late Miocene in order to generate sufficient accommodation space for the Tariquía Formation observed in outcrops within the central to eastern Subandean zone (Figure 5). Constraints on the initiation of rapid rock uplift in the Interandean and Subandean zones is based on the isopach data for the Yecua and Petaca Formations. If rock uplift rates were greater in the Interandean and Subandean zones prior to 9-8 Ma when the Tariquía Formation began to be deposited, then the isopach trends for the Yecua and Petaca Formations observed within the central Subandean zone would show maximum thicknesses greater than 825 meters. Rock uplift rates prescribed for the Interandean and western Subandean zones in the gradual uplift model lead to maximum thicknesses for the Petaca-Yecua deposits that are on the order of 1 km. Although other studies have proposed that decreasing the flexural rigidity of the South American lithosphere can explain an increase in accommodation for the Tariquía Formation (Prezzi et al., 2009), we show that a constant flexural rigidity model can also fit the Late Miocene isopachs well.

At 10 Ma, both the Altiplano and Eastern Cordillera are sufficiently far from the central and eastern Subandean zones such that their contribution to the accommodation space is low compared to that of the Interandean and western Subandean zones. The deflection of an elastic beam in response to a point load decreases exponentially with distance from the center of the load. As such, a comparison of the sediment thickness time series results for the gradual and rapid uplift models shows little change in accommodation rates following 10 Ma in the eastern Subandean zone even though the peak elevations of the Eastern Cordillera differ by 2 kilometers (Figure 5). Although the

difference in peak elevation within the Eastern Cordillera does not strongly affect Late Miocene foreland-basin sediment accommodation, we can constrain the early surface uplift history of the Eastern Cordillera and Altiplano with the middle Tertiary stratigraphy of the Eastern Cordillera and western Interandean zones because these depozones were located at least 100 km closer to the Eastern Cordillera than the central Subandean zone. DeCelles and Horton (2003) measured a thickness of over 2 km for the Camargo Formation within the Camargo Syncline of the Eastern Cordillera. A comparison of sediment thicknesses deposited between 36 and 22 Ma predicted by the gradual and rapid uplift models shows that a sediment accommodation thickness of 2 km within the early foreland basin is not achievable unless rock uplift rates in the core of the Eastern Cordillera more closely resembled the rock uplift rates specified within the gradual uplift model (Figure 5). Although there is uncertainty in the depositional age of the Camargo Formation, the rapid uplift model could not create sufficient sediment accommodation space if deposition began as early as 40 Ma. If the erosion rates in our model are close to the effective erosion rates during the Early Miocene and Late Oligocene, then the thick deposits of the Camargo Formation would imply that the peak elevation of the Eastern Cordillera was between 2-3 km by 22 Ma.

An Eastern Cordillera peak elevation of 2-3 km might have acted as an effective topographic barrier to moisture that was being transported west across the central Andes. Today, the topography of the eastern flank of the central Andean Plateau prevents a significant amount of moisture that originated from the Atlantic Ocean and Amazon Basin from being transported west into the Altiplano and Western Cordillera by the South

American Summer Monsoon (Strecker et al., 2007). A similar behavior occurs in the southern Andes where the moisture from the Pacific Ocean carried by the Southern Hemisphere Westerlies rains out on the west coast of South America and the Patagonian Andes leading to semiarid conditions on the eastern flank of the Andes. The southern Andes are an effective moisture barrier even though their mean elevation is around 2 km lower than the central Andes with peak elevations ranging from 2-3 km between 38 and 50°S. We envision the topography of the central Andes during the early to middle Miocene as being similar to the southern Andes today, which suggests that the orogen may have been an effective barrier to moisture being transported to the southwest from the Atlantic. If this is the case, then basins within the Altiplano and Western Cordillera regions of the central Andes should become increasingly arid around or soon after 22 Ma. Based on abrupt changes in lacustrine facies within basins, the onset of hyper-aridity has been documented to occur between 10 and 6 Ma for basins within the Western Cordillera between 18 and 22°S (Gaupp et al., 1999; Saez et al., 1999). However, based on oxygen isotopes, soil morphological characteristics and salt chemistry, Rech et al. (2006) and Rech et al. (2010) proposed that the onset of hyperaridity could have occurred in the Atacama Desert earlier, between 19 and 13 Ma. In northern Argentina between 25 and 26°S, recent thermochronologic data from the Puna plateau show that the Eastern Cordillera was deformed and exhumed at the same time as the Eastern Cordillera further to the north in southern Bolivia (Carappa et al., 2011). Interestingly, Vandervoort et al. (1995) also documented an earlier shift from nonevaporitic to evaporitic sedimentary deposits within Puna plateau basins located between 24-26°S at approximately 15 Ma. A

middle Miocene onset of aridity-hyperaridity within the Andean plateau (perhaps as far south as the Puna) and basins on the western margin of the central Andes would be consistent with the peak elevations within the Eastern Cordillera that were necessary to generate sufficient accommodation space for the Caramargo Formation.

Another output of our numerical model during the end-member uplift model experiment was a time series for sediment leaving the foreland basin (Figures 3 and 4). Changes in the sediment bypass rates would not be directly recorded in the foreland-basin stratigraphy, and therefore, one must look at the stratigraphy of adjacent intracratonic basins or the continental shelf to directly sample this signal. Presently, a topographic divide exists in southern Bolivia that splits the flow of major rivers draining off the central Andes north into the Amazon and southeast into the Rio del La Plata Cratonic Basins. Based on the sediment bypass time series for each of the simulations the sediment flux component from the central Andes should steadily increase from the Late Oligocene into the Quaternary with a local minimum between 8-3 Ma. Analysis of drill core sediments from the Amazon Fan and Ceara Rise show that Andean derived sediments reached the continental margin between 16.5 and 11.3 Ma (Dobson et al., 2001; Figueiredo et al., 2009). Between 9 and 6.8 Ma sedimentation rates increased for both the Amazon Fan and Ceara Rise. This increase in sedimentation rates was interpreted as the establishment of a transcontinental Amazon drainage system that fully linked the Andean forelands to the Amazon Fan. Sedimentation rates continued to increase into the Pliocene-Pleistocene during the period of most rapid uplift within the northern Andes (Hoorn et al., 1995). The overall increase in sedimentation rates on the Atlantic shelf is

predicted by our model. The higher the mean elevation of the mountain belt, the greater the sediment supply may exceed available accommodation space. Our model also predicts a factor of two increase in sediment flux leaving the foreland basin during the Late Pliocene to Pleistocene as foredeep accommodation rates decrease in response to slower rock uplift rates in the Interandean and Subandean zones. One aspect of our model results that is not recorded in the Amazon Fan is a Late Miocene to Early Pliocene decrease in sediment supply rate. The absence of a drop in sedimentation rates may be expected because a small portion of the Amazon Basin drains the central Andes, and therefore, sediment supply to the Amazon Fan is more predominantly influenced by the northern Andes. A stratigraphic data set that would be more predominately influenced by the central Andes would be the deposits of deepwater fans offshore of the Rio del la Plata estuary which samples the Andes between 18 and 34°S. To our knowledge no analysis has been conducted for the Late Tertiary sediments of the Rio del la Plata fans.

A hypothetical eclogite foundering event in the eastern Altiplano region during the Middle Miocene to Pliocene time was synchronous with increased grain size and depositional rate in the foreland-basin stratigraphy. Our results show that the distance from the center of mass of the load is the most important parameter for determining how the growth and removal of a lower crustal load affected rock uplift and subsidence within the mountain belt and foreland basin (Figure 6). An inflection point between subsidence and uplift occurs at a distance of $(\pi/2)\alpha$ (i.e., approximately 235 km for this study) from the growing eclogite root load. During the Oligocene to Early Miocene, the foredeep depozone was located closer to the eclogite root than it would be for the remainder of the

simulation (i.e., less than $(\pi/2)\alpha$ km). As a result, the accumulation of eclogite drove an additional 100 meters of subsidence, which is more than a factor of 2 greater than subsidence added to the western and eastern Subandean depositional basins during the Late Miocene. The greatest deflection occurred directly above the center of the eclogite root, which was located in the eastern Altiplano and westernmost Eastern Cordillera. This deflection led to approximately 0.5 to 1 km of rock uplift in the Altiplano. Therefore, an addition 2 km of surface uplift due to crustal thickening and sediment deposition is required to achieve the modern mean elevation of the Altiplano if it was located at 1 km around 10 Ma. Similar amounts of rock uplift due to crustal thickening (i.e., 1-2 km) are required in the Eastern Cordillera to reach its modern mean and spatially-averaged maximum elevations. However, less rock uplift due to crustal thickening is necessary if the average thickness of the eclogite root was significantly larger than the value applied in this study. We infer that this is less likely because a thicker eclogite root would grow a significantly sized instability in less than a period of 3 Myr, which is the proposed length for the delamination period. Our results also show that less than 0.5 km of rock uplift is contributed to the eastern edge of the Eastern Cordillera and western Interandean zones by eclogite removal. Barke and Lamb (2006) calculated that the San Juan del Oro paleosurface that overlies the eastern part of the Eastern Cordillera was uniformally uplifted by approximately 1 km. Therefore, the eclogite root must be located closer or beneath to the forethrust of the Eastern Cordillera to uniformly uplift it by 1 km. However, tomography data suggests that foundering is more likely beneath the Altiplano

and western part of the Eastern Cordillera (Beck and Zandt, 2002). Thus, part of the 1 km of rock uplift of the San Juan del Oro surface is likely the result of crustal thickening.

Climate change was the final process that we tested for the foreland basin of the central Andes of southern Bolivia. Erosion rates and transport coefficients between 43 and 9 Ma were a factor of 2 less than the values between 9 and 0 Ma. As a direct result peak sediment flux into the foreland basin and sediment bypass rates were significantly less than the values resulting from the rapid uplift model (Figure 8). At the onset of the South American monsoon, both sediment bypass rates and sediment flux rates into the foredeep increased significantly. The increase in sediment supply to the foredeep is predominantly controlled by the rapid uplift of the mountain belt instead of by the increase in mean annual precipitation. Increasing erosion rates and decreasing transport rates should lead to steeper slopes in the proximal foreland basin. Both sediment supply and transport capability increased as mean annual precipitation increased, which lead to minimal change in the regional slopes as these effects cancel each other. Regardless, regional slopes in the model appear to be predominately affected by rapid subsidence due to crustal thickening near the deformation front instead of by increasing precipitation. Another way to gauge the effect of climate change is to track the boundary between gravel and sand deposition. Paola et al. (1992) demonstrated that sinusoidal variation in both sediment supply and transport coefficients lead to migration of the gravel-sand interface especially if the forcing period is small compared to the basin equilibrium time. Our results show that the first order migration of the gravel-sand boundary appears to be unaffected by the factor of 2 increase in both of these parameters over the timescales that

we are sampling (Figure 9). Based on our results the threshold slope term appears to be a more primary control on gravel progradation than the transport coefficient term. Rock uplift in the hinterland leads to steeper slopes that are capable of transporting gravel. As a result, gravel trapped near the mountain front can rapidly prograde toward the new deformation front when it is located in a wedge top basin. Eventually, rock uplift leads to the exhumation of pre-Tertiary units near the deformation front that can produce gravel during bedrock incision. Conversely, regional slope within the foreland is insufficient to transport gravels far into the foredeep. Therefore, a combination of processes causes progradation of the gravel-sand interface during forward propagation of the deformation front; climate change appears to have played a secondary role in controlling gravel progradation for the central Andes.

6. Conclusions

Based on our modeling results, we propose that the early surface uplift history (i.e., prior to 22 Ma) of the eastern margin of the central Andes more closely resembled the gradual uplift model. When the rigidity of the South American plate ranged between $1.5x10^{23}$ and $4.0x10^{24}$ Nm, surface uplift of the core of the Eastern Cordillera in the rapid uplift model produced grossly under-matched sediment accommodation during the deposition of the >2km thick Camargo Formation. The gradual uplift model more closely fits the observed sediment thicknesses for the Camargo Formation located in the Eastern Cordillera, and thus, the core of the Eastern Cordillera experienced rock uplift rates that would have lead to significant topography (i.e., peak elevations near 2-3 km) by the early Miocene if basin-averaged erosion rates were on the order of 10^{-4} m/yr. Further crustal

thickening during the middle Miocene may have increased mean topography of the Eastern Cordillera to the point where it became an effective barrier to easterly moisture derived from the Atlantic; in turn, this initiated aridity in the Western Cordillera and Atacama Desert regions at that time. During the Late Miocene, the Interandean and western Subandean zones likely underwent rapid rock and surface uplift to produce the amount of accommodation required to store the thick Tariquía Formation which was deposited within a period of 2 million years.

Our results also support the hypothesis that the first-order trends in the Tertiary Subandean zone foreland-basin stratigraphy are predominantly influenced by its distance from the approaching mountain belt. An increase in topographic loads located less then $(3/4)\pi\alpha$ km from the a depozone can cause deflections up to the order of a km. Beyond this distance deflection ranges up to 100s of meters near the forebulge. During the Late Miocene the eclogite root was located more than a distance of $(3/4)\pi\alpha$ from the Subandean depozone. As such, the accommodation rates within the central-eastern Subandean zone foredeep were positive, but only on the order of 10s meters. Therefore, the deflection caused by an approaching mountain belt exceeded the deflection caused by eclogite delamination. Also based on our results, the factor-of-five increase in depositional rates was not likely the result of an increase in erosion rates and sediment transport rates caused by climate change. Increased erosion rates would lead to isostatic rebound of the mountain front, and thus decreased sediment accommodation within the foredeep, if crustal thickening does not increase as well. If crustal thickening does increase with erosion rates as in our model, then the additional sediment supplied

bypasses the foreland basin because it is already overfilled. In addition to accommodation rates, the location of the deformation front in time appears to exert a primary control on the gravel-sand interface. Increasing erosion rates and sediment transport rates by a factor of 2 due to the onset of the South American Monsoon at 9 Ma did not generate a long-term progradation in the gravel-sand interface. Instead, the gravel front retreated toward the deformation front due to the rapid subsidence rates within the foredeep basin. Actively uplifting fold-and-thrust belts are able to achieve channel slopes that are above the threshold for gravel entrainment and produce gravel by bedrock incision. As a direct result, the gravel-sand interface rapidly progrades when the deformation front propagates into the foreland basin.

Acknowledgements

Our research was supported in part by ExxonMobil funding. We thank Peter DeCelles and Joellen Russell for their helpful comments.

References

Barke, R. and Lamb, S., 2006. Late Cenozoic uplift of the Eastern Cordillera, Bolivian Andes, Earth and Planetary Science Letters, 249, 350-367.

Barnes, J.B., Ehlers, T.A., McQuarrie, N., O'Sullivan, P.B., Tawackoli, S., 2008. Thermochronometer record of the central Andean Plateau growth, Bolivia (19.5^{o}S). Tectonics 27, TC3003, doi:10.1029/2007TC002174.

Beck, S.L. and Zandt, G., 2002. The nature of orogenic crust in the central Andes. Journal of Geophysical Research, 107, doi:10.1029/2000JB000124.

Chase, C.G., Sussman, A.J., Coblentz, D.D., 2009. Curved Andes: Geoid, forebulge and flexure. Lithosphere, 1, 358-363.

DeCelles, P.G. and Giles, K.A., 1996. Foreland basin systems. Basin Research, 8, 105-123.

DeCelles, P.G. and Horton, B.K., 2003. Early to middle Tertiary foreland basin development and the history of Andean crustal shortening in Bolivia. Geol. Soc. Amer. Bulletin 115, 58-77.

DeCelles, P.G., Ducea, M.N., Kapp, P., Zandt, 2009. Cyclicity in Cordillera orogenic systems. Nature Geosciences, 2, 251-257.

DeCelles, P.G., Gehrels, G.E., Quade, J., Ojha, T.P., Kapp, P.A., Upreti, B.N., 1998. Neogene foreland basin deposits, erosional unroofing and the kinematic history of the Himalayan fold-thrust belt, western Nepal. Geological Society of America Bulletin 110, 2-12.

Dobson, D.M., Dickens, G.R., Rea, D.K., 2001. Terrigenous sediment on Ceara Rise: a Cenozoic record of South American orogeny and erosion. Palaeogeography, Palaeoclimatology, Palaeoecology 165, 215-229.

Echavarria, L., Hernandez, R., Allmendinger, R., and J. Reynolds, 2003. Subandean thrust and fold belt of northwestern Argentina: Geometry and timing of the Andean evolution. Association of American Petroleum Geologists Bulletin, 87, 965-985.

Ege, H., Sobel, E.R., Scheuber, E., Jacobshagen, V., 2007. Exhumation history of the southern Altiplano plateau (southern Bolivia) constrained by apatite fission track thermochronolgy. Tectonics 26, TC1004, doi:10.1029/2005TC001869.

Ehlers, T.A., Poulsen, C.J., 2009. Influence of Andean uplift on climate and paleoaltimetry estimates. Earth and Planetary Science Letters, 281, 238-248.

Flemings, P.B. and Jordan, T.E., 1989. A synthetic stratigraphic model for foreland basin development. Journal of Geophysical Research, 94, 3851-3866.

Figueiredo, J., Hoorn, C., van der Ven, P., Soares, E., 2009. Late Miocene onset of the Amazon River and the Amazon deep-sea fan: Evidence from the Foz do Amazonas Basin. Geology 37, 619-622.

Ford, M., Lickorish, W.H., Kusznir, N.J., 1999. Tertiary foreland sedimentation in the Southern Subalpine chains, SE France: a geodynamic appraisal. Basin Research, 11, 315-336.

Garcia-Castellanos, D., Fernandez, M., Torne, M., 2002. Modeling the evolution of the Guadalquivir foreland basin (southern Spain). Tectonics 21, ,doi:10.1029/2001TC001339.

Garzione, C.N., Hoke, G.D., Libarkin, J.C., Withers, S., MacFadden, B., Eiler, J., Ghosh, P., Mulch, A., 2008. Rise of the Andes. Science 320, 1304-1307.

Gaupp, Reinhard, Kott, Anne, Worner, Gerhard, 1999. Palaeoclimatic implications of Mio-Pliocene sedimentation in the high altitude intra-arc Lauca Basin of northern Chile. Palaeogeography Palaeoclimatology Palaeoecology 151, 79-100.

Ghosh, P., Garzione, C.N., Eiler, J., 2006. Rapid uplift of the Altiplano revealed through ^{13}C-^{18}O bonds in paleosol carbonates. Science, 311, 511-512.

Gogus, O.H., Pysklywec, R.N., 2008. Near-surface diagnostics of dripping or delaminating lithosphere. Journal of Geophysical Research, 113, B11404, doi:10.1029/2007JB005123.

Gregory-Wodzicki, K.M., Velasquez, K., MacIntosh, W.C., 1998. Climatic and tectonic implications of the Late Miocene Jakokkota flora, Bolivian Altiplano, Journal of South American Earth Sciences, 11, 533-560.

Gubbels, T.L., Isacks, B.L., Farrar, E., 1993. High-level surfaces, plateau uplift, and foreland development, Bolivian central Andes. Geology 21, 695-698.

Hack, J.T., 1957. Studies of longitudinal stream profiles in Virginia and Maryland. U.S. Geological Survey Professional Paper, 294-B, 45-97.

Hassan, M.A., Egozi, R., Parker, G., 2006. Experiments on the effect of hydrograph characteristics on vertical grain sorting in gravel bed rivers. Water Resources Research, 42, W09408, doi:10.1029/2005WR004707.

Heller, P., Angevine, C.L., Winslow, N.S., Paola, C., 1988. Two phase stratigraphic model of foreland-basin sequences. Geology 16, 501-504.

Hoke, G.D., Isacks, B.L., Jordan, T.E., Blanco, N., Tomlinson, A.J., Ramezani, J., 2007. Geomorphic evidence for post-10 Ma uplift of the western flank of the central Andes 18^{o}30'-22^{o}S. Tectonics 26, TC5021, doi:10.1029/2006TC002082.

Horton, B.K., DeCelles, P.G., 1997.The modern foreland basin system adjacent to the Central Andes. Geology 25, 895-898.

Horton, B.K., Hampton, B.A., LaReau, B.N., Baldellon, E., 2002. Tertiary provenance history of the northern and central Altiplano (Central Andes Bolivia): A detrital record of plateau-margin tectonics. Journal of Sedimentary Research, 72, 711-726.

Horton, B.K., 2005. Revised deformation history of the central Andes: Interferences from Cenozoic foredeep and intermontane basins of the Eastern Cordillera, Bolivia. Tectonics 24, TC3011, doi:10.1029/2003TC001619.

Howard, A.D, Kerby, G., 1983. Channel changes in badlands. Geological Society of America Bulletin, 94, 739-752.

Isacks, B.L., 1988.Uplift of the Central Andean Plateau and bending of the Bolivian orocline. Journal of Geophysical Research 93, 3211-3231.

Kay, R.W., and Kay, S.M., 1993. Delamination and delamination magmatism. Tectonophysics, 219, 177-189.

Kay, S.M, Coira, B., Viramonte, J., 1994. Young mafic back-arc volcanic rocks as indicators of continental lithospheric delamination beneath the Argentine Puna plateau, central Andes. Journal of Geophysical Research, 99, 24323-24339.

Kirby, E., and Whipple, K., 2001, Quantifying differential rock-uplift rates via stream profile analysis: Geology, v. 29, p. 415-418.

Kleinert, K. and Strecker, M.R., 2001. Climate change in response to orographic barrier uplift: Paleosol and stable isotope evidence from the Late Neogene Santa Maria basin, northwestern Argentina, Geological Society of America Bulletin, 113, 728-742.

Marzo, M. and Steel, R.J., 2000. Unusual features of sediment supply-dominated, transgressive-regressive sequences: Paleogene clastic wedges, SE Pyrenean foreland basin, Spain. Sedimentary Geology 138, 3-15.

McQuarrie, N., 2002. The kinematic history of the central Andean fold-thrust belt, Bolivia: Implications for building a high plateau. Geol. Soc. Amer. Bulletin 114, 950-963.

McQuarrie, N., Horton, B.K., Zandt, G., Beck, S., DeCelles, P.G., 2005. Lithospheric evolution of the Andean fold-thrust belt, Bolivia, and the origin of the central Andean pleateau. Tectonophysics 399, 15-37.

Molnar. P., Anderson, R., Kier, G., Rose, J., 2006. Relationships among probability distributions of stream discharges in floods, climate, bed load transport, and river incision. J. Geophys. Res., 111, F02001, doi:10.1029/2005JF000310.

Molnar, P., and Garzione, C.N., 2007. Bounds on the viscosity coefficient of continental lithosphere from removal of mantle lithosphere beneath the Altiplano and Eastern Cordillera. Tectonics 26, TC2013, doi:10.1029/2006TC001964.

Montgomery, D., Blanco, G., Willett, S.D., 2001. Climate, tectonics and the morphology of the Andes. Geology 29, 579-582.

Montgomery, D., Brandon, M., 2002. Topographic controls on erosion rates in tectonically active mountain ranges. Earth Planet. Sci. Lett. 201, 481-489.

Mugnier, J.L., Becel, D., and Granjeon, D., Active tectonics of the Subandean belt, in Willett, S., Hovius, N., Brandon, M., Fisher, D., eds., Tectonics, Climate and Landscape Evolution: Geological Society of America Special Paper, 398, 352-369, doi:10.1130/2006.2398(04).

Muller, J.P., Kley, J., Jacobshagen, V., 2002. Structure and Cenozoic kinematics of the Eastern Cordillera, southern Bolivia (21^{o}S). Tectonics 21, 10.1029/2001TC001340.

Oncken, O., Hindle, D., Kley, J., Elger, K., Victor, P., Schemmann, K., 2006. Deformation of the Central Andean Upper Plate System – Facts, Fiction, and Constraints for Plateau Models, in: Oncken, O., Chong, G., Franz, G., Giese, P., Gotze, H.J., Ramos, V., Strecker, M.R., Wigger, P. (Eds.), The Andes: Active Subduction Orogeny, Springer Berlin Heidelberg, Berlin, pp. 3-27.

Paola, C., Heller, P.L., Andgevine, C.L., 1992. The large-scale dynamics of the grain-size variation in the alluvial basins, 1: Theory. Basin Res. 4, 73-90.

Pelletier, J.D., 2007. Erosion rate determination from foreland basin geometry. Geology, 35, 5-8.

Pelletier, J.D., DeCelles, P.D., Zandt, G., 2010. Relationships among climate, erosion, topography and delamination in the Andes, A numerical modeling investigation. Geology, 38, 259-262.

Prezzi, C.B., Uba, C.E., Gotze, H., 2009. Flexural isostasy in the Bolivian Andes: Chaco foreland basin development. Tectonophysics, 474, 526-543.

Quinteros, J., Ramos, V.A., Jacovkis, P.M., 2008. Constraints on delamination from numerical models. 7th International Symposium on Andean Geodynamics (ISAG 2008, Nice), Extended Abstracts: 417-420.

Rech, J.A., Currie, B.S., Michalski, G., Cowan, A.M., 2006. Neogene climate change and uplift in the Atacama Desert, Chile. Geology 34, 761-764.

Rech, J.A., Currie, B.S., Shullenberger, E.D., Dunagan, S.P., Jordan, T.E., Blanco, N., Tomlinson, A.J., Rowe, H.D., Houston, J., 2010. Evidence for the development of the Andean rain shadow from a Neogene isotopic record in the Atacama Desert, Chile. Earth and Planetary Science Letters 292, 371-382.

Saez, A., Cabrera, L., Jensen, A., Chong, G., 1999. Late Neogene lacustine record and palaeogeography in the Quillagua-Llamara basin, Central Andean fore-arc (northern Chile). Palaeogeography Palaeoclimatology Palaeoecology 151, 5-37.

Safran, E.B., Bierman, P.R., Aalto, R., Dunne, T., Whipple, K.X., Caffee, M., 2005. Erosion rates driven by channel network incision in the Bolivian Andes. Earth Surface Processes and Landforms, 30, 1007-1024.

Schurr, B., Rietbrock, A., Asch, G., Kind, R., Oncken, O., 2006. Evidence for lithospheric detachment in the central Andes from local earthquake tomography. Tectonophysics, 415, 203-223.

Sempere, T., Butler, R.F., Richards, D.R., Marshall, L.G., Sharp, W., Swisher, C.C., 1997. Stratigraphy and chronology of Late Cretaceous-early Paleocene strata in Bolivia and northwestern Argentina. Geological Society of America Bulletin 109, 709-727.

Simpson, G., 2004. A dynamic model to investigate coupling between erosion, deposition and three-dimensional (thin-plate) deformation. Journal of Geophysical Research, 109, doi:10.1029/2003JF000078.

Snyder, N.P., Whipple, K.X., Tucker, G.E., and Merritts, D.J., 2000. Landscape response to tectonic forcing: Digital elevation model analysis of stream profiles in the Mendocino triple junction region, northern California: Geological Society of America Bulletin, v. 112, p. 1250-1263.

Snyder, N.P., Whipple, K.X., Tucker, G.E., Merritts, D.J., 2003. Importance of stochastic distribution of floods and erosion thresholds in the bedrock river incision problem. Journal of Geophysical Research, 108, doi:10.1029/2001JB001655.

Stewart, J. and Watts, A.B., 1997. Gravity anomalies and spatial variations of flexural rigidity at mountain ranges. Journal of Geophysical Research, 102, 5327-5352.

Strecker, M.R., Alonso, R.N., Bookhagen, B., Carrapa, B., Hilley, G.E., Sobel, E.R., Trauth, M.H., 2007. Tectonics and Climate of Southern Central Andes. Annual Review of the Earth and Planetary Sciences 37, 747-787.

Tassara, A., 2005. Interaction between the Nazca and South American plates and formation of the Altiplano-Puna plateau: Review of a flexural analysis along the Andean margin (15^{0}-34°S). Tectonophysics, 399, 39-57.

Toth, J., Kusznir, N., Flint, S., 1996. A flexural isostatic model of lithosphere shortening and forland basin formation: application to the Eastern Cordillera and Subandean Belt of NW Argentina. Tectonics 15, 213-223.

Turcotte, D.I., Schubert, G., 2002. Geodynamics. Cambridge University Press, Cambridge.

Uba, C.E., Heubeck, C., Hulka, C., 2005. Facies analysis and basin architecture of the Neogene Subandean synorogenic wedge, southern Bolivia. Sedimentary Geology 180, 91-123.

Uba, C.E., Heubeck, C., Hulka, C., 2006. Evolution of the late Cenozoic Chaco foreland basin, Southern Bolivia. Basin Research 18, 145-170.

Uba, C.E., Strecker, M.R., Schmitt, A.K., 2007. Increased sediment accumulation rates and climatic forcing in the central Andes during the Late Miocene. Geol. Soc. Amer. Bull. 35, 979-982.

Vandervoort, D.S., Jordan, T.E., Zeitler, P.K., Alonso, R.N., 1995. Chronology of internal drainage development and uplift, southern Puna plateau, Argentine central Andes.

Watts, A.B., 2001. Isostacy and Flexure of the Lithosphere, Cambridge University Press, Cambridge.

Whipple, K. and Tucker, G., 1999. Dynamics of the stream-power river incision model: Implications for height limits of mountain ranges, landscape response timescales, and research needs. J. Geophys. Res. 104, 17661-17674.

Tables and Figures:

Table 1: Parameters used in end-member model simulations

k_e (m/yr)	1.0×10^{-6}
k_q (m^2/yr)	1.0×10^{4}
k_s (m^2/yr)	6.5×10^{4}
φ	0.001
α (km)	150
ρ_s (kg/m^3)	2750
ρ_m (kg/m^3)	3300
ρ_e (kg/m^3)	3600
g (m/s^2)	9.8

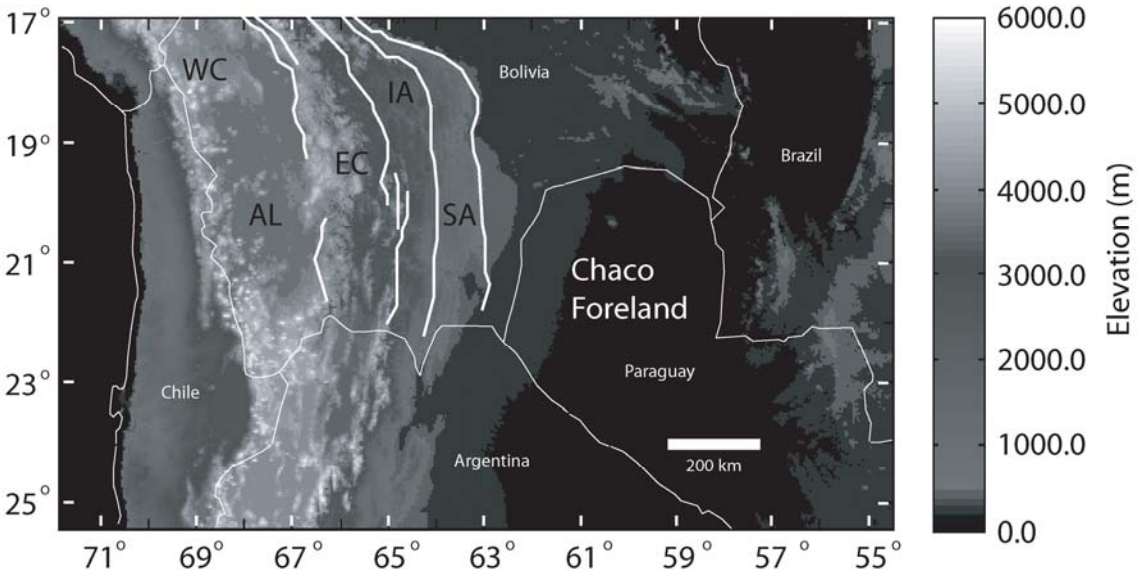

Figure 1: Digital Elevation model for the central Andes displaying the tectonomorphic regions after Barnes et al. (2008). Topography is from the SRTM 90 m data set. The tectonomorphic regions are the following: WC, Western Cordillera; AL, Altiplano; EC, Eastern Cordillera; IA, Interandean zone; SA, Subandean zone. The thick white lines are thrust faults located on the boundary between major divisions and the thin white lines mark political boundaries.

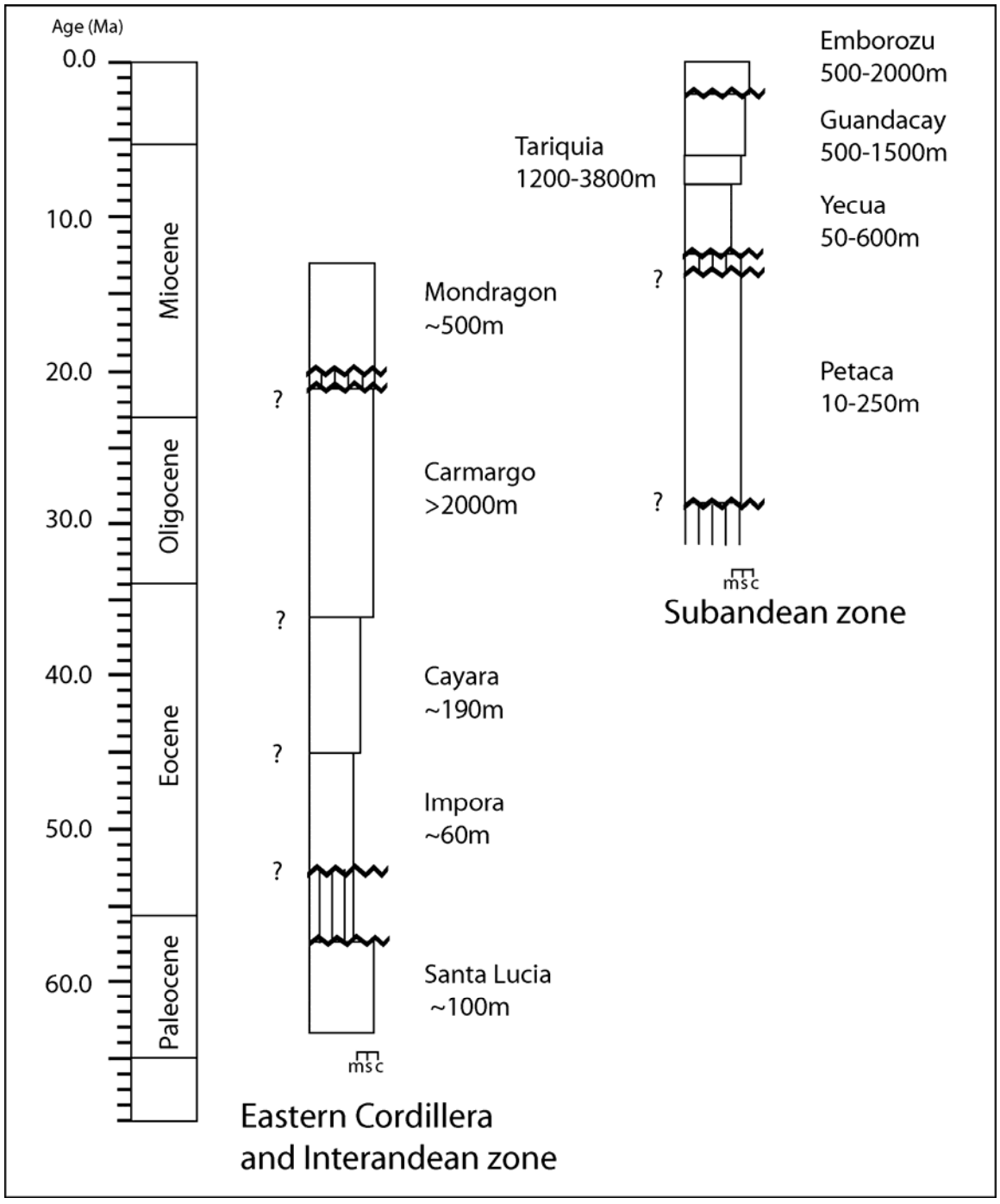

Figure 2: Generalized stratigraphic columns for the Cenozoic stratigraphy of the Chaco foreland basin after DeCelles and Horton (2003), Uba et al. (2006) and Uba et al. (2007). Formation thicknesses are displayed beneath the formation names. The questions marks

represent uncertainty in the boundaries between formations due to a lack of absolute age data. A detailed discussion of the age uncertainties for the Cenozoic stratigraphy of the Eastern Cordillera, Interandean and Subandean zones can be found in DeCelles and Horton (2003) and Uba et al. (2006).

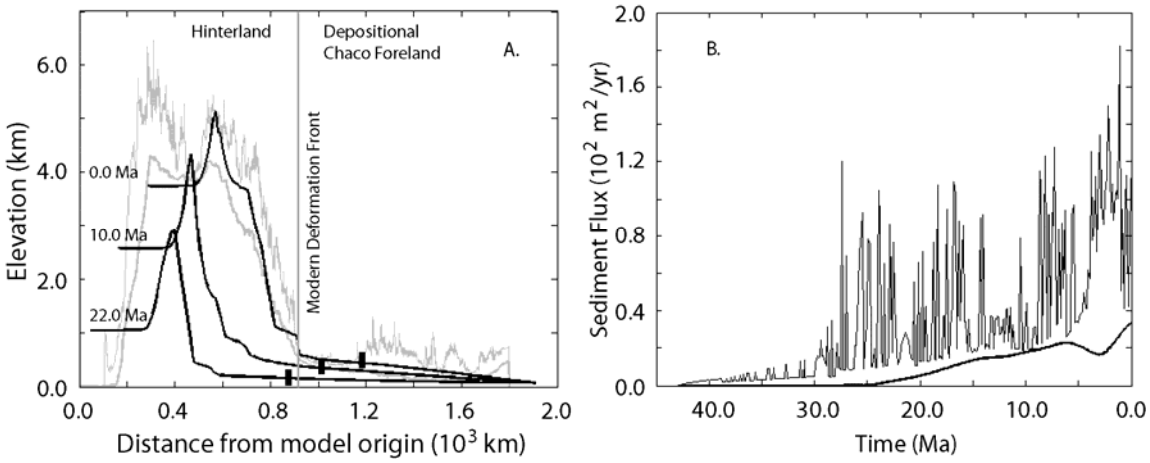

Figure 3: (A) Topographic evolution of the central Andes and (B) time series of sediment supply rates into and out of the foreland basin for the gradual uplift model. The thick black lines in Figure (A) represent snapshots of topography throughout the simulation and the thick gray lines represent the maximum and mean topography for a north-south sweep of topography between 18-21°S. The black rectangles represent the location of the forebulge crest during each snapshot in time with the oldest forebulge location on the left. In Figure (B), the thick line represents the sediment flux leaving the backbulge basin or right edge of the model and the thin lines represent the sediment flux at the deformation front into the foredeep of the foreland basin.

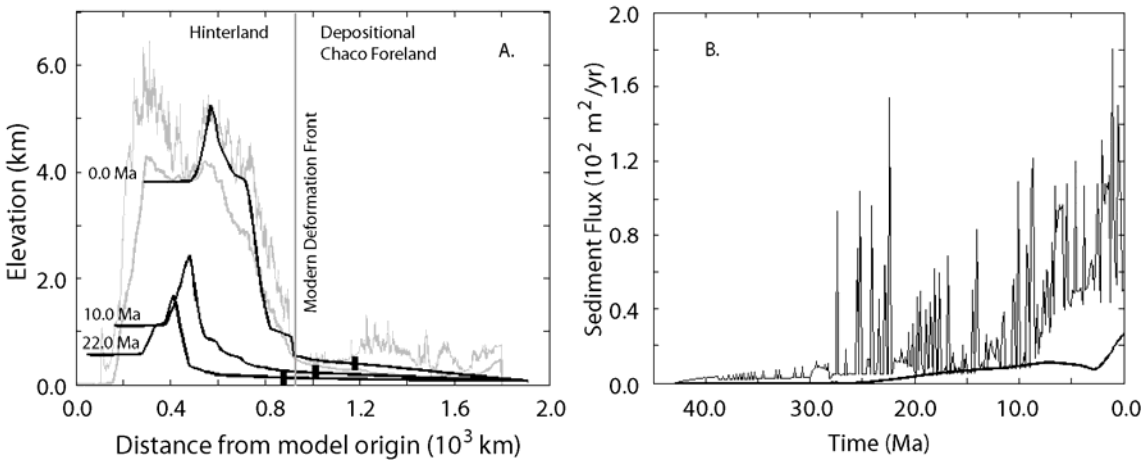

Figure 4: (A) Topographic evolution of the central Andes and (B) time series of sediment supply rates into and out of the foreland basin for the rapid uplift model. The thick black lines in figure (A) represent snapshots of topography throughout the simulation and the thick gray lines represent the maximum and mean topography for a north-south sweep of topography between 18-21°S. The black boxes represent the location of the forebulge crest during each snapshot in time with the oldest forebulge location on the left. In figure (B), the thick line represents the sediment flux leaving the backbulge basin or right edge of the model and the thin lines represent the sediment flux at the deformation front into the foredeep of the foreland basin.

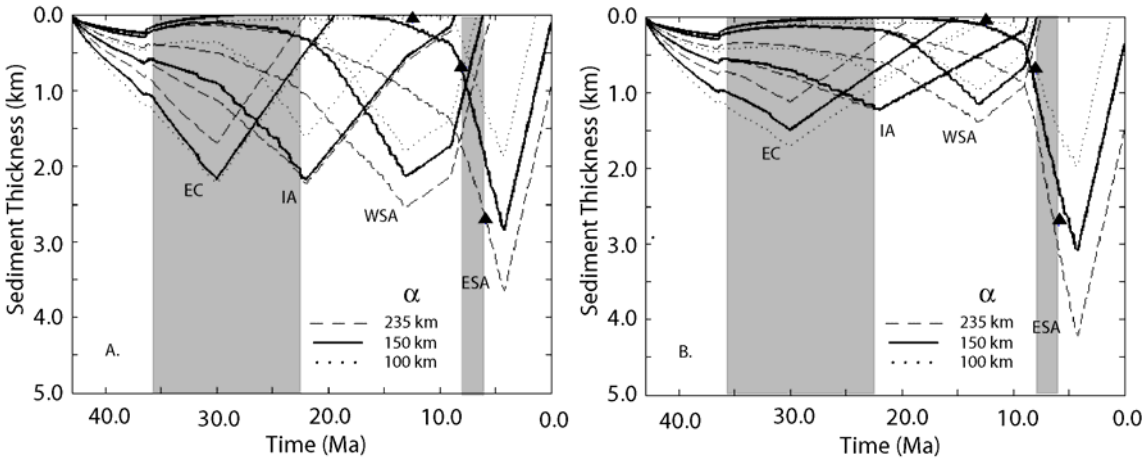

Figure 5: Uncompacted Tertiary sediment thickness for depozones located in the eastern Subandean zone (ESA), western Subandean zone (WSA), western Interandean zone (IA) and within the Eastern Cordillera forethrust region (EC) for the (A) gradual uplift and (B) rapid uplift models. The dotted, solid and dashed lines represent simulations with flexural parameters of 100, 150 and 235 km. Shaded regions represent the times when the Tariquía Formation of the Subandean zone and Camargo Formation of the Eastern Cordillera and Interandean zone were deposited. The subsidence curve from Uba et al. (2006) for the location in the Subandes that we sampled is represented by black triangles in both plots.

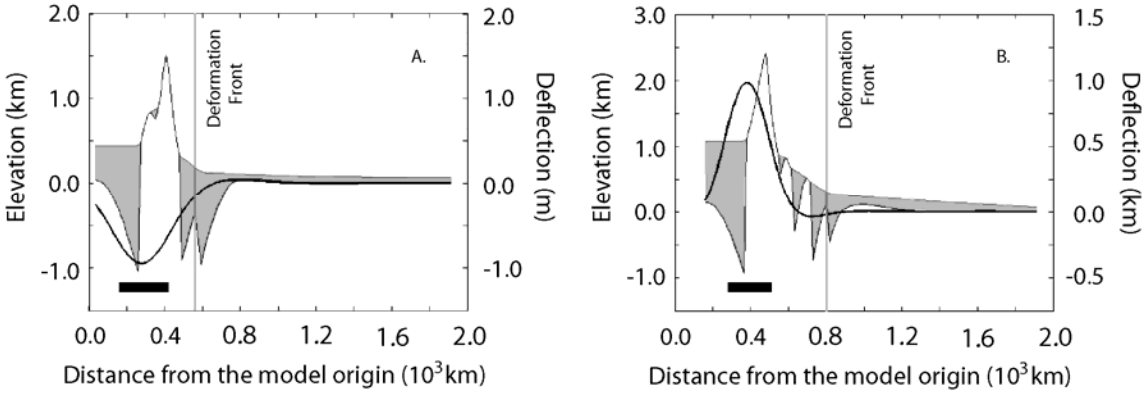

Figure 6: Topographic and flexural profile snapshots for the eclogite delamination model at (A) 25 and (B) 10 Ma. The shaded gray regions represent Tertiary sedimentary deposits and the pre-Tertiary bedrock is white. Lithospheric deflection caused by accumulation and delamination of an eclogite load is represented by a thick black line, whose scale is show on the right vertical axis, and the position of the eclogite load is represented by the black horizontal bars.

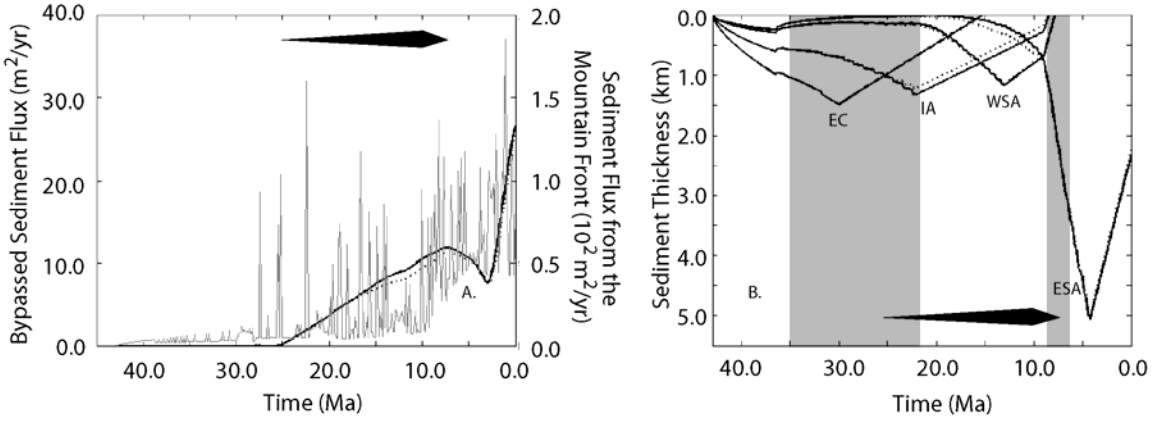

Figure 7: (A) Time series data for sediment fluxes into and out of the foreland basin and (B) uncompacted sediment thickness for depozones located in the eastern Subandean (EA), western Subandean (WSA), Interandean (IA) and Eastern Cordillera (EC) tectonomorphic zones for the eclogite delamination model. The black symbol at the top of figure A and the bottom of figure B represents the growth and delamination of the eclogite root between 25 and 10 Ma. In figures A and B the thick lines represent the eclogite delamination model and the thin dashed lines represent the rapid uplift model.

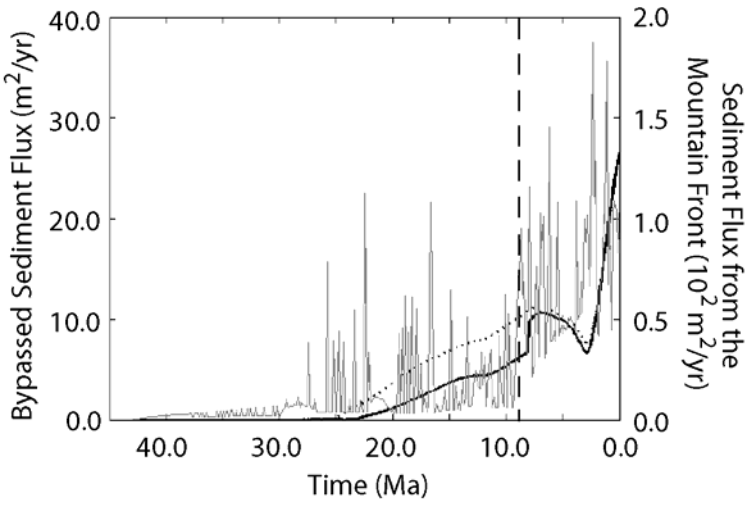

Figure 8: Sediment flux time series data for the climate change model. The thick line represents the sediment flux leaving the backbulge basin during the climate change model and the dashed lines represent the sediment flux leaving the backbulge basin during the rapid uplift model. The dashed vertical line represents the onset of the South American monsoon.

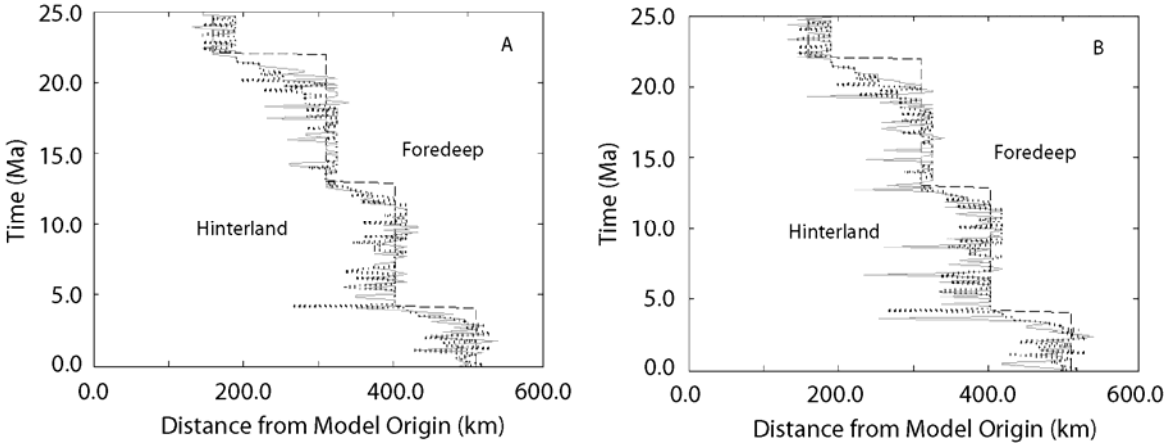

Figure 9: Gravel-sand interface time series data for the (A) gradual and rapid uplift models and the (B) rapid uplift and climate change models. In figure A the gradual and

rapid uplift models are represented by the solid and dotted lines respectively and in figure B the climate change and rapid models are represented by the solid and dotted lines respectively. The location of the deformation front is shown by the dashed line in both plots.

APPENDIX C: QUANTIFYING THE EFFECT OF HYDROLOGIC VARIABILITY ON BEDLOAD SEDIMENT TRANSPORT IN ALLUVIAL CHANNELS

Manuscript in review with Geomorphology

Todd M. Engelder, Department of Geosciences, University of Arizona, 1040 E. Fourth St., Tucson AZ, 85721, USA.

Jon D. Pelletier, Department of Geosciences, University of Arizona, 1040 E. Fourth St., Tucson AZ, 85721, USA.

Abstract

Existing equations for predicting the long-term bedload sediment flux in alluvial channels include mean discharge as a controlling variable but do not explicitly include variations in discharge through time. In this paper, we develop an analytic equation for the long-term bedload sediment flux in alluvial channels that incorporates instantaneous sediment transport equations and the frequency-size distribution of flood events, taking into account both the mean and coefficient of variation of discharge for a channel with a prescribed slope and grain size. Three applications of the resulting equation are considered. First, the equation is used to refine estimates for the effective diffusivity of alluvial channels within the framework of the diffusion model for longitudinal profile evolution. Second, the geomorphic effectiveness of end-member annual-runoff regimes is considered, taking into account the inverse relationship between the mean and coefficient of variation of discharge in alluvial channels. The results indicate that an alluvial channel with high effective annual runoff transports more sediment per unit time than the same

channel would with low effective annual runoff despite the fact that high effective annual runoff conditions may lack the extreme events characteristic of low effective annual runoff conditions. Third, the return period of the effective discharge (i.e. the discharge that contributes the most sediment to the long-term bedload sediment flux) is calculated as a function of climate. Channels in humid-to-temperate climates have effective-discharge return periods of months to decades, while the return periods of the effective discharge for extremely arid climates can be up to several hundred years.

Index Terms- sediment transport, climate impacts, stochastic hydrology, diffusion

1. Introduction

A better understanding of long-term bedload sediment fluxes is needed to properly manage floodplains and reservoirs and to predict how alluvial channels will respond to future climatic and hydrologic changes (Harlin, 1978; Goodwin, 2004). Long-term in this context refers to time scales of decades to centuries, i.e. sufficiently long that the estimated sediment flux for a given location includes the cumulative effects of many flood events but not so long that the estimate averages over the effects of different climatic conditions. Quantifying mean bedload sediment fluxes over geologic time scales is necessary for understanding the evolution of sedimentary basins, because upstream sediment flux acts as a principal boundary condition for terrestrial and marine depozones (Paola et al., 1992; Molnar, 2004).

Here we derive an analytic equation for the long-term sediment transport for an alluvial channel with a prescribed grain size, slope, and mean and coefficient of variation of discharge. Wolman and Miller (1960) first proposed that the geomorphic work (i.e. long-term sediment transport) performed by a channel could be quantified by integrating the product of a sediment transport function and a frequency-size distribution of discharge over the range of all possible discharges. They referred to the product of these two functions as the "effectiveness function." An abundant literature now exists that computes the long-term sediment flux by integrating the product of the frequency distribution of daily discharge with a site-calibrated sediment rating curve for specific channels (e.g. Kettner and Syvitski, 2008), but no generally-applicable analytic equations

for predicting long-term sediment flux are available that incorporate both the mean and coefficient of variation of discharge. Such an equation would be useful for predicting the rates of topographic evolution of alluvial channels as well as for predicting channel response to climatic and anthropogenic changes.

Sediment discharge can be divided into a suspended-load component, i.e. sediment that moves in the water column while only occasionally touching the bed, and a bedload component, i.e. sediment that moves close to the bed by repeated instances of rolling, sliding, and saltation. In this paper we focus on the bedload component for three reasons. First, bedload sediment transport is more closely related to local hydraulic conditions. Second, many bedload formulae have been proposed that work reasonably well. Third, the topographic evolution of alluvial channels is most closely related to bedload because suspended sediment load is sourced primarily from hillslopes and, while some deposition of suspended load can occur in channel beds, most suspended sediment moves from hillslopes to depositional basins (alluvial fans and deltas) without affecting the channel geometry to the same extent as bedload. In contrast, the variation in bedload sediment fluxes along a channel longitudinal profile is the primary driver for aggradation and incision of alluvial channel beds.

The diffusion equation is a commonly used model for simulating the topographic evolution of alluvial channels in sedimentary basins over geologic timescales (Flemings and Jordan, 1989; Paola et al., 1992; Marr et al., 2000). The diffusion equation applies

mass-conservation principles to predict the rate of erosion or deposition at a point along a channel to the gradient of long-term sediment flux at that point. As such, proper application of the diffusion equation requires accurate models for how long-term bedload sediment fluxes relate to the controlling parameters of channel slope, grain size, and hydrologic forcing. More specifically, the diffusion equation assumes that sediment fluxes are proportional to the local slope gradient. It is written as the following:

$$\frac{\partial h}{\partial t} = \kappa \frac{\partial^2 h}{\partial x^2} \tag{1}$$

where h is the elevation of the channel bed (m), κ is diffusivity (m^2/yr), t is time (yr) and x is the horizontal distance with respect to the model origin (m). The diffusivity parameter of the diffusion equation, which is the proportionality constant between sediment flux and channel slope, is a function of all of the variables that control bedload sediment flux, i.e. grain size, channel width, and the hydrological forcing (i.e. the mean and variability of discharge). Paola et al. (1992) derived an expression for diffusivity using the Meyer-Peter and Mueller (1948) sediment transport relation. Paola et al.'s (1992) expression was a function of mean discharge and channel morphology. As such, it did not incorporate grain size or the variability of discharge. Later, Marr et al. (2000) derived a diffusivity that included grain-size effects and a term for hydrologic variability; however, the authors chose to set their variability parameter to unity to simplify the results. There is clear evidence, however, that the variability of discharge affects long-

term sediment transport rates. For example, studies that carefully document the temporal variability of sediment transport often show that the largest events transport the most sediment (Inman and Jenkins, 1999). As such, the mean discharge cannot be the only variable that controls long-term sediment flux. At larger spatial and temporal scales, Leier et al. (2005) documented lower slopes of fluvial megafans in areas of higher discharge variability but similar mean discharge worldwide. Leier et al.'s (2005) observation implies that variability in discharge must be a controlling factor on long-term sediment transport rates because the slopes of the fans reflect the effective diffusivity of the fluvial system. In this paper we derive an analytic expression for the diffusivity that incorporates hydrologic variability.

One explanation why discharge variability is important for long-term transport rates is that sediment transport is a nonlinear function of discharge. Analysis of bedload transport in gravel-bed channels reveals that most power-law rating-curve exponents range between 1.5 and 4.4 for gravel-bed channels (Goodwin, 2004; King et al., 2004). However, power-law rating-curve exponents can also exceed 5.0 when armoring occurs (Emmett and Wolman, 2001). Such strongly nonlinear behavior increases the importance of rare, large flood events relative to more frequent, smaller floods.

Molnar (2001) posed the question of whether channels in arid or humid climates transport more sediment as bedload. Analysis of channel hydrographs reveals that discharge variability, expressed as a coefficient of variation, increases with increasing aridity.

Turcotte and Greene (1993), for example, analyzed peak annual discharge for 10 channels in various climates across the United States. Their results showed that the ratio of the frequency of the largest floods to that of the mean flood increased significantly with increasing aridity. Molnar et al. (2006) found a similar correlation between the power-law exponents for flood frequency and effective annual precipitation for an additional 159 channels across the United States. In the most comprehensive analysis to date, McMahon et al. (2007) analyzed the sample statistics of 1221 channels globally. Their results confirm a negative correlation between the coefficient of variation (i.e., the standard deviation normalized by the mean) of annual discharge and the mean annual runoff. Therefore, as climates shift to greater aridity, the variability in discharge increases.

Molnar (2001) concluded that channels in arid climates would transport more sediment than the same channel in a humid climate. In effect, Molnar (2001) argued that the increase in the flashiness of discharge more than compensated for the decrease in mean discharge with increasing aridity. The reason for this is related to the fact that large floods are so much more effective, per unit discharge, than small floods. In a revised analysis, however, Molnar et al. (2006) pointed to a normalization error in Molnar (2001) and stated that unless the threshold for entrainment was high enough to be exceeded only by very large floods, greater aridity would not likely result in larger transport rates compared to more humid conditions. Molnar et al.'s (2006) analysis was limited, however, in that they did not explicitly incorporate sediment transport into their study. As such, the

relationship between climate and long-term sediment transport is still not well constrained and the question posed by Molnar (2001) remains to be fully answered.

In addition to diffusivity, our analytic solution for the long-term bedload sediment transport also constrains the effective discharge. Wolman and Miller (1960) defined the effective discharge as the discharge responsible for transporting more sediment than any other discharge. Several studies provide analytic solutions for the effective discharge (Nash, 1994; Goodwin, 2004; Doyle et al., 2007). Nash (1994), for example, showed that the effective discharge for suspended sediment was a function of both the mean and coefficient of variation of discharge when the effectiveness function is the product of a sediment rating curve and a two-parameter lognormal distribution. Goodwin (2004) extended this analysis to include the use of effectiveness functions that were the product of more general sediment transport equations and several types of frequency distributions. Although transport thresholds were included in deriving some of his analytic solutions, results showed that the threshold for transport did not change the magnitude of the effective discharge as long as the effective discharge was significantly greater than the threshold for entrainment. These studies and others show that both numerical and analytic solutions for effective discharge can be used to accurately predict the effective discharge for bedload sediment transport in modern channels (Torizzo and Pitlick, 2004; Barry et al., 2008). Goodwin (2004) also stated that the analytic solutions he derived could be used to predict changes in effective discharge caused by future changes in hydrology and sediment supply. However, these studies did not take into

consideration the covariation between the mean and the coefficient of variation of discharge considered in this paper.

Here we derive an analytic equation for the long-term bedload sediment flux that includes the mean and coefficient of variation of discharge. We then explore three applications of that equation. First, recasting the analytic solution as a function of channel gradient yields an analytic solution for the diffusivity as a function of effective mean discharge and the coefficient of variation of mean daily discharge. We then use this equation to determine the sensitivity of diffusivity to each controlling parameter and compare our results to reported diffusivity values from the literature. Second, we determine the relationship between long-term bedload sediment flux and hydrologic distribution, which is a function of climate, for an alluvial channel of a prescribed slope and grain size. Third, we derive an expression for the effective discharge and the return period of that effective discharge. The results of that analysis enable us to assess how the magnitude and frequency of the channel-forming discharge depends on the hydrologic distribution and, by extension, to climate.

2. Analytic Solutions

2.1. Derivation of an analytic equation for long-term bedload sediment flux

The long-term bedload sediment flux per unit channel width in an alluvial channel is given by the integral of the effectiveness function. Although the effectiveness function is generally cast in terms of volumetric discharge, here we choose to write it as a function of Shields stress, τ_* (i.e. the dimensionless shear stress), in order to simplify the expression and facilitate comparison between channels of different geometries and textures. The expression for the long-term bedload sediment flux as a function of Shields stress and critical Shields stress is:

$$\overline{q_{s*}} = \int_{\tau_{*cr}}^{\infty} q_{s*}(\tau_*, \tau_{*cr}) f(\tau_*) d\tau_* \qquad (2)$$

where q_{s*} is the instantaneous, non-dimensional volumetric bedload sediment flux per unit channel width, and τ_{*cr} is the critical Shields stress for sediment entrainment (also dimensionless). In this paper, all variables that have a bar above them represent time-averaged (i.e., long-term) values.

Sand- and gravel-bed channels must be considered separately because different sediment transport formulae apply to each type of channel (discussed in the next paragraph). For sand-bed channels, we set the lower limit of integration in (2) to 0 and the upper limit to ∞. The lower limit of integration is 0 because commonly-used sediment transport formulae for sand-bed channels, including the formula we adopt in this paper, do not include a threshold for transport. At the upper end of the integration, a natural upper bound to Shields stress exists that is largely controlled by the limit of water that can

delivered by a storm to a basin over a given period of time. Instead of solving for the upper bound as a function of basin parameters (e.g. size and drainage density) and climate the upper bound is set to ∞. The simplification of choosing no upper limit for the range of integration is reasonable because the frequencies of discharges located at the extreme end of the distribution tail are sufficiently low that such storms comprise a very small component of the long-term sediment transport rate. For gravel-bed channels, we set the lower limit of integration to equal the critical Shields stress because, by definition, no transport occurs below the critical Shields stress. However, two possible choices exist for the upper limit in the gravel-bed channel case: (1) Shields stress can continue to increase as discharge increases (necessitating an upper limit of integration of ∞), or (2) Shields stress can be limited to values between 1.2 and 1.4 times the critical value to account for channel widening in response to large floods (i.e., the self-forming channel of Parker (1978)). If the channel is self-forming, then the integral must be the sum of two terms: an integral similar to (1) when the Shields stress is less than either 1.2 or 1.4 times the critical Shields stress and an integral with a constant transport rate when the Shields stress exceeds either 1.2 or 1.4 times the critical Shields stress. Like gravel-bed channels, sand-bed channels do widen in response to floods that generate shear stresses sufficient to entrain channel bank sediment. However, we chose to not to explore the effects of limiting shear stress in sand-bed channels because the specific value for the upper bound in Shields stress is not as well constrained in the literature for sand-bed channels.

Two general classes of sediment transport formulae can be applied to solve for the long-term bedload sediment flux: site-specific sediment rating curves and general transport equations. Sediment rating curves are generally cast as a power-law function of discharge and the coefficient and exponent of each rating curve are calibrated to a specific reach within a channel and for a given period of time. Rating curves have the advantage of a simple functional form and they match observed sediment fluxes in natural streams better than general transport equations. However, they have the disadvantage of requiring site-specific and time-specific calibration. More general transport equations are required to predict instantaneous sediment fluxes over a broad range of channel conditions without site-specific calibration. Numerous sediment transport formulae have been developed over the last century for this purpose. Empirical equations that predict sediment flux as a function of shear stress (Meyer-Peter and Muller, 1948; Engelund and Hansen,1967; Parker et al., 1982; Wiberg and Smith, 1989), as a stochastic function of sediment movement (Einstein, 1950), or as a function of stream power (Bagnold; 1980) have been tested against observed sediment transport rates for channels (e.g. Gomez and Church, 1989; Barry et al., 2004). Gomez and Church (1989) found that the majority of bedload sediment transport formulae over-predict transport rates. These authors attributed this over-prediction to bed-surface armoring and insufficient sediment supply to the reach. More recently, Barry et al. (2004) tested bedload sediment transport equations against sediment transport data collected in gravel-bed channels by the USGS and USDA Forest Service in Idaho and found no consistent relationship between sediment transport formulae performance and the degree to which each formula was calibrated or to the

complexity of the equation. While bedload sediment transport formulae have a limited ability to accurately predict instantaneous fluxes within channels, the averaging effect of computing long-term sediment fluxes mitigates these problems to some extent. Both studies also found that formulae with thresholds for entrainment often erroneously predicted zero transport when the discharge was finite but below the predicted threshold for transport. As a result, Barry et al. (2004) found that the Ackers and White (1973) and Parker et al. (1982) equations preformed better than equations that contain a threshold term for entrainment (e.g. Meyer-Peter and Muller (1948)). Despite the increase in accuracy, however, the complexity of the Ackers and White (1973) and Parker et al. (1982) equations makes both integration and calibration of the analytic solutions difficult. Therefore, we compute bedload sediment flux in gravel-bed channels in this study using the following relationship derived by Wiberg and Smith (1989):

$$q_{s*} = 9.64\,\tau_*^{1/6}(\tau_* - \tau_{*\mathrm{cr}})^{3/2} \tag{3}$$

Equation (3) is applicable over a broad range of grain sizes from medium sand to gravel (i.e., 0.35 to 28.6 mm). For sand-dominated channels with grain sizes less than 2 mm, we use the Engelund and Hansen (1967) transport equation, i.e.

$$q_{s*} = \left(\frac{0.05}{C_\mathrm{f}}\right)\tau_*^{5/2} \tag{4}$$

where C_f is a dimensionless drag coefficient, assumed here to be 0.01. Equation (4) does not contain a threshold for entrainment and is a simple power-law function of Shields stress.

Analyses of hydrologic time-series data show that both mean daily and mean annual channel discharge can follow normal, lognormal, power-law, and other distributions with parameters that depend on drainage basin area and climate (e.g. Leopold et al., 1964; Turcotte and Greene, 1993; Molnar et al., 2006). Further analysis of channels from North America and Europe reveal that the two-parameter lognormal and gamma distributions best describe the time series data for mean annual discharge (Goodwin, 2004; McMahon et al., 2007). Equation (2) is cast as a function of Shields stress instead of discharge, and thus, a representative distribution for Shields stress is required for this analysis. When channel flow is uniform and steady, Shields stress is a power-law function of discharge. In this paper we assume that discharge, and hence Shields stress, follows a two-parameter lognormal distribution. We use the lognormal distribution because it is a commonly used two-parameter distribution for discharge that can accurately represent the entire distribution of discharge events including small, common discharges and large, rare discharges (Goodwin, 2004; McMahon et al., 2007). Written in terms of τ_*, this distribution is given by

$$f(\tau_*) = \left(\frac{1}{\tau_* \, \sigma_{\ln\tau_*} \sqrt{2\pi}} \right) \exp\left(\frac{-\left(\ln\tau_* - \mu_{\ln\tau_*}\right)^2}{2\,\sigma_{\ln\tau_*}{}^2} \right) \tag{5}$$

where $\sigma_{\ln\tau_*}$ is the standard deviation of ln τ_* and $\mu_{\ln\tau_*}$ is the mean of ln τ_*. Substituting (3) and (5) into (2) yields an effectiveness function for τ_* that can be applied to gravel-bed channels in cases when τ_* is not limited near τ_{*cr} for high discharges:

$$\overline{q_{s*}} = \int_{\tau_{*cr}}^{\infty} 9.64\,\tau_*^{1/6}(\tau_* - \tau_{*cr})^{3/2}\left(\frac{1}{\tau_*\sigma_{\ln\tau_*}\sqrt{2\pi}}\right)\exp\left(\frac{-\left(\ln\tau_* - \mu_{\ln\tau_*}\right)^2}{2\,\sigma_{\ln\tau_*}^{\;2}}\right)d\,\tau_* \qquad (6)$$

A similar expression for sand-bed channels can be obtained by substituting (4) and (5) into (2). However, the limits of integration are between 0 and ∞ for the sand-bed case. In order to compute the integral of (6) analytically, it is necessary to perform a Taylor expansion of the Wiberg and Smith (1989) formula, i.e. (3), in order to yield an infinite series of solvable integrals. We used the following Taylor expansion:

$$(\tau_* - \tau_{*cr})^{3/2} = \tau_*^{\,3/2} - \left(\frac{3}{2}\right)\tau_*^{\,1/2}\tau_{*cr} + \left(\frac{3}{8}\right)\tau_*^{\,-1/2}\tau_{*cr}^{\;2} + \ldots\ldots + H.O.T. \qquad (7)$$

where *H.O.T.* stands for higher-order terms. Upon integration of (6), the resulting equation is a function of the mean and standard deviation of the normally distributed ln τ_*. As such, we must solve for the mean and standard deviation of a lognormally transformed variable in terms of the mean and variance of the original variable, which yields the following solutions:

$$\mu_{\ln\tau_*} = \ln\left(\overline{\tau_*}\right) - \left(\frac{\ln\left(1 + C_{v,\tau_*}{}^2\right)}{2}\right) \tag{8}$$

$$\sigma_{\ln\tau_*} = \ln\left(1 + C_{v,\tau_*}{}^2\right)^{1/2} \tag{9}$$

where $\bar{\tau}_*$ is the mean of τ_*, C_{v,τ_*} is the coefficient of variation of τ_*. Substituting (8) and (9) into the infinite-series solution for the integral of (6) results in the following expression:

$$\overline{q_{s*}} = \sum_{k=1}^{\infty} \alpha \bar{\tau}_*^{-\left(\frac{3k-8}{3}\right)} \left(1 + C_{v,\tau_*}{}^2\right)^{\left(\frac{(3k-8)(3k-5)}{18}\right)} [1 - \mathrm{erf}(\beta)] \tag{10}$$

$$\beta = \left(\frac{-3\ln\bar{\tau}_* + (3k - \frac{13}{2})\ln(1 + C_{v,\tau_*}{}^2) + 3\ln\tau_{*\,\mathrm{cr}}}{3\sqrt{2}\ln(1 + C_{v,\tau_*}{}^2)^{(1/2)}} \right)$$

$$\alpha = \begin{cases} \left(\frac{9.64}{2}\right) & if, k = 1 \\ \left(\frac{9.64}{2}\right)\left(\frac{(-1)^{k-1}\tau_{*cr}^{k-1}}{(k-1)!}\right)\prod_{m=1}^{k-1}\left(\frac{5}{2} - m\right) & if, k > 1 \end{cases}$$

where k and m are summation indices and α and β are constants defined in equation 10. The symbol erf() stands for the Error function. Equation 10 predicts the long-term bedload sediment flux for a given lognormal distribution of τ_*. In practice, only the first few terms in the series are required in order to implement (10) because the series

converges to several-decimal-point-accuracy with just a few terms for most values of $\bar{\tau}_*$ and C_{v,τ_*}. We verified the accuracy of the form of (10) by comparing its predictions to a numerically-integrated calculation of (6). This validation procedure illustrates the power of a closed-form analytic expression for long-term sediment flux. Although the expression in (10) is lengthy, numerical integration requires different integration step sizes for different values of C_{v,τ_*} (to insure that the final solutions for long-term sediment flux represent the entire range of contributing discharge), and thus determining the relationships between long-term sediment flux and $\bar{\tau}_*$ and C_{v,τ_*} is less than straightforward. The series solution, in contrast, provides an exact result without numerical integration.

For gravel-bed channels that adjust to high Shields stresses by widening, the integral is divided into two ranges of Shields stress:

$$\overline{q_{s*}} = \sum_{k=1}^{\infty} \alpha \bar{\tau}_*^{-\left(\frac{3k-8}{3}\right)} \left(1 + C_{v,\tau_*}{}^2\right)^{\left(\frac{(3k-8)(3k-5)}{18}\right)} \left[\operatorname{erf}(\beta) - \operatorname{erf}(\beta)\right] + \gamma \qquad (11)$$

$$\gamma = 9.64\left[(1+\varepsilon)\tau_{*cr}\right]^{1/6}\left(\varepsilon\,\tau_{*cr}\right)^{3/2}\left[\frac{1}{2} - \frac{1}{2}\operatorname{erf}\left(\frac{\ln((1+\varepsilon)\tau_{*cr}) - \ln\bar{\tau}_* + (1/2)\ln(1+C_{v,\tau_*}{}^2)}{\sqrt{2}\ln(1+C_{v,\tau_*}{}^2)^{1/4}}\right)\right]$$

where γ is the contribution to the long-term sediment flux when Shields stress is greater than $(1+\varepsilon)\tau_{*cr}$ and ε is equal to a constant between 0.2 and 0.4. The terms α and β are the same as in (10) except that τ_{*cr} is replaced with $(1+\varepsilon)\tau_{*cr}$ in the left-most *erf* (β) term.

We also solved for the long-term bedload sediment flux by integrating the product of the Engelund and Hansen (1967) transport equation and the lognormal distribution. In this case, performing a Taylor expansion on the transport equation was not necessary because the resulting integral has a known solution. The following is the expression for long-term bedload sediment flux applicable to sand-bed channels:

$$\overline{q_{s*}} = \left(\frac{0.05}{2C_{\mathrm{f}}}\right)\overline{\tau_*}^{5/2}\left(1 + C_{\mathrm{v},\tau_*}{}^2\right)^{15/8} \tag{12}$$

In order to apply (10-12) to a specific set of climatic and geomorphic conditions we must relate the mean channel parameters (i.e., grain size, grain density, channel bed slope and the frequency-size distribution of discharge) to the Shields stress. When discharge is relatively steady and uniform, the instantaneous discharge is related to the instantaneous τ_* through the following equations:

$$\tau_* = \frac{(Qn)^{3/5} S^{7/10}}{w^{3/5}\left(\frac{\rho_{\mathrm{S}} - \rho_{\mathrm{f}}}{\rho_{\mathrm{f}}}\right) d} \tag{13}$$

$$\tau_* = \frac{Q^{3/10} n^{3/5} S^{7/10}}{b^{3/5}\left(\frac{\rho_s - \rho_f}{\rho_f}\right) d} \tag{14}$$

where Q is the volumetric discharge per unit channel width (m^3/s), n is the Manning's roughness coefficient (approximately 0.035 for moderately rough gravel-bed channels), S is the local channel bed slope, d is the sediment grain diameter (m), w is the channel width (m), ρ_s is the grain density (kg/m^3), ρ_f is the fluid density (kg/m^3) and b is the proportionality coefficient for the power-law relationship between w and Q (i.e., its units are $s^{1/2}/m^{1/2}$ when Q has units of m^3/s and the power-law exponent is equal to 1/2). We solved for a relationship between Shields stress and volumetric discharge because using volumetric discharge facilitates comparison with data reported in the literature. A square-root relationship between channel width and discharge (i.e., $w = bQ^{1/2}$) was applied to convert volumetric discharge to discharge per unit channel width to yield (14). Several studies have constrained the range of values for b and the power-law exponent relating width and discharge for U.S. channels located in humid to semi-arid regions (Blench, 1952; Leopold and Maddock, 1953; Simons and Albertson, 1963). They found that b values vary from approximately 3.1 to 6.3 depending on the erodibility of the bank material. The exponent relating width and discharge ranged between 0.50 and 0.51. The instantaneous Shields stress is also a function of grain diameter d. Of course, channels are not comprised of sediment grains of uniform diameter. As such, the value of d should be chosen to be a representative value of the channel bed material, e.g. d_{50} or d_{80} (i.e., the

median or the 80th percentile grain size of the distribution, respectively). Our analytic approach, however, is not limited to channel beds with uniform grain sizes or distributions that can be characterized by a single grain size. In the case of more complicated grain size distributions, the range of channel bed grain size can be divided into multiple bins. Then our analytic solution can be used to compute the component (i.e., normalized by the bin's weight percent of the distribution) of long-term bedload sediment transport rates contributed by each grain size bin to the total long-term bedload sediment transport rate. Although long-term bedload sediment transport rates can be calculated for a fixed distribution of grain sizes, long-term changes in channel texture due to hydraulic sorting and changes in upstream sediment supply cannot be properly addressed by our analytic solution. As such, sensitivity study results discussed later in the paper are presented for channels of uniform grain size.

Long-term sediment fluxes result from the cumulative effect of many discharge events. As such, equations (13 and 14) were modified to relate the mean and variation of Shields stress to those of discharge. We derived these equations by first linearizing (13) and (14) as functions of ln Q through a logarithmic transformation. Then, we replaced the logarithms of Shields stress and discharge with the mean and standard deviations of the logarithms of Shields stress and discharge. This was accomplished by using standard relationships for the effect of linear transformation on the mean and the variance of a variable (i.e., ln τ_* is a linear transform of ln Q). As an example, we show the equations that were derived from (14):

$$\mu_{\ln\tau n} = (3/10)\,\mu_{\ln Q} + \ln\left(\frac{n^{3/5}S^{7/10}}{b^{3/5}\left(\frac{\rho_s-\rho_f}{\rho_f}\right)d}\right) \tag{15}$$

$$\sigma_{\ln\tau n} = (3/10)\,\sigma_{\ln Q} \tag{16}$$

where μ_{lnQ} and $\sigma_{\ln Q}$ are the mean and the standard deviation of ln Q. Equations similar to (8) and (9), but written in terms of discharge instead of Shields stress, were then substituted into (15) and (16) to solve for the relationship between the mean and variation of both Q and τ_*:

$$\bar{\tau}_* = \left(\frac{\bar{Q}^{3/5}n^{3/5}S^{7/10}}{w^{3/5}\left(\frac{\rho_s-\rho_f}{\rho_f}\right)d\left(1+C_{v,Q}{}^2\right)^{6/50}}\right) \tag{17}$$

$$\bar{\tau}_* = \left(\frac{\bar{Q}^{3/10}n^{3/5}S^{7/10}}{b^{3/5}\left(\frac{\rho_s-\rho_f}{\rho_f}\right)d\left(1+C_{v,Q}{}^2\right)^{21/200}}\right) \tag{18}$$

$$C_{v,\tau_*} = \left[\left(1+C_{v,Q}{}^2\right)^{9/25}-1\right]^{1/2} \tag{19}$$

$$C_{v,\tau_*} = \left[\left(1 + C_{v,Q}{}^2\right)^{9/100} - 1\right]^{1/2} \quad (20)$$

where $\overline{Q}$ is the mean volumetric discharge (m^3/s) and $C_{v,Q}$ is the coefficient of variation of volumetric discharge. Notice that channel width has been removed from equations 18 and 20, and thus, these equations can be applied to channels where the site-specific relationship between discharge and channel width is not available. However, this approach only applies to channels that are effectively stable because the power-law relationship between channel width and discharge with an exponent of 1/2 does not apply to channels that are actively incising. Equations (17-20) can then be substituted into (10-12) in order to quantify the long-term bedload sediment flux in an alluvial channel in terms of the mean and the coefficient of variation of discharge. Although (17-20) do not explicitly include seasonal variability in discharge, the coefficient of variation of discharge is larger in regions with more seasonality in discharge, so the effects of seasonality are implicitly included.

Channel slope was the remaining parameter in (17-18) required to convert the discharge distribution to the Shields stress distribution, taking into account the channel geometry and channel bed texture. Prescribing a channel slope independently of shear stress for input into (18) can result in unrealistic Shields stress values at large discharges. Over-estimating the Shields stresses during larger discharges would result in an overestimation of long-term bedload sediment transport rates and effective discharge return periods. Therefore, we calculated the channel slope such that the Shields stress for large

discharges was in an acceptable range. Using data from Church and Rood (1983), Marr et al. (2000) showed that gravel- and sand-bed channels function at two distinct ranges of Shields stress (i.e., 0.025 to 0.14 for gravel-bed channels and 0.5 to 2.0 for sand-bed channels) during discharges of channel-forming significance. The return periods of the channel-forming discharges included in the Church and Rood (1983) dataset range from 0.6 years to several years. Additional studies of channels located in humid to temperate climates found that bankfull discharges, which can represent the channel-forming discharge, have return periods on the order of one to several years with an average of 1.4-1.5 years (Leopold et al., 1964; Knighton, 1998). Based on these observations, we calculated the channel slope such that the Shields stresses were within the range observed by Marr et al. (2000) for discharges with return periods of one to several years. Equation (14) was rearranged to solve for the channel slope that satisfies this condition:

$$S = \left(\frac{\tau_{*\mathrm{cf}}\, b^{3/5} \left(\frac{\rho_s - \rho_f}{\rho_f} \right) d}{Q_{\mathrm{cf}}{}^{3/10} n^{3/5}} \right)^{10/7} \tag{21}$$

where Q_{cf} is the channel-forming discharge (m^3/s) and $\tau_{*\mathrm{cf}}$ is the channel-forming discharge Shields stress. A discharge with a specific return period can be calculated directly from the lognormal distribution for discharge. However, choosing a unique value for the prescribed channel-forming discharge return period is problematic because the

variation of this return period as a function of channel cross-section, channel bed texture and hydrologic distribution is not well constrained. Instead of picking a single value for the return period, we chose to test the sensitivity of our analytic solution to the prescribed channel-forming discharge return period. Specifically, two channel slopes calculated using the 1.5 and 6.0 year discharges were applied in our long-term bedload sediment flux and effective discharge return period sensitivity studies.

2.2. Derivation of the diffusivity coefficient

The analytic equation for long-term bedload sediment flux can be applied to a number of geomorphic problems. One application is to derive an analytic expression for the diffusivity coefficient within the context of the diffusion model for the evolution of alluvial channel profiles. A key assumption of diffusion modeling is that sediment flux is linearly proportional to the local channel slope. Equations (10-12) show that long-term bedload sediment flux is a nonlinear function of $\bar{\tau}_*$ and therefore of *S*. As such, the analytic expression for the long-term sediment transport rate must be linearized as a function of slope in order to derive an expression for diffusivity. The diffusion model, while it does not capture the full complexity of sedimentary basin evolution, is nevertheless extremely useful and, when implemented in a model of sedimentary basin evolution, permits the use of greater time steps compared to event-based models (e.g. Paola et al., 1992; Ritchie et al., 1999; Coulthard et al., 2002).

Similarly to equations (10) and (11), the diffusivity κ that appears in (1) can, for gravel-bed channels, also be written as an infinite series:

$$\kappa = \sum_{k=1}^{\infty} \alpha \sqrt{\left(\frac{\rho_s - \rho_f}{\rho_f}\right) g d}\, d \left(\frac{\bar{\tau}_*^{-\left(\frac{3k-8}{3}\right)}}{S_0}\right) \left(1 + C_{v,\tau_*}{}^2\right)^{\left(\frac{(3k-8)(3k-5)}{18}\right)} \left[1 - \mathrm{erf}(\beta)\right] \tag{22}$$

$$\kappa = \sum_{k=1}^{\infty} \alpha \sqrt{\left(\frac{\rho_s - \rho_f}{\rho_f}\right) g d}\, d \left(\frac{\bar{\tau}_*^{-\left(\frac{3k-8}{3}\right)}}{S_0}\right) \left(1 + C_{v,\tau_*}{}^2\right)^{\left(\frac{(3k-8)(3k-5)}{18}\right)} \left[\mathrm{erf}(\beta) - \mathrm{erf}(\beta)\right] + \gamma \tag{23}$$

$$\gamma = \sqrt{\left(\frac{\rho_s - \rho_f}{\rho_f}\right) g d}\, d \left(\frac{9.64\left[(1+\varepsilon)\tau_{*cr}\right]^{1/6}\left(\varepsilon\tau_{*cr}\right)^{3/2}}{S_0}\right) \left[\frac{1}{2} - \frac{1}{2}\mathrm{erf}\left(\frac{\ln\left[(1+\varepsilon)\tau_{*cr}\right] - \ln \bar{\tau}_* + (1/2)\ln(1 + C_{v,\tau_*}{}^2)}{\sqrt{2}\ln(1 + C_{v,\tau_*}{}^2)^{1/4}}\right)\right]$$

where g is the gravitational acceleration (m/s^2), and α and β are the same as in (10) (except that S is replaced by S_0, the average slope of the basin that is being modeled with the diffusion equation). Equations (22) and (23) are expressions for the diffusivity of gravel-bed channels that include the mean and coefficient of variation of discharge, the mean channel geometry, sediment texture, and the densities of sediment and water. The diffusivity κ for sand-bed channels is given by:

$$\kappa = \sqrt{\left(\frac{\rho_s - \rho_f}{\rho_f}\right) g d}\left(\frac{0.05 d}{2C_f}\right)\left(\frac{\bar{\tau}_*^{5/2}}{S_0}\right)\left(1 + C_{v,\tau_*}{}^2\right)^{15/8} \tag{24}$$

The average slope S_0 can be prescribed in the analysis or it can be estimated from sediment and hydrologic parameters using (21).

2.3. Numerical and analytic solutions for the effective discharge

A third application for our analytic solution is to calculate the effective discharge and its return period for gravel- and sand-bed channels. The peak of the effectiveness function is the effective discharge that transports more sediment than all other discharge magnitudes. For gravel-bed channels, setting the derivative of the product of (3) and (5) to zero and solving for the Shields stress corresponding to the peak of the effectiveness function results in an equation that cannot be solved analytically. Therefore, we chose to numerically solve for the effective discharge for gravel-bed channels.

An analytic solution does exist for the effective discharge of sand-bed channels because of the simpler form of the Engelund and Hanson (1967) transport equation. To solve for the effective discharge we first substituted the analytic solution for the effective Shields stress into (14). Equations (8) and (9) were used to replace the mean and variance of the logarithms of Shields stress that are present in the analytic solution for the effective Shields stress with the mean and variance of Shields stress for input into (14). We then rearranged the resulting equation to obtain the following analytic solution for the effective discharge for sand-bed channels:

$$Q_e = \left(\frac{\bar{\tau}_* \left(1 + C_{v,\tau_*}{}^2\right)^{(\eta - 3/2)} b^{3/5} \left(\frac{\rho_s - \rho_f}{\rho_f} \right) d}{n^{3/5} S^{7/10}} \right)^{10/3} \quad (25)$$

where Q_e is the effective discharge (m^3/s) and η is the exponent of the power-law sediment transport function (i.e. 5/2 for the Engelund and Hansen (1967) transport function). The resulting effective discharge for gravel- and sand-bed channels can then be substituted into the following equation to solve for the return period of the effective discharge:

$$T_{Q_e} = \left(1 - \left[\frac{1}{2} + \frac{1}{2} \mathrm{erf} \left(\frac{\ln Q_e - \ln \overline{Q} + (1/2) \ln\left(1 + C_{v,Q}{}^2\right)}{\sqrt{2 \ln\left(1 + C_{v,Q}{}^2\right)}} \right) \right] \right)^{-1} \quad (26)$$

where T_{Q_e} is the effective discharge return period (units of the return period depend on the sampling interval for Q).

3. Preliminary data analysis required for validation of model predictions

3.1. Climate effect on long-term bedload sediment flux

One of the goals of this study was to determine the geomorphic effectiveness of end-member climates. Given equations for the ability of a given channel to transport sediment in a humid versus a more arid climate, we can start to place constraints on how channels might change their geometry as climate changes. Statistical analysis of discharge data from U.S. channels shows that with increasing aridity, the number of larger floods relative to smaller floods increases (Turcotte and Greene, 1993). This observation has since been supported by other studies (Molnar, 2001; Molnar et al., 2006). A comparison of long-term bedload sediment flux for end-member climates must include this observed covariation between the mean and variability of discharge as functions of climate. Therefore, relationships between the variation in discharge, mean annual discharge, and mean annual runoff were required to link the discharge distribution input into our analytic solutions to climate.

Although previous studies have correlated the mean and the variation of discharge with climate, further statistical analysis is required to obtain a relationship that can be applied to our analytic solution. Molnar et al. (2006) fit power-law distributions to 155 stream gauges within the United States and found a positive correlation between effective precipitation and the exponent of a power-law distribution. In this study we assume that discharge values are lognormally distributed. Power-law distributions are useful for characterizing the tail of the frequency-size distribution of discharge but they are less accurate at characterizing small, more common floods. McMahon et al. (2007) analyzed more than 1000 channels globally and found that the relationship between mean annual

runoff (i.e. mean annual discharge divided by contributing drainage basin area) and the coefficient of variation of annual discharge is approximately a power-law with an exponent of –0.299. Averaging discharge over 365 days causes the coefficient of variation for mean annual discharge to be less than the coefficient of variation for mean daily discharge. A decrease in variation between daily and annual data results from averaging out seasonal effects, large floods and days with zero discharge. However, daily variations have significant effects on long-term bedload sediment transport and thus should be included within the analytic solution. As such, we need to relate the coefficient of variation of daily discharge to the mean annual discharge or runoff.

To do this, a regression analysis of the coefficient of variation of daily discharge (C_{v,Q_d}) versus mean annual runoff (R) was conducted for channel discharge data obtained from the National Stream Water Quality Monitoring Network as part of the 1996 U.S. Geological Survey Digital Data Series DDS-37 (Alexander et al., 1996). We analyzed 590 channel discharge records across the United States for mean daily discharge and contributing drainage area. Only hydrograph records greater than 10 yr in duration were included in the analysis, yielding a final number of 530 stations. Large drainage basins are problematic because they are more likely to be impacted by nearby dams. The presence of dams commonly decreases C_{v,Q_d} relative to natural flow conditions by reducing seasonally large flows and enhancing low flows (Magilligan and Nislow, 2005).

The coefficient of variation of daily discharge and the mean annual runoff were calculated for each record and are plotted in Figure 1. When the data are plotted in log-log space there is a linear, inverse trend between the C_{v,Q_d} and R, which implies a power-law relationship with a negative exponent. Although these data are strongly correlated, there is significant scatter with many of the data points located near C_{v,Q_d} and R values of 1 and a few data points with anomalously low C_{v,Q_d} values. Channels with drainage basin areas less than 5,000 km^2 appear to plot toward greater C_{v,Q_d} values than channels with larger drainage basin areas for equivalent mean annual runoff values. One interpretation of this pattern is that small drainages may not have a continuous base flow throughout the year and as a result there is increased variability in discharge between storm and inter-storm periods in small basins. We chose to only include drainage basins that were larger than 5,000 km^2 (shown as black asterisks) in our best-fit linear regression analysis to reduce the influence of this basin-scale effect. The dashed line represents the resulting least-squares fit to the logarithm of the data. Removing data points that represent channels with smaller drainage areas improved the correlation coefficient from –0.45 to –0.63. Visual comparison of the trend line with the overall data shows that C_{v,Q_d} values calculated for the arid end of the plot would be potentially underestimated by a factor of 2 to 3. This trend is explained by the fact that the majority of the data falls between R values of 0.1 and 1 m, and thus, the trend line fits the data in the central region best (the data located on the extreme ends of the R axis is not well fit). A least-squares regression of binned data yields a fit that weighs each portion of the data throughout the range of mean runoff values equally. The data were binned by averaging the points within each

bin spanning an order of magnitude variation of R. We then performed a least-squares regression on the new data to calculate the solid line in Figure 1, i.e.

$$C_{v,Q_d} = 0.868\, R^{-0.27} \tag{27}$$

Equation (27), which is represented by the solid line in Figure 1, appears to more accurately fit the data located on the arid end of the R axis than the regression for the non-binned basins that are greater than 5,000 km^2 (dashed line). However, it's difficult to assess if the new power-law improves the accuracy on the humid end of the R axis because there are few large drainage basins in the U.S. that receive more than a meter of runoff per year.

Now that we have a relationship between C_{v,Q_d} and R, $\overline{Q}$ must be derived from R to compare channels of similar hydraulic parameters using (17-20). Mean annual runoff is simply the runoff per unit area of the drainage basin. As such, it can be multiplied by a drainage area to yield $\overline{Q}$. We chose a channel drainage area of 10,000 km^2 because our relationship between C_{v,Q_d} and R was constrained by data collected from basins larger than 5,000 km^2 and it is an appropriate intermediate basin size. In our sensitivity studies, mean annual runoff ranges between 0.001 and 1 m. This represents the range of mean annual runoff that is well represented by the data in Figure 1.

4. Methods of Sensitivity Studies

4.1. Diffusivity sensitivity studies

We explored the sensitivity of the diffusivity to a prescribed range of values of $C_{v,\tau*}$ and $\bar{\tau}_*$ for both sand- and gravel-bed channels using (22-24). The advantage of performing sensitivity studies in terms of the Shields stress distribution rather than the discharge distribution is that a single Shields stress value can represent a range of channel conditions. Shields stress values calculated from observed hydraulic parameters for gravel- and sand-bed channels range between 0.025 to 0.14 and 0.5 to 2.0, respectively, during discharges with channel-forming significance (Marr et al., 2000). In our sensitivity study we chose mean Shield stress values that are less than or equal to the observed range of Shields stress for channel-forming discharges because channel-forming discharges are relatively large events. The range of $C_{v,\tau*}$ was directly calculated using (20) assuming that C_{v,Q_d} varies between 0.5 and 8.0 for U.S. channels. A grain size is required to convert non-dimensional sediment flux to a sediment flux with units (e.g. m^2/yr). We used grain sizes of 0.02 and 0.001 m for gravel- and sand-bed channels respectively. The remaining parameter for input into (22-24) was the average channel slope, prescribed to be 0.0035 for both gravel- and sand-bed channels. We chose this value because it is a middle ranged depositional basin slope that is lower than typical alluvial fan slopes but on the high end for coarse grained river gradients. While the choice of the basin average slope does affect

the magnitude of the diffusivity, it does not significantly affect the first order behavior of the diffusivity as a function of mean Shields stress.

Thus far we have assumed that the diffusivity was only affected by changes in the magnitude and frequency of discharges. However, limiting shear stresses to near threshold conditions during large discharges (i.e., the self-forming channel of Parker (1978)) can significantly affect the relationship between diffusivity and the mean Shields stress in gravel-bed channels. In order to test the effect of limiting shear stress to account for channel bank widening on diffusivity we compare the results for calculating the diffusivity using (22) and (23). Limiting the shear stress should cause the diffusivity to decrease below the diffusivity of an equivalent channel with sufficient bank cohesion to sustain shear stresses that are well above critical.

Following the description of the results of our sensitivity studies, we compare published estimates of diffusivities for alluvial channels to those calculated with our analytic solution. Recently, Moshe et al. (2008) calculated diffusivities for several alluvial channels draining into the Dead Sea in Israel that have been adjusting to falling base level over the past 150 years. We used channel morphology and hydraulic parameters reported by Moshe et al. (2008) and Bowman et al. (2007) for input into our model (Table 1). For the parameters that were not explicitly given, we used parameter values that fell within the range of typical observed values for the region (labeled with a ^{c} in Table 1).

4.2. Long-term bedload sediment transport sensitivity studies

Sensitivity studies for the long-term bedload sediment flux as a function of mean annual runoff and the coefficient of variation of daily discharge were conducted for both gravel- and sand-bed channels. Equations (18) and (20) were used to convert the mean and variation of discharge into the mean and variation of Shields stress using the hydraulic parameters given in Table 2. We chose a middle-ranged b value of 5.0 $s^{1/2}/m^{1/2}$ to relate channel width to discharge. The final parameter required for input into (18) was channel slope. Fixing channel slope for all mean annual runoff is a simplification because the effective discharge is a function of the mean and variability of discharge. However, our goal was to compare alluvial channels of a single prescribed texture and channel slope (i.e. with values chosen to yield realistic hydrologic scenarios) across a range of mean annual runoff conditions instead of attempting to keep the Shields stress distribution the same as mean annual runoff varies.

The fixed channel slope calculated using (21) is the slope at which the channel-forming discharge (Q_{cf}) generates the prescribed Shields stress (τ_{*cf}). As such, the Shields stress distribution of our channels, which is a function of channel slope, is sensitive to these two parameters. The channel-forming discharge was calculated from the lognormal distribution using a prescribed return period (i.e., either 1.5 or 6.0 years) and a prescribed mean annual runoff. Channel-forming discharge return periods reported in the Marr et al.

(2000) study and others are predominantly for channels located in humid to temperate climates. Therefore, we chose the hydrologic distribution used to calculate the channel-forming discharge to have a prescribed mean annual runoff of 0.5 m. The coefficient of variation of daily discharge for the hydrologic distribution was then calculated using (27).

Equation (21) also requires a prescribed Shields stress (τ_{*cf}) for the channel-forming discharge. Shields stress values range between 0.025 to 0.14 and 0.5 to 2.0, for gravel- and sand-bed channels respectively, during discharges with channel-forming significance (Marr et al., 2000). We chose mid-ranged channel-forming discharge Shield stresses of 0.07 for gravel-bed channels and 1.0 for sand-bed channels. These shear stress values are appropriate for calibrating the channel slope because shear stress distributions are realistic for all considered R-C_{v,Q_d} pairs characteristic of U.S. channels (i.e., the channel-forming Shields stresses calculated for channels located in end-member climates fall within the observed range of Shields stresses). However, channel-forming Shields stresses picked near extreme ends of the observed Shields stress ranges do not yield realistic Shields stress distributions for end-member climates.

In addition to climate change, another process that affects the long-term bedload sediment fluxes is channel width adjustment to large discharges (i.e., the self-forming channel of Parker (1978)). Limiting the shear stresses produced by large discharges should reduce the long-term sediment fluxes if the contribution of large discharges to the

total sediment flux is significant. As such, we test the sensitivity of long-term sediment fluxes to regulating shear stress by comparing the results for (10) and (11).

Following the description of the sensitivity analysis, we compare our analytic solution for long-term bedload sediment fluxes to published data. Validating model predictions against observed data is essential to any quantitative analysis. Few datasets exist, however, during which continuous bedload transport rates have been sampled for all channel flow events over time scales of a few years to decades. Studies do exist where bedload transport rates were measured briefly during flows of varying magnitude over several years in order to develop power-law relationships between bedload sediment transport rates and discharge (i.e. rating curves). One of the most complete studies to date was conducted for 33 gravel-bed channels in Idaho (King et al., 2004). The parameters applied to this analysis are given in Tables 1, 7 and 8 of King et al. (2004). Discharge time series data were obtained from the National Water Information System online hydrological database (NWISWeb, http://waterdata.usgs.gov/nwis/rt) maintained by the United States Geological Survey and from the Rocky Mountain Research Station website (http://www.fs.fed.us/rm/boise/research/watershed/BAT/index.shtml) maintained by the USDA Forest Service. Observed long-term bedload sediment transport rates were calculated by numerically integrating the product of the rating curves given by King et al. (2004) and the discharge time series and then dividing by the number of days of data. King et al. (2004) published channel cross-section data that we used to compute channel width. Equations (17) and (19) were used to calculate the mean and variation of Shields

stress. We then compared the long-term bedload sediment transport rates calculated from the results of King et al. (2004) to the rates predicted by our analytic solution.

4.3. Effective discharge return period sensitivity studies

The relationship between the effective discharge and climate is not well constrained because few bedload studies exist for semiarid to arid drainages. Therefore, we also tested the sensitivity of the effective discharge return period to the mean annual runoff and the coefficient of variation of discharge. We applied the hydraulic parameters reported in Table 2 and a b value of 5.0 $s^{1/2}/m^{1/2}$ (i.e., to relate channel width to discharge) as input to these equations. As in the sensitivity study for long-term bedload sediment flux, fixed channel slopes were calculated such that the 1.5 and 6.0 year discharges yield realistic Shields stresses.

The effective discharge, and by extension the effective discharge return period, is sensitive to the relationship between discharge and sediment flux. Limiting the shear stress of larger-magnitude lower-frequency discharges should cause the effective discharge return period for gravel-bed channels to decrease. Therefore, we also tested the sensitivity of the effective discharge return period to limiting the shear stress.

Following the results of the sensitivity studies in the next section we compare effective discharge and effective discharge return periods of gravel-bed channels reported by Barry et al. (2008) and Torizzo and Pitlick (2004) to effective discharges and effective discharge return periods predicted by our effectiveness function. The parameters used for this study were found in Tables 1, 7 and 8 of King et al. (2004) and Table 1 of Torizzo and Pitlick (2004). Discharge hydrographs were obtained from the same website locations as reported in the long-term bedload sediment flux sensitivity studies.

5. Results of sensitivity studies

5.1. Diffusivity sensitivity studies

Adding a threshold term in the transport function appears to have the greatest effect on how diffusivity varies with mean Shields stress when the results for sand- and gravel-bed channels are compared (Figure 2). In the case of the sand-bed channels (dashed lines), diffusivity values increase by approximately two orders of magnitude as Shields stress values increase by one order of magnitude from 0.2 to 2. Diffusivities for gravel-bed channels (solid lines) vary over a wider range, i.e. several orders of magnitude as mean Shields stress increases by approximately the same amount from 0.01 to 1. The effect of a threshold term appears to be less significant as mean Shields stress increases above 0.06 and the relationship between diffusivity and mean Shields stress returns to a power-law behavior.

Although diffusivity values are most strongly correlated with mean Shields stress, the coefficient of variation of Shields stress also exerts a significant effect on diffusivity for both types of channels values (Figure 2). The increase in diffusivity values is more sensitive to $C_{v,\tau*}$ for gravel-bed channels when mean Shields stress is less than or equal to the critical Shields stress. A gravel-bed channel with a mean Shields stress well below the critical Shields stress but a high $C_{v,\tau*}$ value can transport significantly more sediment than one with a low $C_{v,\tau*}$. Sand-bed channels appear to consistently influenced by the coefficient of variation of Shields stress across the range of mean Shields stress. A comparison between gravel- and sand-bed channels at the high end of mean Shields stress values reveals that sand-bed channels are more sensitive to $C_{v,\tau*}$ values compared to gravel-bed channels. This occurs because the exponent of the coefficient of variation term in (24) is larger than the equivalent exponents in (22-23).

A third process that was considered for its effects on the diffusivity for gravel-bed channels was the channel width adjustment when Shields stresses exceed a critical threshold value (Figure 2). A comparison of self-forming channels (thick, solid lines) to channels able to sustain Shields stress values significantly greater than critical (thin, solid lines) reveals that diffusivity is unaffected when both mean Shields stress and the coefficient of variation of Shields stress are low (e.g. $C_{v,\tau*}$ of 0.2). At higher values of both the mean and coefficient of variation of Shields stress, self-forming channels have consistently lower diffusivities. The diffusivity of self-forming channels appears to

converge to the instantaneous transport rate for $(1+\varepsilon)\ \tau_{*cr}$ at the high end of mean Shields stress and is essentially independent of mean Shields stress. The rate that diffusivity converges appears to be dependent on the coefficient of variation of Shields stress.

The above sensitivity study results show a broad range of diffusivity values that depend primarily on mean Shields stress. The diffusivity calculated with (22) for a gravel-bed, single-thread channel that drains a 1,000 km^2 basin and that has a mean annual runoff of 100 mm is approximately $5.3x10^1$ m^2/yr when the average basin slope is on the order of 10^{-3} (Table 3). A gravel-dominated channel that drains a larger basin (10,000 km^2) located in wetter climate that has a mean annual runoff of 1.0 m yields in a diffusivity of approximately $2.67x10^6$ m^2/yr. The 5 orders of magnitude increase in diffusivity between the gravel-bed channels is mainly caused by the existence of a threshold slope condition for transport. For sand-dominated channels characterized similar drainage areas, a channel slope of 10^{-4}, channel bed sediment comprised of quartz sand with a dominant grain size of 1 mm, and mean annual runoff values that range between 0.1 and 1.0 m, the resulting diffusivities range between $2.11x10^4$ and $7.13x10^5$ m^2/yr (i.e., 0.021 and 0.71 km^2/yr).

We compared diffusivities calculated using (22) with diffusivities reported in the literature to assess the validity of our analytic solution. Calculated diffusivities for smaller-sized basins were within a factor of 4 of the diffusivity values reported by Moshe et al. (2008) (gray rows within Table 1). Diffusivities calculated for larger basins are as

much as 2 orders of magnitude greater than the reported values. For each basin considered in our study, we divided the rainfall index or annual volume of rain delivered to a basin reported by Moshe et al. 2008 by the contributing area to calculate the effective mean annual runoff. Ideally, the mean annual runoff should be directly calculated from a hydrograph record. However, few basins in this region have been monitored with stream gauges. Over-estimation of diffusivities for large basins may result from substituting rainfall as a proxy for runoff because larger basins may have a significant portion of their rainfall lost to infiltration and evaporation. In order to correct for the basin scale effect, we used a power-law relationship with exponents of −0.3 to −0.5 to calculate the mean annual runoff as a function of drainage area for semi-arid to arid basins (Farquharson et al., 1992; Baker, 2006). The power-law coefficient was determined from the effective mean annual runoff calculated for the smallest basin in the Moshe et al. (2008) data. When a power-law with an exponent of −0.3 is used to predict mean annual runoff, the calculated diffusivities show similar misfit to the diffusivities calculated using the rainfall index. However, when a power-law exponent of −0.5 is used to predict the mean annual runoff, the calculated diffusivities for larger basins show improved fit to the reported diffusivities.

5.2. Climate effects on long-term sediment transport

Figure 3 plots the results of solving (10-12) over a range of mean annual runoff values with a fixed channel slope and texture for both gravel- (Figure 3A,C) and sand- (Figure 3B,D) bed channels. The gray curves represent constant C_{v,Q_d} values of 0.5, 2 and 8, respectively. Both gravel- and sand-bed channels (solid gray lines) exhibit a positive correlation between long-term bedload sediment flux and mean annual runoff. Results for a gravel-bed channels show that the relationship between long-term bedload sediment flux and mean annual runoff is not a simple power-law relationship, which is evident from the general form of (10) (Figure 3A). Increasing C_{v,Q_d} leads to an increase in long-term sediment flux. Bedload sediment flux is effectively zero for a C_{v,Q_d} of 0.5 at low mean annual runoff values below 0.1 m. If the curves for C_{v,Q_d} of 8 and 2 are projected beyond a mean annual runoff of 1m, a point is reached where increasing C_{v,Q_d} decreases long-term bedload sediment fluxes. The location of this cross-over point is sensitive to the threshold of entrainment and the Shields stress distribution. Increasing the mean Shields stress by increasing the channel slope or decreasing the grain size would shift the cross-over point to a lower mean annual runoff. The relationship between C_{v,Q_d} and mean annual runoff is less complicated for sand-bed channels (Figure 3B). The general form of (12) is a power-law that lacks a threshold term, and therefore, the relationship between sediment flux and mean annual runoff is a straight line in log-log space. Increasing C_{v,Q_d} leads to a decrease in long-term bedload sediment flux over the entire range of mean annual runoff because all discharge magnitudes produced in the sand-bed channel are able to entrain sand. Increasing the C_{v,Q_d} increases the frequencies of the larger

discharges, but this increased contribution is not enough to offset the loss of work performed by mid-range discharges as the mode of the discharge distribution decreases.

Increasing channel width in response to discharges that exceed the threshold for entrainment (i.e. the channels are self-forming) also has an effect on the relationship between long-term bedload sediment flux and mean annual runoff in gravel-bed channels (dashed-gray lines in Figure 3A). A comparison of self-forming channels to channels that are able to sustain Shields stresses well above the threshold for entrainment shows that limiting the shear stress of larger floods decreases the long-term bedload sediment flux. The divergence in long-term bedload sediment transport rates between the two types of channels appears to be negligible at low mean annual runoff values when C_{v,Q_d} is less than 8. However, the divergence is significant as mean annual runoff increases toward 1m. If mean annual runoff continued to increase above 1m the long-term bedload sediment flux would approach the instantaneous sediment flux for the critical Shields stress. The mean annual runoff value at which the long-term rate approaches a limit is dependent on the mean Shields stress. Limiting Shields stress to near critical values during large discharges also shifts the location where increasing C_{v,Q_d} begins to decrease the long-term bedload sediment flux values toward a lower mean annual runoff value. This occurs because the contribution of larger discharges is reduced by limiting the Shields stress to near the critical Shields stress.

For channels located in the United States, C_{v,Q_d} is negatively correlated with mean annual runoff. The dot-dashed black lines in Figure 3 represent the long-term bedload sediment fluxes for U.S. channels with similar channel parameters to those chosen for our study. Long-term bedload sediment flux values increase with mean annual runoff for both channel types because increasing the mean Shields stress has a greater effect on the long-term sediment flux than decreasing the variation in Shields stress. Overall, the negative correlation between C_{v,Q_d} and mean annual runoff causes the change in long-term sediment fluxes with decreasing mean annual runoff for gravel-bed channels to be less significant than the change predicted for a channel that maintained a constant low value (i.e., ≤ 2) of C_{v,Q_d}. However, negatively correlating mean annual runoff and C_{v,Q_d} does lead to an increase in the magnitude of change in sediment flux for sand-bed channels.

We also tested the sensitivity of long-term bedload sediment flux to calibrating the channel slope based on a channel-forming discharge return period. Channel slopes were calculated such that the Shields stress of a discharge of a given return period fell within the observed range for channel-forming discharges. The higher the discharge return period, the lower the channel slope must be to yield the prescribed Shields stress. Figures 3A,B represent the results for a channel-forming discharge return period of 1.5 years, while Figures s 3C,D represent the results for the 6.0 year channel-forming discharge. Increasing the return period for the channel-forming discharge by a factor of 4 lead to less than a factor of 2 decrease in long-term sediment flux for curves that represent gravel-bed channels with high C_{v,Q_d} values. For lower C_{v,Q_d} values located toward the

humid end of the mean annual runoff axis long-term sediment flux decreased by a factor of 2 or more. Sand-bed channels showed less than a factor of 2 decrease in long-term sediment flux regardless of the C_{v,Q_d} value. Although the magnitude of long-term sediment transport rates was affected by the choice of channel-forming discharge, the first-order behavior did not change.

The curves in Figure 3 are profiles parallel to the mean annual runoff axis from the continuous parameter space that is shown in Figure 4 for gravel- (A) and sand- (B) bed channels. The advantage of the plots in Figure 4 is that effect of changes to the exponent for the power-law relationship between mean annual runoff and C_{v,Q_d} or a uniform change in C_{v,Q_d} can be more easily visualized in a 2-dimensional space. The power-law relationship between mean annual runoff and C_{v,Q_d} for U.S. channels is represented by the solid white line. A decrease in the power-law exponent or an increase in the negative correlation is equivalent to an increase in slope of the solid white lines in Figure 4. A uniform change in C_{v,Q_d} across climates of varying aridity is a vertical axis shift in the trend line. To first order, long-term bedload sediment fluxes appear to be more affected by variations in mean annual runoff than by variations in C_{v,Q_d}. Upon inspection of Figure 4, neither a rotation nor a uniform shift in the covariation between mean annual runoff and C_{v,Q_d} for the U.S. will allow channels located in arid end-member climates to transport more sediment over a period of time than equivalent channels in humid end-member climates. A climatically or anthropogenically forced increase in C_{v,Q_d} for a

gravel-bed channel could lead to an increase in long-term bedload sediment transport rates if the mean runoff value was unaffected. Increasing the C_{v,Q_d} in sand-bed channels will lead to a decrease in long-term bedload sediment fluxes

Following the sensitivity studies we also compare our analytic solution for long-term bedload sediment fluxes to values calculated from field data collected by Barry et al. (2004) from gravel-bed channels (Figure 5). Long-term sediment fluxes predicted by our analytic solution (asterisks) are on average comparable to field-measured data but also show scatter about a one-to-one line. One explanation for the scatter is that general transport equations are less accurate at predicting instantaneous sediment fluxes given mean channel conditions than site-calibrated sediment rating curves. We also plotted the long-term bedload sediment transport rates predicted by integrating the product of the Barry et al. (2004) sediment transport equation and a log normal distribution (triangles) against the observed rates. Predicted rates still show scatter, but the variation about the one-to-one line is significantly less, and thus, the accuracy of predicted long-term bedload sediment transport rates appears to be primarily affected by the choice of sediment transport equation. Another issue to consider is the spread of the observed bedload sediment transport rates. Although the observed bedload sediment transport rates cover 2-orders of magnitude, the majority of the data represent small drainages (< 5,000 km^2). Also, the data collected by Barry et al. (2004) comes from a sufficiently small study area that mean annual runoff and C_{v,Q_d} are approximately uniform over the study area. We feel that the correlation between our analytic solution predictions and observed

bedload sediment transport rates would improve with more data from other climatic regions and basin sizes that cover a wider range of long-term bedload sediment transport magnitudes.

5.3. Climate effects on effective discharge return period

A third application of our analytic solution was to calculate the return period of the effective discharge. Geomorphic effectiveness can be quantified using a variety of measures, but in alluvial channels bedload sediment flux is the most appropriate measure to adopt. The return period of the effective discharge provides an approximate time scale for geomorphic "equilibrium" because, if the return period is long (e.g. decades to centuries), the landscape can be considered to be "recovering" from the impacts of discharges of that return period in the intervals of time between events of that size. Sensitivity studies were conducted for gravel- and sand-bed channels using the same parameters listed in Table 2 in order to determine the return period of the effective discharge. The slope of the discharge effectiveness function is the product of the probability density function for discharge and transport equation as a function of discharge. The discharge beneath the peak of the discharge effectiveness function represents the effective discharge that is responsible for transporting the most sediment over a given interval of time (Wolman and Miller, 1960). In the case of gravel-bed channels, for simplicity we chose to numerically solve for the peak of the discharge

effectiveness function for each mean discharge and C_{v,Q_d} pair. For sand-bed channels, we used (26) to solve for the effective discharge.

The return period for a discharge that is greater or equal to the effective discharge is negatively correlated to the coefficient of variation of daily discharge and mean annual runoff for gravel-bed channels (Figure 6A). The effective discharge return period decreases by several orders of magnitude across the range of mean annual runoff. The decrease in the effective discharge return period over the range of C_{v,Q_d} depends on the mean annual runoff. As C_{v,Q_d} increases for channels with low mean annual runoff, the frequency of the larger discharges increases, and thus, the return period of discharges that are greater than or equal to the effective discharge decreases. At higher mean annual runoff, the lower-magnitude discharges near the mode of the distribution are able to exceed the threshold for transport. Therefore, increasing the frequency of larger discharges near the tail of the distribution does not significantly decrease the return period for the effective discharge. Conversely, at low mean annual runoff the discharges close to the mode of the distribution might not exceed the threshold for entrainment, and thus, increasing the frequency of larger storms leads to a decrease in the return period of the effective discharge.

Gravel-bed channels that are considered self-forming maintain a constant Shields stress for discharges that exceed the threshold for entrainment. Comparing Figures 6A and 6B shows that the return period for the effective discharge decreased in the region where

both mean annual runoff and the coefficient of variation of daily discharge are high when channels are self-forming. A lesser decrease also occurred in the region of high coefficient of variation and lower mean annual runoff. The region of low coefficient of variation beneath the solid white line appears to be unaffected by limiting Shields stress. Overall, decreases in the return period for the effective discharge were less than a factor of 5. The small degree of change between Figures 6A and 6B suggests that the Shields stress of the effective discharge is generally less than the $(1+\varepsilon)\tau_{*cr}$ for gravel-bed channels with lower mean annual runoff and coefficient of variation of daily discharge.

Excluding a threshold term in the sediment transport equation for sand-bed channels has a significant effect on how the effective discharge return period varies with the mean and the variation of discharge. The effective discharge return periods for sand-bed channels show a positive correlation with C_{v,Q_d} and a weaker correlation with mean annual runoff when mean annual runoff is high (Figure 6C). Increasing the frequency of larger discharges causes the effective discharge return period to increase. Nash (1994) derived solutions for the effective discharge as a function of the mean and standard deviation of discharge for lognormal and normal distributions. Our results are in agreement with those of Nash (1994) that the return period of the effective discharge has a stronger dependency on the variation than the mean of discharge when mean annual runoff is high.

At lower mean annual runoff values the effective-discharge return period for sand-bed channels switches from being primarily dependent on C_{v,Q_d} to being primarily dependent

on mean annual runoff. The lognormal distribution does not assign any probability to zero discharge, which causes the effective discharge return period to be too low for channels with low mean annual runoff. Ephemeral channels in the semi-arid to arid southwestern U.S. can spend more than half a year without flow, and thus, the effective discharge return period should be greater than that interval. Hydrographs for ephemeral U.S. channels that represent the arid end of mean annual runoff values were analyzed to determine the relationship between the maximum period of consecutive days without flow and mean annual runoff. If the computed return period was less than the observed period for the given mean annual runoff, then the computed return period was set to the observed maximum period of dry days. We found that U.S. channels with arid to semi-arid drainage basins that were greater than or equal to 10,000 km^2 still have discharge running through their channels a few days a year. As such, the return period of the effective discharge for sand-bed channels near the arid end of the mean annual runoff axis is on the order of 0.1 years.

Although a broad range of effective-discharge return periods occurs as the mean annual runoff and C_{v,Q_d} are varied, channels tend to occupy a discrete region that is represented by the solid white line in Figure s 6A, 6B and 6C. Effective discharge return periods for the sand-bed channel case are less than one year over the entire range of mean annual runoff. The threshold for entrainment of sand was set to zero by the Engelund and Hansen (1967) transport equation, and thus, the return period for the effective discharge is low compared to an equivalent gravel-bed channel. Effective discharge return periods

for the gravel channels were calculated to be between less than a year to hundreds of years, with effective discharge return periods positively correlated with aridity.

The return periods predicted for the arid end of the axis may be bias toward higher values because the channel slope was prescribed such that the 1.5-year discharge for a channel with a mean annual runoff of 0.5 m had a particular Shields stress. Channels located in basins within more arid climates do not experience flows of channel-forming significance with the same frequency as channels in temperate climates. Figure 6D shows the effect of increasing the assumed channel-forming discharge return period from 1.5 to 6.0 years for both gravel- and sand-bed channels. For gravel-bed channels, increasing the assumed channel-forming discharge return period by a factor of 4 led to a comparable increase in the effective-discharge return period. The increase in the effective-discharge return period appears to be dependent on mean annual runoff. Increasing the assumed channel-forming discharge return period did not significantly affect the effective-discharge return periods for sand-bed channels.

We also tested how accurately our solution predicted both the effective discharge and effective-discharge return period for Idaho and Colorado gravel-bed channels compared to the data reported Torizzo and Pitlick (2004) and by Barry et al. (2008). Most of the predicted effective discharge points are located within a factor of four of the one-to-one line and appear to be systematically higher than the observed effective discharges (Figure 7A). The scatter in points about the one-to-one line might result from the limited

accuracy of a general transport equation for predicting sediment fluxes based on mean channel parameters. The predicted effective-discharge return periods show a wider spread about the one-to-one line with more of the points located above the one-to-one line (Figure 7B). The systematic over-prediction of the effective discharge return period arises from overestimating the effective discharge. However, some of the predicted return periods are within a factor of 2 of the observed return periods. These results may improve if the effective discharge and effective discharge return period are calculated by binning grain size instead of using a single representative grain size. The d_{50} may be coarser than the grain size that contributes the most toward the total bedload sediment transport rate during the effective discharge, and thus, greater discharges are required to transport sediment.

6. Discussion

6.1. Diffusivity

Over the range of observed Shields stress values for sand- and gravel-bed channels, diffusivities are up to two orders of magnitude higher and lower than the range of published diffusivity values (i.e., between 10^4 to 10^5 m^2/yr) reported by other studies (Begin et al., 1981; Flemings and Jordan, 1989; Paola et al., 1992; Marr et al., 2000). Direct comparison between our results and Marr et al. (2000) and Paola et al. (1992) is difficult because their diffusivities where derived independently of specified grain size

and channel slope. Diffusivities are within the range of reported values when mean Shields stress and the coefficient of variation of daily Shields stress are between 0.02-0.03 and 0.2-0.4 for gravel-bed channels. Diffusivities for sand-bed channels are on the order of 10^5 m^2/yr when mean Shield stress is less than 0.6. While our results support the previously reported diffusivity values, diffusivity values can vary over a range greater than an order of magnitude depending on the channel slope, grain size and hydrologic distribution. Therefore, it is necessary to use these parameters to calculate the diffusivity.

Using the analytic equations for diffusivity given by (22-24), landscape evolution models can now quantify the effects of both the mean annual runoff and the coefficient of variation for discharge within transport-limited channels. Commonly, landscape evolution models and diffusion models utilize a representative flood discharge (Tucker and Slingerland; 1996; Marr et al., 2000). This representative discharge is not well defined and does not account for hydroclimatic variability. By incorporating both the mean and the variability of discharge, the full discharge distribution can be applied to calculating the long-term sediment flux without having to numerically resolve individual flood events, which can be computationally prohibitive for some models when run over geologic time scales.

6.2. Climate effects on sediment transport and the effective discharge return period

Given a channel segment that has a constant slope and grain size distribution as climatic conditions shift from wetter to dryer periods (the latter characterized by flashier discharges), the long-term bedload sediment flux decreases for both gravel- and sand-bed channels (represented by the solid white line of Figure 4). If the variation in discharge is held constant, then decreasing the mean annual runoff within a drainage basin should decrease the frequency of greater-than-threshold discharge events that contribute to the long-term sediment flux of the basin, especially for gravel-bed channels. This conclusion is consistent with those of Molnar et al. (2006). Increasing the discharge variability across the range of considered mean annual runoff values for gravel-bed channels is predicted to increase long-term bedload sediment transport rates and partially offset the effects of decreasing the mean annual runoff. Across the entire range of mean-annual runoff in sand-bed channels and at very high mean annual runoff (i.e., greater than 1m) in gravel-bed channels, long-term bedload sediment fluxes decrease with increasing discharge variability (Figure 4). For the lognormal distribution, increasing the variability while maintaining a constant mean value causes the mode to shift toward smaller discharges. Long-term bedload sediment transport rates decrease in such cases because the increase in frequency of lower rates is not offset by the increase in frequency of higher rates.

Figure 4 shows that a gravel-bed channel located at the arid end of the mean-annual-runoff axis could achieve a long-term bedload sediment flux that is on the order of an equivalent channel with a temperate mean annual runoff if the C_{v,Q_d} is sufficiently high.

However, mean annual runoff and C_{v,Q_d} have been demonstrated to covary, which places a limit on the increase in C_{v,Q_d} with increasing aridity (McMahon et al., 2007). As a result, the increase in the frequency of larger discharges is not sufficient to offset the component of sediment transported by lost by shifting the mode of the discharge distribution to lower discharges with decreasing mean annual runoff. As such, the threshold for entrainment would have to be much larger than the threshold considered in this study to allow an increase in long-term bedload sediment transport rates with increasing aridity.

Conversely, the return period for the geomorphically-effective discharge is inversely proportional to mean annual runoff. Sand-bed channels have effective flow return periods on the order of a year or less over the range of considered mean annual runoff. Gravel-bed channels in arid to hyper arid climate end-members with mean annual runoff values of less than 10 mm have effective discharge return periods on the order of hundreds of years. As the mean annual runoff of a region increases, the return period of the effective discharge decreases because the mode of the distribution moves toward larger discharges that are capable of entraining sediment. Humid climate end-members with mean annual runoff values of greater than 1000 mm have effective discharge return periods one the order of 0.1 years (i.e., scale of a few weeks to a month). These results are in agreement with the return periods calculated by Torizzo and Pitlick (2004) for gravel-bed channels with temperate mean annual runoff (i.e., 0.4-0.5 m) and D_{50} that range from 23 to 80 mm.

They found that the effective discharge was exceeded at least 1.5 to 11.3 days out of the year.

In addition to the mean and variation of the discharge distribution, channel width response to large discharges within gravel-bed channels can affect long-term bedload sediment transport rates. At high mean annual runoff values, long-term bedload sediment transport rates converge toward the instantaneous sediment transport rate calculated for a Shields stress of $(1+\varepsilon)\tau_{*cr}$. This behavior suggests that self-forming channels may have a natural upper limit to increasing long-term sediment transport rates with increasing mean annual runoff as long as the channel remains stable (i.e. does not undergo active entrenchment). However, the mean annual runoff would have to be greater than 1m for the channels considered in our sensitivity study to reach the long-term sediment flux limit.

Self-regulation of Shields stress values via channel width adjustment within gravel-bed channels appears to have less of an effect on the effective discharge return period than the long-term sediment flux. One explanation is that the effective discharge generally yields a Shields stress that is less than or equal to 1.2 to 1.4 times the critical Shields stress. As such, placing an upper limit on Shields stress did not significantly shift the effectiveness peak. However, increasing the exponent in the sediment transport equation may lead to greater effective discharges and effective discharge return periods. If the effective discharges sufficiently increased to yield Shields stresses beyond 1.4 times the critical

Shields stress, then placing an upper limit on Shields stress would have a more significant effect on the effective discharge return period.

It is important to emphasize that our results assume that the sediment flux always follows the Wiberg and Smith (1989) and Engelund and Hansen (1967) relationships. However, gravel-bed channels that develop significant channel armoring might violate this assumption. Channels with a mixture of bed grain-sizes and low or decreasing sediment supply can develop a strong vertical sorting in channel bed grain size under constant discharge conditions or during the falling limb of a storm hydrograph if the period of decreasing discharge is not brief (Hassan et al., 2006). Covering finer subsurface material with a layer of coarse material prevents sediment transport during more frequent, lower magnitude discharges, and thus, the channel is considered detachment-limited instead of transport-limited during flows that might be sufficient to entrain grain sizes less than or equal to the D_{50} grain size. A second effect of channel armoring is to increase the power-law exponent that relates sediment flux to discharge. Finer sediment in the channel bed subsurface is exhumed and mobilized in addition to the coarse surface material during large discharges capable of eroding the channel armor. Emmett and Wolman (2001) observed that channel armoring can lead to rating curve exponents up to 5, which is significantly greater than the 3/2 exponent for excess Shields stress (i.e., 9/10 exponent for discharge) assumed by our chosen sediment transport equation. Increasing the power-law exponent for the relationship between sediment flux and Shields stress

causes the long-term bedload sediment transport rates and the effective discharge return period to increase.

Our results for the long-term bedload sediment flux and effective discharge return period are also dependent on the type of distribution that is used for discharge. We applied a lognormal distribution that accurately approximates the frequency of smaller discharges that are close to mean values for channels in North America. Other distributions (e.g. power-law distribution) have been found to more accurately fit the distal tail of the discharge distribution that represents very large, infrequent discharge magnitudes (Turcotte and Greene, 1993; Molnar et al., 2006). However, the lognormal distribution is the best distribution available to accurately fit all parts of the distribution. Future research might involve a hybrid of the two distributions to obtain the best representation of the discharge distribution.

Our results for the return period of the effective discharge have implications for relating basin-averaged erosion rates of different timescales. Kirchner et al. (2001) found that basin-averaged erosion rates measured from gravel-bed channels in Idaho representative of decadal timescales based on the total sediment load are an order of magnitude lower than basin-averaged erosion rates that represent timescales of thousands to millions of years. The decrease in long-term erosion rates was interpreted as an effect of sampling over a short enough timescale such that decadal-scale erosion rates did not capture a large, infrequent storm event that accounts for 90 percent of the millennial timescale

geomorphic work. Our results for modern climate conditions suggest that the most effective geomorphic event in gravel-bed alluvial channels located in semi-arid to humid climates occurs on a time scale that is much shorter than a millennium. Sand-bed channels appear to experience effective discharges on timescales of on the order of one year. Unless alluvial channel cross-sections become perturbed by a phase of entrenchment (i.e., channel disequilibrium) or the lognormal distribution greatly underestimates the frequency of large discharges at the tail of the distribution, bedload sediment transport rates measured over a period of a few years to a decade should be representative of the bedload contribution toward the long-term basin-averaged erosion rates for drainage basins located in temperate to humid climates, provided that the vegetation of the drainage basin stays constant. Erosion rates can increase dramatically following fires and other perturbations that lead to changes in erosivity and it may be that some of the episodicity invoked by Kirchner et al. (2001) to explain their data is related to changes in vegetation and soils, including post-fire effects. However, our results suggest that hydrologic variability alone cannot result in effective discharge return periods on the order of a millennium or more.

7. Conclusions

In this study, we have derived analytic solutions for diffusivity, long-term bedload sediment flux and the effective discharge return period. Our results showed that the long-

term bedload sediment flux of alluvial channels is highly dependent on the hydroclimatic regime. As such, diffusivities should be a function of both the mean and variation of the discharge distribution. We also showed that the mean and variation of discharge are negatively correlated for U.S. channels. Channels in humid climates are characterized by a discharge distribution with larger mean discharge but a lower coefficient of variation. Conversely, channels in arid environments are characterized by lower mean annual discharge but higher coefficients of variation. If the threshold for bed material entrainment is relatively low then the sediment flux contribution of more frequent, smaller discharges allows channels in humid climates to transport a greater quantity of sediment in a given time period than similar channels located in arid climates. Conversely, the return period for the effective discharge is negatively correlated with mean annual runoff. The threshold for sediment entrainment and cross-sectional geometry greatly affect the long-term sediment flux and effective discharge, and therefore, gravel- and sand-bed channels are predicted to evolve over different time scales in response to climate change.

Notation

b	power-law coefficient for the relationship between w and Q, $s^{1/2}/m^{1/2}$ if Q has units of m^3/s and the exponent is 1/2
C_f	dimensionless drag coefficient
$C_{v,Q}$	coefficient of variation of discharge
C_{v,Q_d}	coefficient of variation of daily discharge
$C_{v,\tau*}$	coefficient of variation of Shields stress
d	grain size of bedload sediment, m
ε	constant for scaling Shields stress with respect to Critical Shields stress
g	gravitational acceleration, m/s^2
h	elevation, m
κ	diffusivity, m^2/yr
μ_{lnQ}	mean of the natural log of discharge per unit channel width, m^2/s
$\mu_{ln\tau*}$	mean of the natural log of Shields stress
n	Manning's roughness coefficient
η	sediment transport equation exponent
q_{s*}	non-dimensional sediment flux
$\bar{q}_{s*}$	long-term non-dimensional sediment flux
Q	volumetric discharge, m^3/s
$\bar{Q}$	mean annual discharge, m^3/s
Q_{cf}	channel-forming discharge, m^3/s

Q_e effective discharge, m^3/s

R mean annual runoff, m

ρ_s density of bedload sediment, kg/m^3

ρ_f density of fluid, kg/m^3

S local channel slope

S_0 average channel slope for a given reach of simulated channel profile

σ_{lnQ} standard deviation of the natural log of discharge per unit channel width, m^3/s

$\sigma_{ln\tau_*}$ standard deviation of the natural log of Shields stress

t time, s

T_{Q_e} effective discharge return period, yr

τ_* Shields stress

τ_{*cf} channel-forming discharge Shields stress

$\bar{\tau}_*$ mean Shields stress

τ_{*cr} critical Shields stress of bedload sediment

x distance from the model origin, m

w channel width, m

References

Ackers, P., White, W.R., 1973. Sediment transport: New approach and analysis. J. Hydraul. Div. Am. Soc. Civ. Eng., 99, 2041-2060.

Alexander, R.B., Slack, J.R., Ludtke, A.S., Fitzgerald, K.K., Schertz, T.L., 1996. Data from selected U.S. Geological Survey national stream water-quality monitoring networks *(WQN)*: U.S. Geological Survey Digital Data Series, DDS-37, 2 disc.

Baker, V.R., 2006. Paleoflood hydrology in a global context. Catena, 66, 161-168.

Bagnold, R.A., 1980. An empirical correlation of bed-load transport in flumes and natural rivers. Proc. R. Soc. London, A372, 453-473.

Barry, J.J., Buffington, J.M., King, J.G., 2004. A general power equation for predicting bed load transport rates in gravel bed rivers. Water Resour. Res., 40, doi:10.1029/2004WR003190.

Barry, J.J., Buffington, J.M., Goodwin, P., King, J.G., Emmett, W.W., 2008. Performance of Bed-Load Transport Equation Relative to Geomorphic Significance: Predicting Effective Discharge and Its Transport Rate. J. Hydraul. Engineering, doi:10.1061/(ASCE)0733-9429(2008)134:5(601).

Blench, T., 1952. Regime theory for self-forming sediment-bearing channels. Trans. ASCE, 117, 383-408.

Bowman, D., Shachnovich-Firtel, Y., Devora, S., 2007. Stream channel convexity induced by continuous base level lowering, the Dead Sea, Israel. Geomorph., 92, 60-75.

Church, M., Rood, K., 1983. Catalogue of Alluvial River Channel Regime Data: University of British Columbia, Department of Geography, Vancouver, BC.

Coulthard, T.J., Macklin, M.G., Kirkby, M.J., 2002. A cellular model of Holocene upland river basin and alluvial fan evolution. Earth Surf. Processes Landforms, 27, 269-288.

Doyle, M.W., Shields, D., Boyd, K.F., Skidmore, P.B., DeWitt, D., 2007. Channel-forming discharge selection in river restoration design. J. Hydraul. Engineering, 133, 831-837.

Einstein, H.A., 1950. The bed load function for sediment transport in open channel flows. Tech. Bull. 1026, Soil Conserv. Serv., U.S. Department of Army, Washington, D.C.

Emmett, W.W., Wolman M.G., 2001. Effective discharge and gravel-bed rivers. Earth Surf. Processes Landforms, 26, 1369-1380.

Engelund, F., Hansen H., 1967. Investigation of flow in alluvial streams. Acta Polytechnica Scandanavia, ci-35.

Farquharson, F.A.K., Meigh, J.R., Sutcliffe, J.V., 1992. Regional flood frequency analysis in arid and semi-arid areas. J. Hydro., 138, 487-501.

Flemings, P., Jordan T., 1989. A synthetic stratigraphic model of foreland basin development. J. Geophys. Res., 94, 3851-3866.

Gomez, B., Church, M., 1989. An assessment of bed load sediment transport formulae for gravel bed rivers. Water Resour. Res., 25, 1161-1186.

Goodwin, P., 2004. Analytical solutions for estimating effective discharge. J. Hydraul. Engineering, 130, 729-738.

Harlin, J.M., 1978. Reservoir Sedimentation as a Function of Precipitation Variability. Water Resour. Bull., 14, 1457-1465.

Hassan, M.A., Egozi, R., Parker, G., 2006. Experiments on the effect of hydrograph characteristics on vertical grain sorting in gravel bed rivers. Water Resour. Res., 42, doi:10.1029/2005WR004707.

Inman, D.L., Jenkins S.A., 1999. Climate change and the Episodicity of sediment flux of small California rivers. J. Geol., 107, 251-270.

Kettner, A.J., Syvitski, J.P.M., 2008. HyrdoTrend v.3.0: A climate-driven hydrological transport model that simulates discharge and sediment load leaving a river system. Comp. and Geosci., 43, 1170-1183.

King, J.G., Emmett, W.W., Whiting, P.J., Kenworthy, R.P., Barry, J.J., 2004. Sediment transport data and related information for selected coarse-bed streams and rivers in Idaho. U.S. For. Serve. Gen. Tech. Rep. RM, RMRS-GTR-131, 26 pp.

Kirchner, J.W., Finkel, R.C., Riebe, C.S., Granger, D.E., Clayton, J.L., King, J.G., Megahan, W.F., 2001. Mountain erosion over 10 yr. 10 k.y., and 10 M.y. time scales. Geology, 29, 591-594.

Knighton, David, 1998. Fluvial Forms and Processes: A New Perspective. Arnold, London.

Leier, A.L., P.G. DeCelles, Pelletier, J.D., 2005. Mountains, monsoons, and megafans. Geology, 33, 289-292.

Leopold, L.B., Maddock, T., 1953. The hydraulic geometry of stream channels and some physiograhic implications. Professional Paper no. 252, US Geologic Survey, Washington, DC.

Leopold, L.B., Wolman, M.G., Miller J.P., 1964. Fluvial processes in Geomorphology. 522 pp., W.H. Freeman, London.

Magilligan, F.J., Nislow, K.H., 2005. Changes in hydrologic regimes by dams. Geomorph., 71, 61-78.

Marr, J.G., Swenson, J.B., Paola, C., Voller, V.R., 2000. A two-diffusion model of fluvial stratigraphy in closed depositional basins. Basin Research, 12, 381-398.

McMahon, T.A., Vogel, R.M., Peel, M.C., Pegram, G., 2007. Global Stream Flows – Part 1: Characteristics of annual stream flows. J. Hydro., 347, 243-259.

Meyer-Peter, E., Muller R., 1948. Formulas for bed-load transport. in *Proceedings 2nd Congress International Association of Hydrological Research*, pp. 39-64, Int. Assoc. of Hydraul. Res., Stockholm.

Molnar, P., 2001. Climate change, flooding in arid environments, and erosion rates. Geology, 29, 1071-1074.

Molnar, P., 2004. Late Cenozoic increase in accumulation rates of terrestrial sediment: How might climate change have affected erosion rates? Annu. Rev. Earth Planet. Sci., 32, 67-89.

Molnar, P., Anderson, R., Kier, G., Rose, J., 2006. Relationships among probability distributions of stream discharges in floods, climate, bed load transport, and river incision. J. Geophys. Res., 111, F02001, doi:10.1029/2005JF000310.

Moshe, L.B., Haviv, I., Enzel, Y., Zilberman, E., Matmon, A., 2008. Incision of alluvial channels in response to continuous base level fall: Field characterization, modeling and validation along the Dead Sea. Geomorph., 93, 524-536.

Nash, D.B., 1994. Effective sediment-transporting discharge from magnitude-frequency analysis. J. Geol., 102, 79-95.

Parker, G., 1978. Self-forming straight rivers with equilibrium banks and mobile bed, part 2, The gravel river. J. Fluid Mech., 89, 127-146.

Parker, G., Klingeman, P.C., McLean, D.G., 1982. Bedload and size distribution in paved gravel-bed streams. J. Hydraul. Div. Am. Soc. Civ. Eng., 108, 544-571.

Ritchie, B.D., Hardy, S., Gawthorpe, R.L., 1999. Three-dimensional numerical model of coarse grained clastic deposition in sedimentary basins. J. Geophys. Res., 104, 17759-17780.

Simons, D.B., Albertson, M.L., 1963. Uniform water conveyance channel in alluvial material. Trans. ASCE, 128(1), 65-107.

Torizzo, M., Pitlick, J., 2004. Magnitude-frequency of bed load transport in mountain streams in Colorado. J. Hydrol., 290, 137-151.

Tucker, G.E., Slingerland, R., 1996. Predicting sediment flux from fold and thrust belts. Basin Research, 8, 329-349.

Turcotte, D.L., Greene, L., 1993. A scale-invariant approach to flood frequency analysis. Stocastic Hydrol. Hydraul., 7, 33-40.

Wiberg, P.L., Smith, J.D., 1989. Model for calculating bed-load transport of sediment. J. Hydraul. Eng., 115, 101-123.

Wolman, M.G., Miller, J.P., 1960. Magnitude and Frequency of Forces in Geomorphic Processes. J. Geol., 68, 54-74.

Tables:

Table 1: Calculated and reported Diffusivities for channels draining in the Dead Sea

Number	Channel	Drainage Area (km^2)	Mean Q (m^3/s)	$C_{v,Q}$	Slope	Grain Size (m)	Channel Width (m)	Calculated Diffusivity (m^2/day)	Reported Diffusivity (m^2/day)
1	Qumeran	47	0.238	1.42	0.35	0.008	50	4.55[a], 24.78[b]	8
2	Qidron	123	1.046	1.24	0.04[c]	0.016	60[c]	35.11[a], 3.18[b]	11.25
3	Darga	237	2.347	1.19	0.05	0.016	80	332.68[a], 12.22[b]	22.5
4	Qedem	12	0.044	1.55	0.1	0.004	60[c]	4.42[a], 112.99[b]	1.25
5	Ishai	2	0.076	0.83	0.04[c]	0.005	60[c]	0.02[a], 0.02[b]	0.041
6	Hever	175	1.494	1.24	0.04[c]	0.008	60[c]	617.2[a], 140.48[b]	6.75
7	Zeelim	253	1.506	1.36	0.02	0.008	60[c]	245.82[a], 49.58[b]	1.5

[a] Diffusivities calculated using rainfall index to predict mean annual runoff
[b] Diffusivities calculated using a power-law relationship between mean annual runoff and drainage area with an exponent of −0.5
[c] Data was not explicitly provided by either Moshe et al. (2008) or Bowman et al. (2007)

Table 2: Parameters used in calculations for Figures 3, 4 and 6

Parameters	Gravel-bed	Sand-bed
Drainage Area (km^2)	$1.0x10^4$	$1.0x10^4$
Manning's Roughness Coefficient, n	0.035	0.035
Grain Size, d (m)	0.02	0.001
Submerged Specific Gravity	1.7	1.7
Critical Shields Stress, τ_{*cr}	0.047	NA
Channel-Forming Discharge Shields Stress, τ_*	0.07	1.0
Channel-Forming Discharge Return Period (yr)	1.5, 6.0	1.5, 6.0

Table 3: Calculated diffusivities and corresponding parameters

Drainage Area (km^2)	R (m/yr)	Mean Q (m^3/s)	$C_{v,Q}$	d (m)	S_0	Diffusivities (m^2/yr)
$1.0x10^3$	1	31.71	0.868	0.01	$1.0x10^{-3}$	$1.09x10^4$
$1.0x10^3$	0.1	3.17	1.616	0.01	$1.0x10^{-4}$	$5.34x10^1$
$1.0x10^4$	1	317.10	0.868	0.01	$1.0x10^{-3}$	$2.67x10^6$
$1.0x10^4$	0.1	31.71	1.616	0.01	$1.0x10^{-4}$	$5.59x10^4$
$1.0x10^3$	1	31.71	0.868	0.001	$1.0x10^{-3}$	$1.27x10^5$

$1.0x10^{3}$	0.1	3.17	1.616	0.001	$1.0x10^{-4}$	$2.11x10^{4}$
$1.0x10^{4}$	1	317.10	0.868	0.001	$1.0x10^{-3}$	$7.13x10^{5}$
$1.0x10^{4}$	0.1	31.71	1.616	0.001	$1.0x10^{-4}$	$1.19x10^{5}$

Figures:

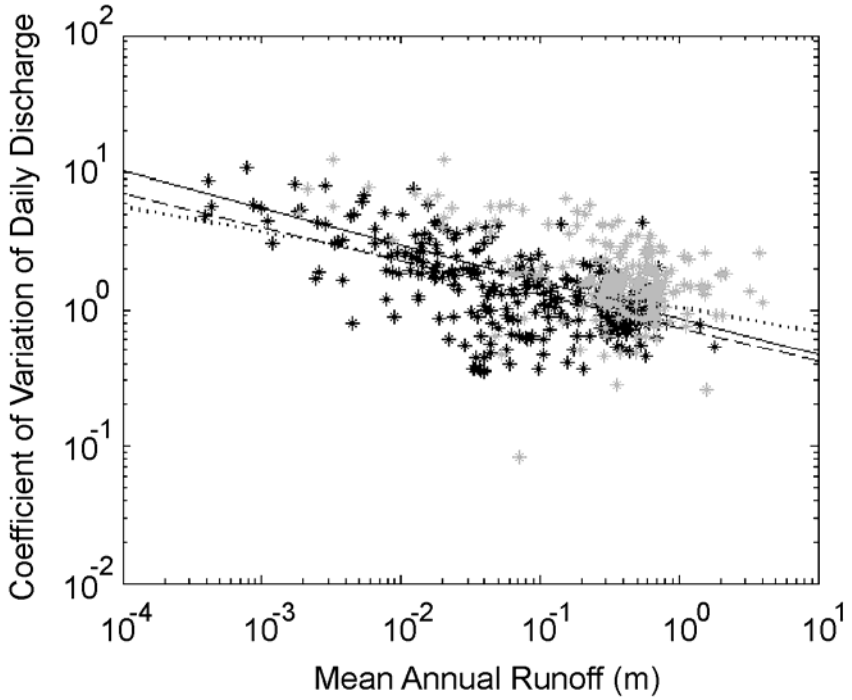

Figure 1: Relationship between mean annual runoff and the coefficient of variation of daily discharge for 530 United States channels. Channels that drain areas between 10 and 5,000 km^2 (gray) and 5,000 to $3.0x10^6$ km^2 (black) are plotted as asterisks. Linear regression lines for this study are the following: (solid line) trend line for data binned by mean annual runoff, (dashed line) trend line for all data points that represent drainage basins larger than 5,000 km^2 and (dotted line) trend line for all data points.

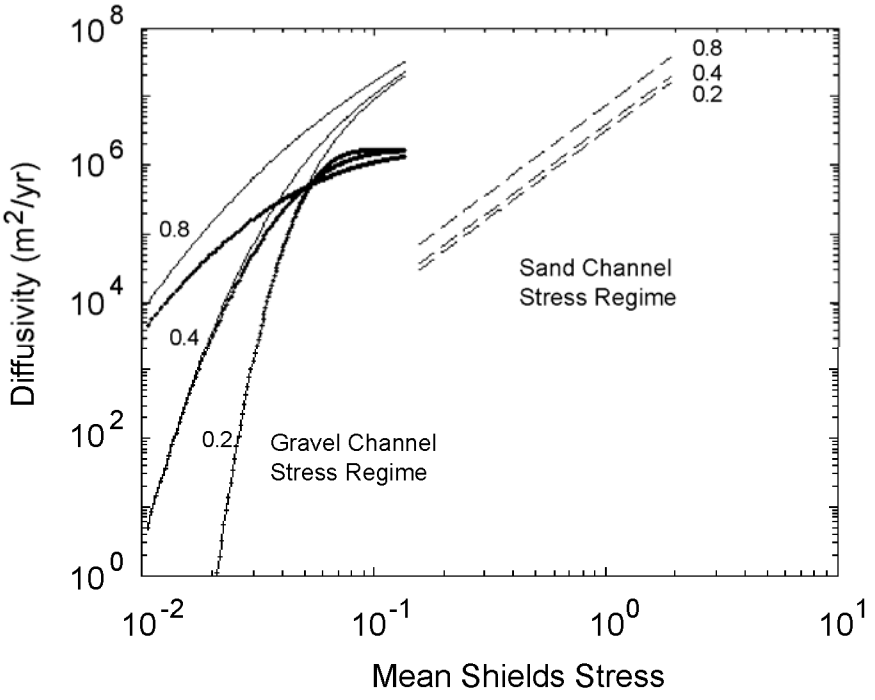

Figure 2: A comparison of diffusivity values for sand- (dashed lines) and gravel- (solid thin lines represent cohesive channels and dotted-solid lines represent self-regulating channels) bed channels as a function of mean Shields stress. Diffusivity values were calculated for three coefficient of variation of Shields stress values that span the expected range for U.S. channels (i.e., 0.2, 0.4 and 0.8).

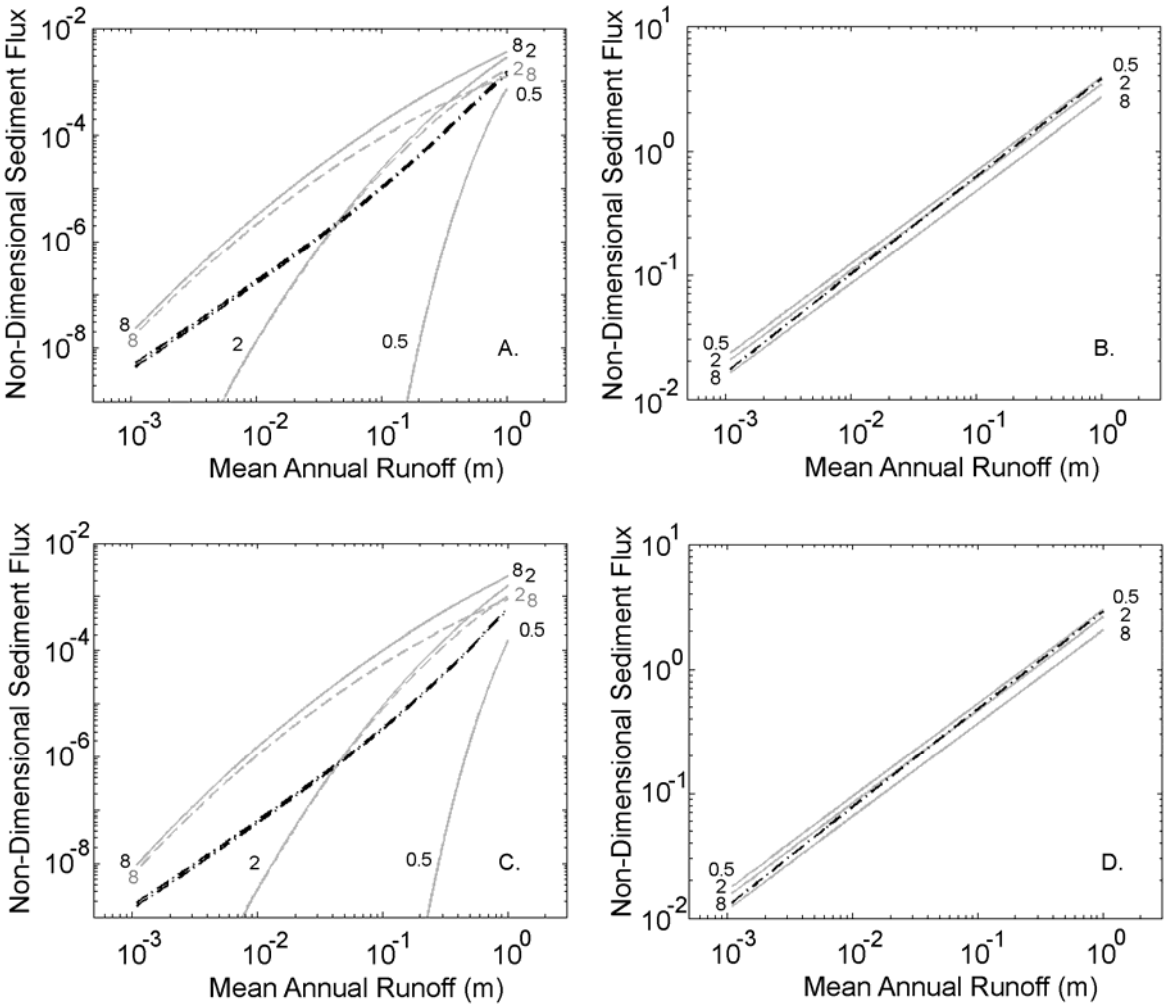

Figure 3: Relationship between climate and long-term bedload sediment flux for gravel- (A, C) and sand-bed channels (B, D). Each gray curve represents a different coefficient of variation of daily discharge (i.e., 0.5, 2 and 8). For the gravel-dominated channels the solid lines and black numbers represent cohesive channels. The dashed lines and gray numbers represent self-forming channels. The dash-dotted lines in each figure represent a channel in which the coefficient of variation of daily discharge is a function of mean annual runoff. Figures (A, B) represent channels with slopes calibrated to the 1.5 year

discharge and Figures (C, D) represent channels with slopes calibrated to the 6.0 year discharge.

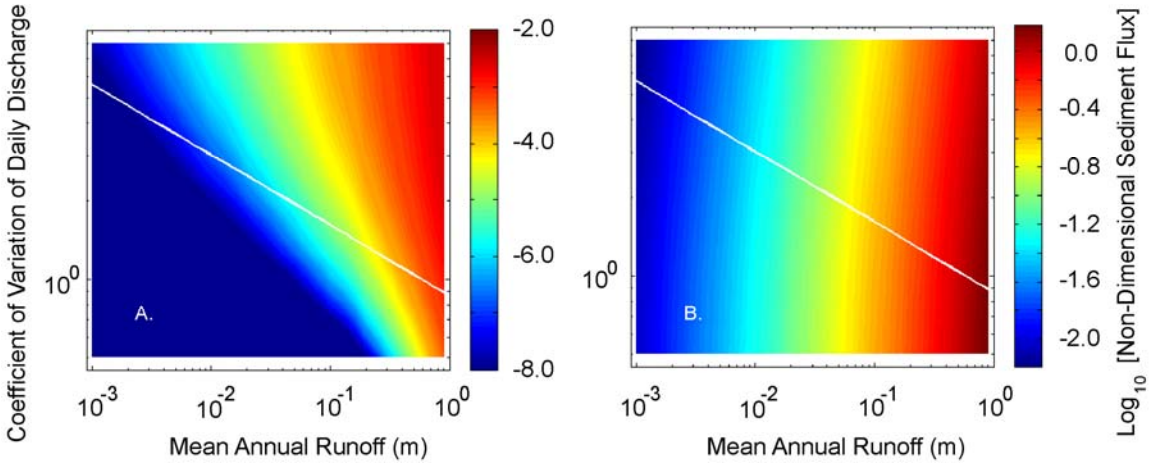

Figure 4: The relationship between long-term sediment flux and climate (expressed in terms of mean and coefficient of variation of discharge) for gravel- (A) and sand- (B) bed channels of constant grain size and slope. The thick, white line represents the covariation between mean annual runoff and the coefficient of variation of daily discharge observed for modern U.S. channels.

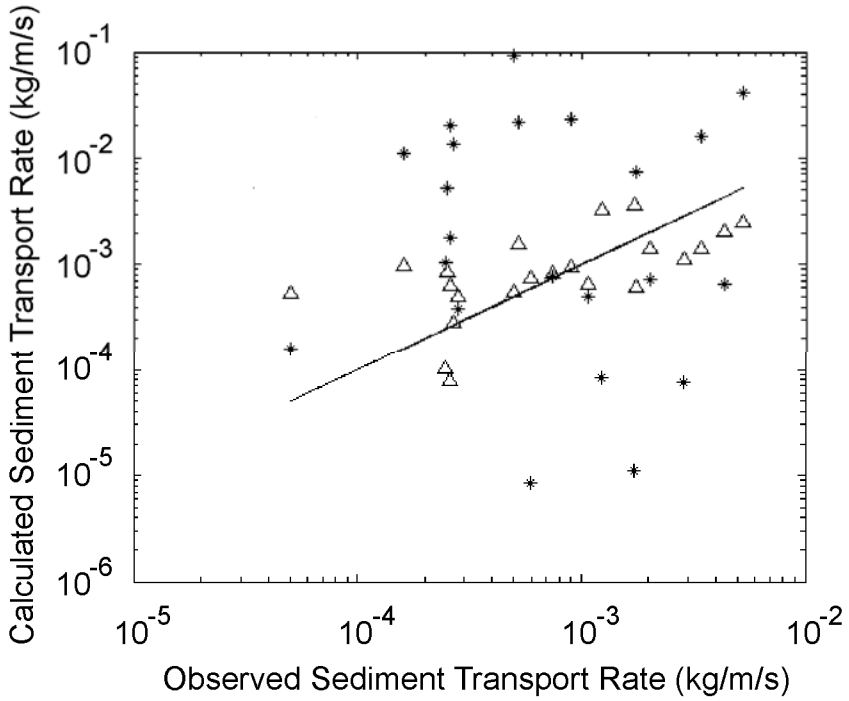

Figure 5: A comparison of long-term bedload sediment transport rates for gravel-bed channels that were calculated using a site-calibrated rating curve (solid line), the Barry et al. (2004) transport formula (triangles), and the Wiberg and Smith (1989) transport formula (asterisks).

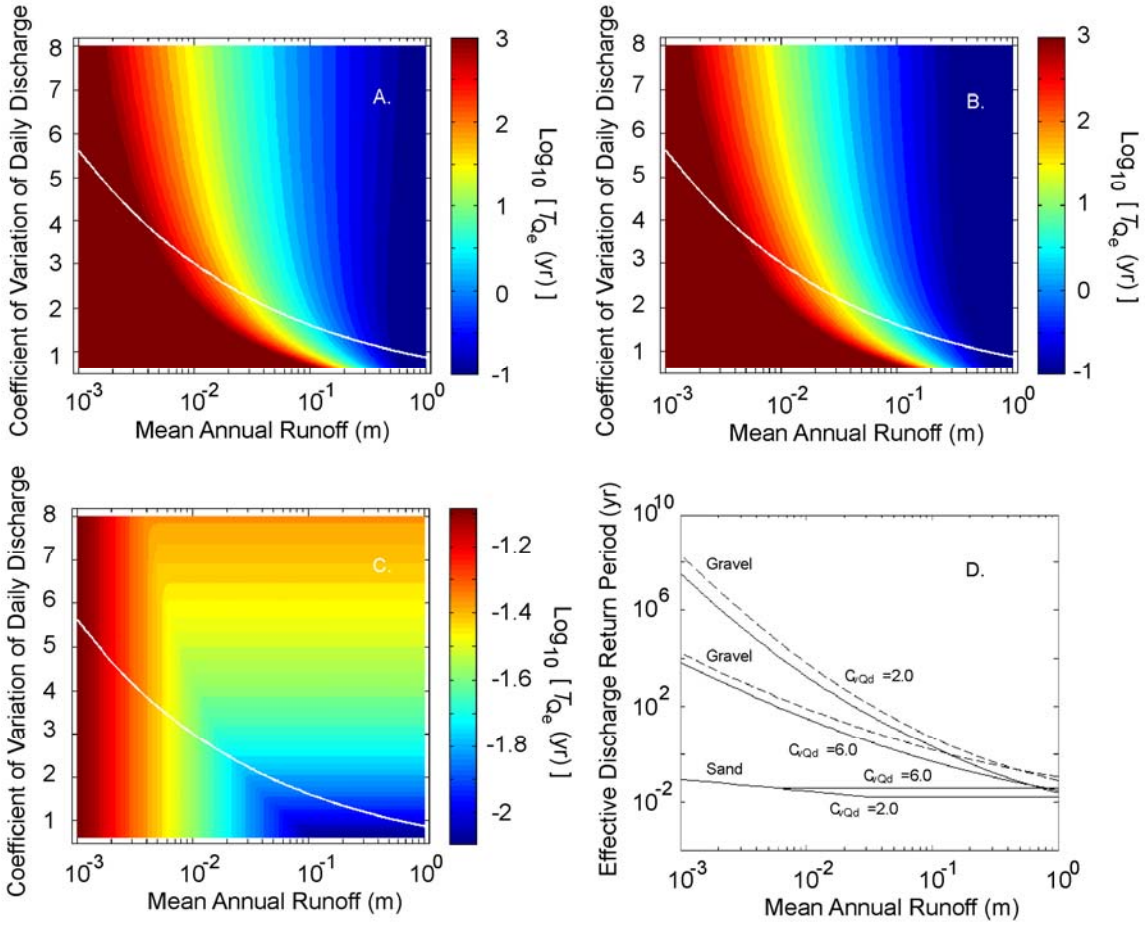

Figure 6: The relationship between the effective discharge return period and parameters of the hydroclimatology for gravel- (A, B, D) and sand- (B, D) bed channels. Figure 6A represents a channel with cohesive banks and 6B represents a self-forming channel. The thin, white line in (A, B, C) represents the covariation between mean annual runoff and the coefficient of variation of daily discharge that is observed in modern channels. In Figure 6D the dashed lines represent channels with slopes calibrated to the 6.0 year discharge and the solid lines represent calibrating slope to the 1.5 year discharge.

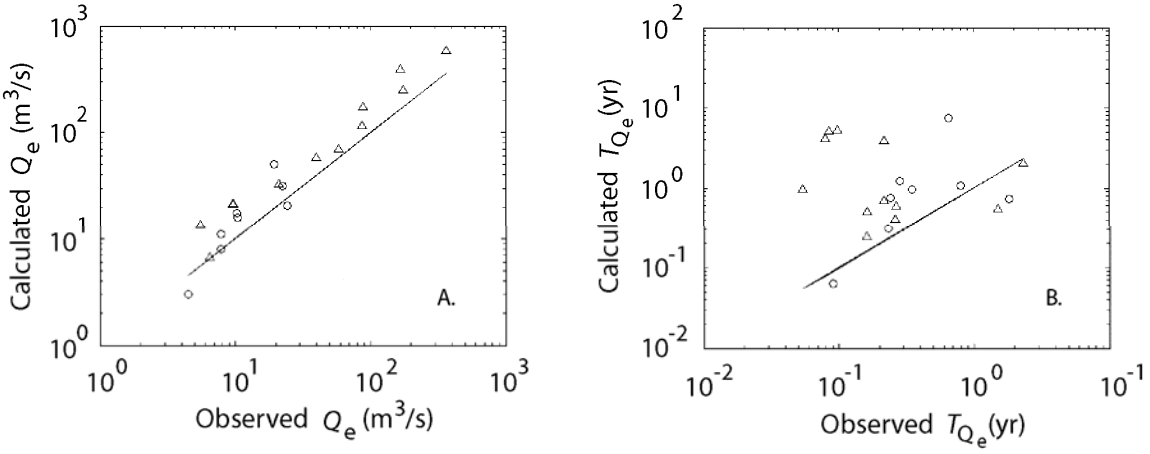

Figure 7: A comparison of the effective discharge (A) and effective discharge return period (B) predicted by our analytic solution to field observations for gravel-bed channels from Barry et al. (2008) (triangles) and Torizzo and Pitlick (2004) (circles).